Simulation of drying for multilayer investment casting shells.

Harun, Zawati

CIVIL AND COMPUTATIONAL ENGINEERING CENTRE
SWANSEA UNIVERSITY

SIMULATION OF DRYING FOR MULTILAYER INVESTMENT CASTING SHELLS

ZAWATI HARUN

B.Sc., M.Sc. (Malaysia)

THESIS SUBMITTED TO THE SWANSEA UNIVERSITY IN FULFILLMENT OF THE REQUIREMENTS FOR THE DEGREE OF DOCTOR OF PHILOSOPHY

NOVEMBER 2007

ProQuest LLC.
789 East Eisenhower Parkway
P.O. Box 1346
Ann Arbor, MI 48106 – 1346

ABSTRACT

The number of interacting variables influencing the drying of ceramic shells is large and to explore by experimental means is prohibitive. Therefore, the main advantage of the proposed theoretical model in this work, is that the effect of the drying conditions on their other important parameters (such as saturation, temperature, gas pressure) and transport properties (permeabilities, diffusivity) that control final properties of a multilayer ceramic shell can be investigated without extensive experimentation. This is very important in avoiding shell failure due to incomplete drying.

Due to the fact that a porous ceramic body is a three phase system (solid, liquid and gas), modelling its transport and thermodynamic behaviour involves a complex solution due to the highly nonlinear physics that capture their evolution. A two-dimensional numerical model based on the fundamental equations of heat, mass and gas transport was developed to establish the drying and thermodynamic response of the ceramic shell system. This complete coupled set is based on Whitaker's model that includes the mass, momentum and energy equation which also embodies the constitutive diffusion and capillary flow theory and its evaporation-condensation term in the flow phases; conduction, convection and latent heat of evaporation in the energy equation; along with the gas transport equation.

The most widely implemented numerical solution (the fully implicit backward time stepping scheme) in the area of multiphase flow and drying in porous media was chosen for the temporal solution. The finite element method was employed for the spatial solution, due to its flexibility in dealing with complex geometries, and also it shows an ideal approach to employ in the solution of this class of problem. Both of the temporal and spatial numerical solutions for the theoretical solution were implemented into a computational code by using the Fortran programming language.

This simulation scheme has been benchmarked against thermal test cases (to confirm the correct functioning of the thermal analysis) and for the first time the brick drying benchmark by Stanish in which it is demonstrated to provide the best solution. The

scheme was then extended to address the drying of a single ceramic layer and compared with the published work, again showing good agreement.

For the first time a simulation approach for the drying of a multilayer system that includes the impact of wet layer addition is proposed. The principles of an ab initio scheme are demonstrated that again show good agreement with experimental trends.

Further work is required to obtain a better match with experimental data, but to do so will require improvements in deriving a compatible material data set that is appropriate for this simulation approach. The scheme set out in this thesis may be used to guide the test selection to facilitate derivation of these material properties.

DECLARATION

This work has not previously been accepted in substance for any degree and is not being concurrently submitted in candidature for any degree.

Signed ..... (candidate)

Date 29-1-2008

STATEMENT 1

This thesis is the result of my own investigations, except where otherwise stated. Where correction services have been used, the extend and nature of the correction is clearly marked in a footnote(s). Other sources are acknowledged by footnotes giving explicit references. A bibliography is appended.

Signed ... . (candidate)

Date 29-1-2008

STATEMENT 2

I hereby give consent for my thesis, if accepted, to be available for photocopying and for inter-library loans, and for the title and summary to be made available to outside organisations.

Signed ..... (candidate)

Date 29-1-2008

CONTENTS

CHAPTER 3 : MATERIAL PROPERTIES AND TRANSPORT PROPERTIES

CHAPTER 4 : MATHEMATICAL FORMULATIONS AND THEORETICAL MODELLING

LIST OF FIGURES

LIST OF TABLES

ACKNOWLEDGEMENTS

Pursuing the degree of PhD is both a painful and an enjoyable experience. It's just like climbing a high peak, step by step, accompanied with bitterness, hardships, frustration, encouragement and trust. In all these years, many people were instrumental directly or indirectly in shaping up my academic career. Though it will not be enough to express in words to all those people who helped me, I would still like to give my many, many thanks to all these people.

First of all, I would like to give my sincere thanks to my supervisor, Prof. David Gethin, who accepted me as his PhD. student without any hesitation when I presented him my research proposal. Thereafter, he offered me so much advice, patiently supervising me, and always guiding me in the right direction. I have learned a lot from him, without his help I could not have finished my dissertation successfully. His company and assurance at the time of crisis will be remembered lifelong.

I would also like to gratefully acknowledge the support of some very special individuals. They helped me immensely by giving encouragement and friendship, this includes Prof. Roland Lewis and Dr. William J. Ferguson. I can only say thank you very much.

I would like to express my appreciation to Rolls Royce plc and Dr. Paul Withey who offered me their time when I collected necessary data for my case study in their company.

Special acknowledgment is also given to Malaysian Public Service Department and Universiti Tun Hussein Onn Malaysia (UTHM) for funding this research.

I thank my parents in law for their continuous prayer, patience, support and love whenever I need it over these years. I also would like to dedicate this work to my two young children, Nur Qurrata Aina and Muhammad Hafizuddin for their silent prayer for my work at the time when they needed my company most. Their love and support

without any complaint or regret has enabled me to complete this PhD. They are always the source of motivation behind me.

Finally, I would like to express my deepest appreciation to my beloved husband, Nazri Mohd Nawi, for his presence in my life. We have been each others best friends and the strongest supporters all these times. Without his loving support and understanding I would never have completed my present work. His patience and encouragement was the drive for me.

ABBREVIATIONS AND NOMENCLATURE

NOTATIONS

exp.	Experiment
MOR	Modulus Of Rupture.
sim	Simulation
C_p	Specific heat (J/kg K).
D_{atm}	Molecular diffusivity of water vapor (m^2/s)
g	Acceleration due to gravity (m/s^2).
h_T	Heat transfer coefficient (W/m^2 K).
L	Latent heat of vaporization (J/kg)
h_m	Mass transfer coefficient at the outer surface of insulation (kg/m^2 s).
K_{intc}	Absolute permeability (m^2).
λ	Thermal conductivity (W/m K).
k	Relative permeability
$\dot{m}$	Rate of phase change (negative for condensation) (kg/m^3 s).
P	Pressure (Pa).
R	Universal gas constant (=8314 J/kmol K).
S	Dimensionless liquid saturation.
v	Velocity (ms^{-1})
T	Temperature (deg C).
t	Time (s).
M	Molar Mass (kg/mol^{-1})

GREEK SYMBOLS

ϕ	Porosity.
μ	Dynamic viscosity (kg/m s).
ρ	Density (kg/m^3).

SUBSCRIPTS

g	Gas
l	Liquid
s	Solid
v	Vapor
a	Air
sat	Saturated condition
o	Initial condition
cri	Critical
c	Capillary
irr	Irreducible condition

CHAPTER 1

INTRODUCTION

1.0 Background

The investment casting process will be summarised in a later section in this chapter. However, for many years, precision investment casting foundries have periodically reported serious casting defects (Hyde, October 1995). One source is associated with the shell manufacturing process and is due to unremoved moisture during the drying of the layers as they form the shell. This results in a cracking mechanism in the dewax cycle as it may create vapour pressure build up in the shell body (Jones and Leyland, 1994). This defect is attributed to uncontrolled drying. The drying condition is very critical to shell manufacture due to the fact that it can lead to hygrothermal stresses and hence the shell can exhibit a tendency to crack. Therefore, the production environment for the ceramic shell must be enclosed and incorporate temperature and humidity control systems. One of the longest steps in shell manufacture is the drying process which must be carried out in a controlled environment after each dipping and stuccoing stage in the build up process. Each layer can take typically up to two hours to complete the dipping and drying process. Therefore failure of an investment mould can be extremely expensive not only because of the loss of raw materials, but in terms of processing time and the cost of the drying process which is energy intensive.

One of the main reasons for failure is not having detailed knowledge of the drying process, such as controlling the drying parameters which are highly influenced by the transport mechanism especially in the case of a porous medium. Other factors that may contribute to failure are raw materials, such as binders, solution etc. but these are not taken into consideration in this work as they may be controlled through well established quality control procedures that may be established through laboratory based procedures (Roberts and Delaware, 1995).

Experimentation has contributed to significant process understanding and hence improvement. Investigation has explored the changing of the drying parameters (Leyland and Jones, 1994), the drying time (Guerra *et al.*, 1992), the raw materials (Jones, February-June 1994) etc. and their final impact on the final shell performance. This empirical approach is expensive, time consuming, and valid only for the conditions explored within the confines of the experiment. Recently, with the advent of powerful computers, more emphasis has been given to process modelling. The use of computer models has provided better understanding of several industrial processes, and the simulation of situations never considered before have resulted in innovative process improvements.

Before proceeding to the modelling approach it is appropriate to have some overview of the main stages in the ceramic shell making process and also its common failures. This may help to identify or give a clear description of the drying parameters and how they may contribute to process failure.

1.1 General process of the ceramic shell build up process

The complete investment casting process is shown in Figure 1.1. The current project focuses specifically on stages 4 and 5.

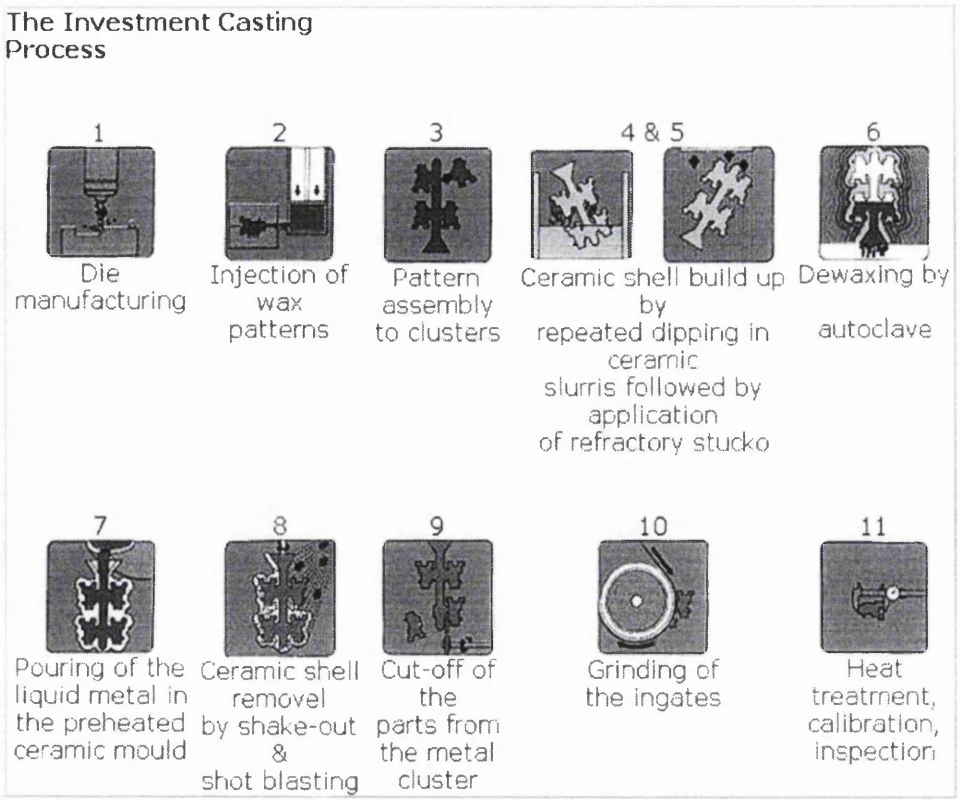

Figure 1.1: The investment casting process (P.I.Casting Ltd).

The term investment casting derives from the characteristic use of mobile ceramic slurry, or investment, to form a mould that has an extremely smooth surface. Investment casting allows dimensionally accurate components to be produced and is a cheaper alternative than forging or machining, since the waste material is kept to a minimum (Jones and Marquis, 1995). Quantitative understanding of the shell formation process can help to establish the structure and property relationship for the mould. Recently, many researchers have realized the importance of the drying process and conditions to control the quality of the final ceramic shell, however none have attempted to analyse this part of shell formation rigorously through development of process simulation techniques.

The basic step in the production of a ceramic shell is the dipping of the assembled wax pattern into a muticomponent slurry which is composed of a fine mesh refractory ceramic and colloidal binder system. After this, a layer of fine ceramic powder is added to retain the fidelity of the wax surface. Further layers are then added to build

up the shell thickness and hence strength. Thus, after every dipping process a ceramic layer is added by sprinkling refractory stucco that is then dried. The purpose of stucco addition in this way is to minimise the drying stresses and to facilitate a mechanical bond between the primary coating and the back up or secondary layer. Thus, an investment casting mould consists of individual layers of fine and granular refractory material held together into the required thickness. This can be seen in stages 4 and 5 in Figure 1.1.

The rate of drying between consecutive layer applications plays an important role in economic production of shell moulds in order to get the optimum strength. Normally, each layer of the mould takes between 1 and 2 hours to produce due to the need for controlled moisture removal in every layer. Unless sufficient moisture is removed the layer will have insufficient mechanical strength to allow another to be applied (Jones and Leyland, 1994; Leyland and Jones, 1994). Drying and strength development are the most significant rate-limiting factors in reduction of lead times and production costs for the ceramic shell making process within the casting industry (Leyland and Jones, 1994).

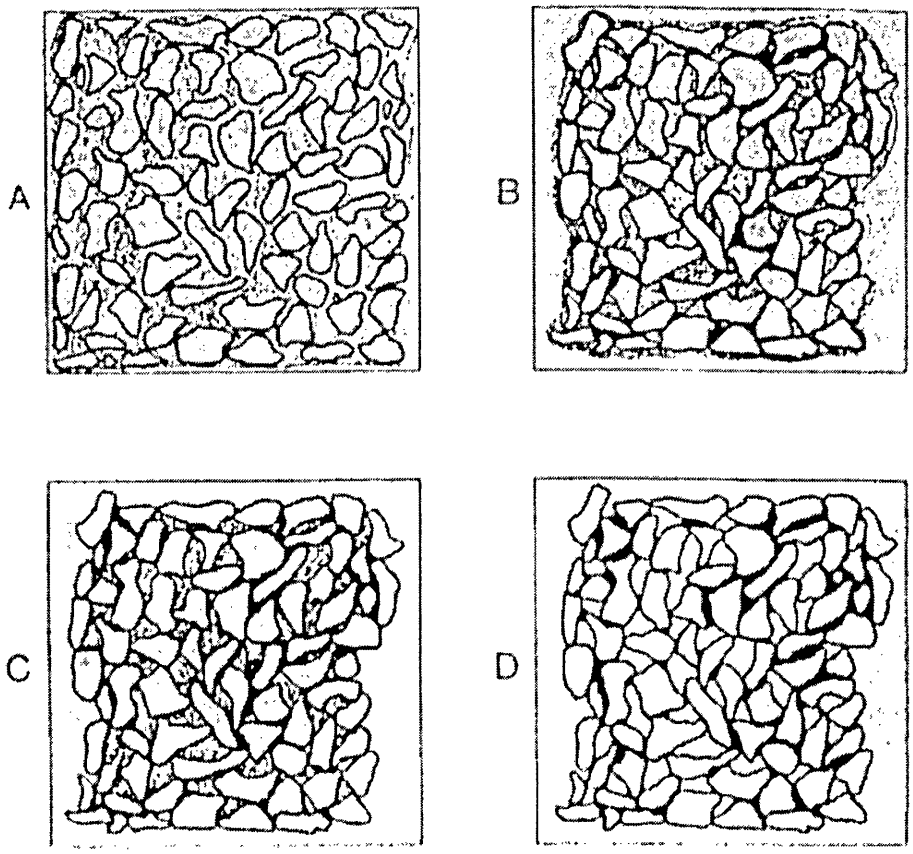

Figure 1.2: The stages of drying a ceramic body (Guerra *et al.*, 1992).

The drying mechanism depends on moisture removal in a very controlled manner, or severe cracking or warping can occur. Fortunately, the sequence of putting one dip on at a time allows for much greater flexibility in drying, as the slurry layer is thin and spread over a wide area. Also, the stucco layer (granular particle of refractory) acts to slow down the rate of drying on each individual dip by covering much of the surface of the slurry. Nevertheless, low relative humidity or excessive air movement can cause cracking. One reason often given for this occurring is drying too rapidly during which excessive moisture gradients are generated within the matrix, leading to high hygrothermal stress levels.

Figure 1.2 shows the drying process with regard to the ceramic particles. Figure 1.2 (A) shows a group of particles separated by a large amount of water, which would be the case when a cluster has just been dipped. Figure 1.2 (B) is when some of the water has been removed. Some shrinkage has occurred, and many of the particles have

started to touch. In Figure 1.2 (C), drying shrinkage has stopped, as all the particles have made at least some contact with other particles. A great deal of water is left in the pores and at interparticle contacts. In Figure 1.2 (D), most of the readily accessible water has been removed. Some liquid remains in small capillaries along with physically adsorbed water. A full description of drying can be found in many texts on drying where models are drawn from well known drying theories, such as by Scherer (1990), Whitaker (1977) and Luikov (1975),

The amount of water to be removed from the shell mould also depends on the amount of water contained in the slurry. Low viscosity slurry will have a greater amount of water and thus will allow more water to soak into the previously dried coats and will soak further back into the shell mould structure. The length of time that the mould is immersed into the slurry will also increase the amount of soak back that occurs. Immersion for a short time (e.g. 10 s) may result in de-lamination due to insufficient binder soaking into the previous coats. Excessive wetting occurs when the moulds are immersed for longer periods resulting in softening of the previously dried coats and also increasing the amount of water to be removed during drying

Drying of the shell moulds after the seal coat has been applied is required in order to remove the remaining moisture. Failure to remove the mositure content from the inner coats will result in the moisture rapidly expanding as it turns into steam during the de-wax cycle damaging the primary coat and inner secondary coats. The final firing stage in shell formation is undertaken to develop its strength as well as ensuring that the mould is completely dry during which bound water will be removed from the mould. This stage of drying in which bound water is removed will not be considered within this work.

1.2 Side effect of drying ceramic shell body

In the drying of ceramic porous material, the removal of moisture can cause shrinkage and warping which may lead to failure (Scherer, 1990). Shrinkage is caused primarily by self-contraction of the material as moisture is removed from the ceramic body. If

the shrinkage is anisotropic or hindered, the drying material may warp and crack. Normally, tension tends to be greater near the drying surface (because the outer surface tends to contract faster than the interior) which produces a differential shrinkage of the solid that will cause cracking.

Cracking of a slurry and porous network is most likely to occur at the end of the constant rate period, i.e. the critical point when shrinkage stops (Scherer, 1990). As mentioned previously, during this period liquid flows toward the outside to prevent exposure of the slurry porous network. As the liquid stretches to cover the solid phase it goes into tension (concave meniscus form). The tension P is balanced by compressive stresses on the solid phase that tends to suck the network under the surface of the liquid. The radius of curvature of the meniscus which is related to P is initially much larger than the pore radius. A fast evaporation rate and a stiff network leads to a greater tension, pulling the network together. Therefore, as long as the network is sufficiently compliant, the liquid vapour interface remains at the exterior surface of the body. However, the maximum pressure that the liquid can exert is related to the pore size of the network. The critical point is reached when the tension in the liquid cannot compress the network fast enough for the contraction rate to match the rate of evaporation. Also the physical contact between particles will ultimately lead to a system that will not contract further. This process is depicted schematically in Figure 1.3.

Also, during the constant rate period the tension in the liquid compresses the network and induces flow from the interior. For the meniscus to remain at the surface of the network, the rate of evaporation must equal the liquid flux to the surface, which is given by Darcy's law in the form of surface flux as shown below:

$$J_{surface} = \frac{K}{\mu} \nabla P \tag{1.1}$$

where ∇P is a pressure potential gradient, K is the permeability of the network and μ is the dynamic viscosity of the liquid. The lower the permeability, the more difficult it is to draw liquid from the inside of the body, and therefore the greater the pressure gradient that develops to support a greater evaporation rate. The reason that slurries

are more difficult to dry than ordinary ceramics is that their permeability is very low.

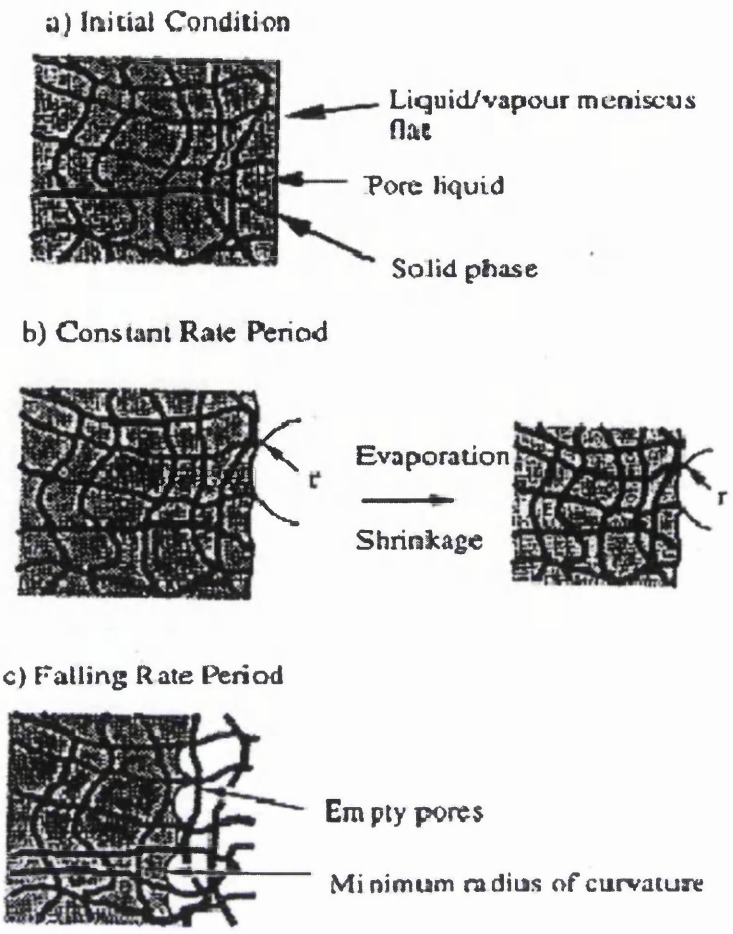

Figure 1.3: Schematic illustration of the drying stages in the pore network (Scherer, 1990).

Other factors that contribute to cracking during the shell building process is the role of the firing and drying time which may lead to variation in shrinkage in every layer of shell having a different orientation (Guerra *et al.*, 1992). As reported by laboratory works on the shell layer build up process, a small temperature fluctuation may develop during the shell build up process due to the effect of the latent heat of evaporation in every repetition of the dipping process. The fluctuation that occurs during each coating operation may therefore cause each individual coat to crack, producing a source of weakness through the shell mould thickness (Leyland and Jones, 1994). The damaged section will then be prone to cracking during the

dewaxing stage as well as surviving the rigours of handling during the shell building process (Schiefelbein, 1987).

1.3 Research motivation

A thorough understanding of the mechanisms that govern ceramic shell drying process not only can avoid failure, but facilitate and design the drying cycle for every layer and thus lead to more precise moulds (Leyland, March 1996). Therefore, research into the drying of ceramic shell moulds should lead to improved production rates and lower operational cost through scrap reduction and time lost. One way of deepening understanding is by developing mathematical models that are incorporated into a numerical solution to give a good prediction of the important variables, such as temperature, moisture, gas pressure etc and their variation during the drying time.

Such a mathematical modelling process will also lead to prediction that will aid experimentation improvement in the drying performance and guide the choice of the various kinds or properties of material to be used. Besides this advancement, it allows the complex mechanisms that take place to be predicted and investigated, such as the mechanism of the water soak back into previous coats during the drying of the shell system. Other important or interrelated parameters also can be predicted during this period. This modelling also enables the investigation of drying for various geometries i.e. linear and corner sections that will underpin modelling of full scale complex geometries.

Most experimental methods and results in drying are concerned with determination of drying kinetic curves, since a knowledge of the drying kinetics is necessary for drier design. Drying kinetics are connected with the changes of average material moisture content and average material temperature with time. This is in contrast with drying dynamics that describe changes in the temperature, pressure and moisture profiles throughout the drying body. Drying dynamic variables are very important in describing the drying mechanism (capillarity, diffusivity or convection). Therefore the development of a mathematical model through integrating these dynamic variables

that incorporate the governing equations of heat, moisture and gas transport provides an attractive possibility to investigate drying of a porous ceramic shell.

Therefore, the motivation of this study is to establish a process simulation tool based on a comprehensive model, implement this within a numerical framework and to undertake a validation of this scheme where it is possible to do so.

1.4 Objectives of the project

Based on the preceding discussion, the present research effort was undertaken with the following objectives:

1. To develop a theoretical formulation in two dimensions to describe two phase flow, with fully coupled heat, mass and gas transport for a nonhygroscopic porous system for drying of a ceramic body particularly for drying a ceramic shell mould system.

2. To develop a numerical solution of the above fully coupled theoretical form using a combination of a finite element formulation and a finite difference time stepping algorithm for predicting the important variables such as temperature, moisture, pressure, permeability, and relative humidity and etc. variation during the drying of the ceramic porous body.

3. To develop a model to capture the drying of a single and multilayer shell.

4. To verify the model against analytical solutions and to validate the numerical model against experimental studies and previously published numerical results.

1.5 Research contributions

In this work, the fully coupled, heat, mass and gas transport governing equations was developed based on a continuum framework. This model provides a systematic way to incorporate transport through convective and diffusive mechanisms. The derivation of the transport equations is based on the drying working parameters such as temperature, gas and pore water pressure that can be measured within laboratory experiments. The advancement offered in this work is the development and application of a comprehensive model that is based on geomechanics to an industrial drying problem. This model may be contrasted against the previous work that used the irreversible thermodynamic modelling approach proposed by Malan (September 2002) in which he recommended that material properties of the shell need to be determined based on a phenomenological approach.

This fully coupled set of transport equations was succesfully implemented. The numerical simulation was benchmarked against analytical studies on heat transfer, brick drying and drying of single and multilayer shells. The latter represents a first attempt at an 'ab initio' simulation of a multi layer shell drying process. The contour results provide a valuable insight to the dynamic variation of process variables during the drying process.

1.6 Outline of the thesis

The thesis is organized into seven chapters. In the first part of Chapter 1, a short introduction of the importance of the drying process and possible failure mechanisms that are always present in the ceramic shell build up process has been presented. An introduction to the ceramic shell mould making process is also included in here. Some objectives of the works, research motivations, research contributions and an overview of the Chapters are also presented.

In Chapter 2, the theoretical and numerical modelling developments are explained and

illustrated in connection with the drying process. This traces their evolution and application, mainly in other fields. Some characteristics of drying in porous systems are also explained. This chapter also includes a short introduction to the well known basic drying models and their extension, for example to include temperature gradient influences, together with models based on irreversible thermodynamics are also discussed. Comparisons, limitations and advantage of the reviewed models are illustrated in connection with the drying process.

In Chapter 3, a range of material properties required by the theory developed in Chapter 4 is presented. Ceramic bodies (brick and ceramic shells) can be represented by a three-phase system comprising liquid, gas (vapour and air) and solid particles which may contain water in bound and unbound form. This chapter focuses on the material properties and transport processes (heat, mass and gas) that are used for simulating the benchmark problems and for simulating ceramic shell drying.

In Chapter 4, a full derivation of the coupled heat, mass and gas transport equations in a two dimensional framework is presented. This partial derivation of the coupled equation is based on the temperature, moisture, pore water potential and gas pressure gradient. Generally, this formulation is follows the approach advocated in Whitaker's model. The sets of coupled equation consist of the constitutive derivative of their transport equations, material properties, thermodynamic state equilibrium etc., which have been presented in Chapter 3.

The set of the partial differential of the coupled governing equations presented in Chapter 5 sets out the equation solution by the Finite element method (for the spatial discretization) and difference time stepping algorithm (for the time discretization). The discretization process transforms the nonlinear partial differential equations where the unknowns are state variables at a discrete points in space. This is followed by implementing a fully implicit backward time stepping scheme. The skyline solver is used to manage the storage capacity required and the solution of the coupled problem is achieved by an iterative method.

In Chapter 6, validation of the proposed model is tested. Validation is achieved by comparison against benchmark problems ranging from the simple linear heat flow for

which the results compared well with the analytical solutions. Validation of the fully coupled heat, mass and gas transport problem is also presented for a documented study on brick drying, for which good agreement is again achieved. The coupled scheme is then implemented to simulate the shell drying process. This involves the isothermal drying of a plain linear shell section which is compared with industrial experimental work. This includes single and multi layer shells. This simulation shows a correct trend rather than close absolute agreement. For now, the lack of agreement has been attributed to the absence of good material model data. This shell drying simulation is then extended to a corner shape geometry that shows the moisture transport process under more complex geometric conditions.

Finally, Chapter 7 discusses the overall conclusions derived from this work, and makes pertinent recommendations for future work to extend and develop this research.

REFERENCES

Guerra, M., Roberts, W.O., and Bozzo, A.T., 1992, DuPont, Factors Affecting Shell Strength and The Effect of Dry Time on Shell Strength: 22nd EICF Conference, Paris.

Hyde, R., October 1995, The Rupture of Ceramic Moulds for Investment Casting: PhD Theses, University of Birmingham, Birmingham.

http://www.P.I.Casting/ Investment Casting Process .

Jones, S., February-June 1994, COST 504 European Collaborative Research Programme: *in* Rolls-Royce plc and The University of Birmingham, p. 10.

Jones, S., and Leyland, S., 1994, Investigation into The Drying Behaviour of Water Based Slurries: I.C.I 42nd Annual Technical Meeting.

Jones, S., and Marquis, P.M., 1995, British Ceramic Transaction Journal, v. 94, p. 68-73.

Leyland, S., and Jones, S., 1994, The Effect of Drying Conditions Upon the Wax/Ceramic Interface Temperature: In Internal Report for Rolls Royce plc.

Leyland, S., March 1996, Research Procedures and History of The Water Based Shell Development Programme, Rolls-Royce Plc and PCF-Derby.

Luikov, A.V., 1975, Heat and Mass Transfer in Capillary Porous Bodies; Oxford Pergamon.

Malan, A.G., September 2002, Investigation into the Continuum Thermodynamic Modelling of Investment Casting Shell-Mould Drying: PhD Theses, University Of Wales, Swansea.

Roberts, W.O., and Delaware, W., 1995, Ludox SK-R as A Replacement for Ethyl Silicate: Investment Casting Institute.

Scherer, G.W., 1990, Theory of Drying: Journal of American Ceramic Society, v. 73(1), p. 3-14.

Schiefelbein, W.G., 1987, Ceramic Shell Production for Controlling Shell Cracking.

Whitaker, S., 1977, Simultaneous Heat, Mass and Momentum Transfer in Porous Media; A Theory of Drying: Advances in Heat Transfer, v. 13, p. 119-203.

CHAPTER 2

DRYING PROCESS IN POROUS MEDIA

CHAPTER LAYOUT

This chapter consists of several sections which review the most pertinent work that is relevant to the drying process that takes place in a porous ceramic media, especially in the application to ceramic shell drying that forms part of the investment casting process. An introduction to porous media was set out in Chapter 1 and this provides an outline to support the explanation and description in this chapter. A description of the physical variables, controlling parameters and thermodynamic reactions in the porous system and its interaction with the ambient conditions need to be included in order to have a better illustration of the drying mechanism. A description of drying is often summarised in the form of a drying curve which depicts the stages in the drying process. On a more detailed level, the coupling of heat, mass and gas transport mechanisms enables a more complete scientific description of the drying process, especially when incorporated with the moving evaporation boundary inside the body and moving boundary condition in the drying environment.

2.1 Introduction.

The drying process is energy intensive and is probably one of the least understood. Since phase change is often concurrent with the drying process in porous media, moisture can exist in a number of forms, including, liquid, vapour at a range of saturations that can tend to be a gas when dry. Furthermore, moisture transport within a porous medium becomes very complicated especially as pores assume a small size which may also contribute to hygroscopicity, bound water, moisture in multimolecular and monolayer layer etc. (Keey, 1975). Thus, the drying process needs a quantitative understanding of the physics involved that will include transport phenomena in all phases. This is relevant to shell drying in the investment "precision" casting manufacturing process, where attempts have been underway to improve investment casting ceramic shell-mould integrity through increasing the understanding of the drying process involved and its complicated porous structure interaction (Jones *et al.*, 2003; Chakrabarti, 2002).

In order to theoretically describe the flow of moisture and heat through a porous medium, it is necessary to introduce and describe the structure of a porous body. Generally, a porous medium consists of intercellular spaces or voids which are interconnected and filled with air and a certain amount of free water. The cells themselves also contain water, which is also called bound water. The cellular membrane behaves like a perfectly semi-permeable structure and may act as a capillary path or for the bound water to migrate (as shown in Figure 2.1). When the water content is lower than the maximum irreducible water content, water will exist as bound water in the pores. However, when the water content exceeds the maximum irreducible water content, water will exist as free water and form a water ring, which may be continuous or discontinuous depending on the level. Other factors that contribute to water flow inside and outside of the porous medium (especially in the case of drying or under temperature gradient) include parameters such as the molecular forces in the capillarity flow, dynamic phase change in the pore and at the boundary that forms the moisture interface and hygrothermal equilibrium mechanisms within the capillary network (when interacting with specified ambient conditions).

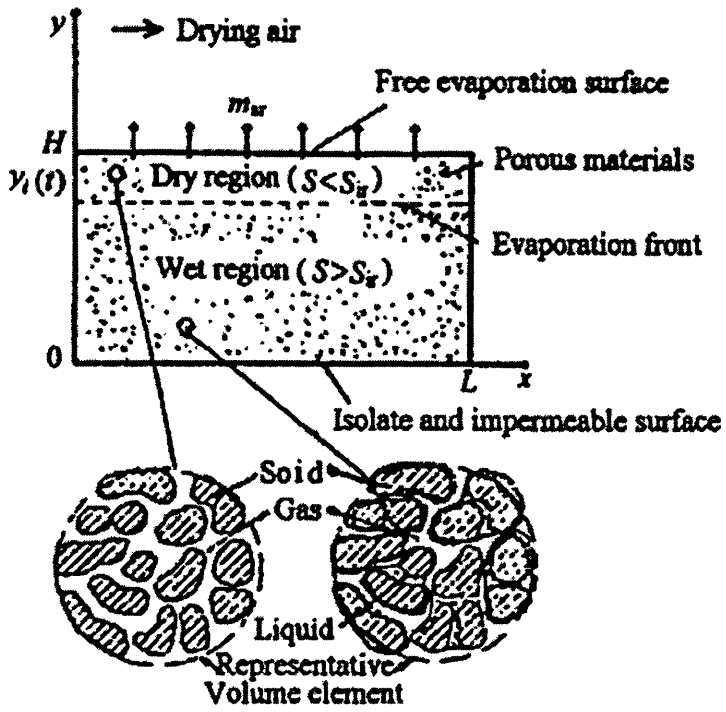

Figure 2.1: Schematic of the drying model (Zhang, 1999).

In general, most of the drying works presented transport mechanisms (heat, moisture and gas) that is culminated in the form of a drying curve. The more recent and the most widely accepted qualitative explanation accounting for the characteristic drying curve is given by Scherer (1990). He suggests that in the constant rate period of drying the evaporation of water occurs at the surface of the material in a manner similar to evaporation from a free water surface. Moisture exerts its full vapour pressure, and the migration of the moisture is determined primarily by capillarity, and thus is independent of moisture content up to saturation (sometimes this is known as saturated drying). The falling rate period begins when depletion of water in the interior starts and the resistance to internal liquid movement becomes significant. The early stage of this period is characterized by "unsaturated surface drying". Later in the falling rate period, the plane of evaporation retreats into the interior of the material. As drying proceeds the water removal continues and finally the body approaches the second falling rate period where the removal of bound water takes place under

circumstances of strong hygroscopic action. This mechanism clearly shows the movement of liquid water from the interior of the porous system to a plane of evaporation at or toward a surface, which may also describe the evaporation front. Theoretically this evaporation front divides the system into two distinct zones: the wet and the dry zone as shown in Figure 2.2. In the dry zone, the free water content is zero and the main mechanism of moisture transfer is vapour flow. However in the case of hygroscopic material, the dry zone is called the sorption zone due to the adsorptive nature of moisture retention. The general form of the drying curve as described in many drying books (Keey, 1975; Luikov, 1975) and in many papers that deal with drying (Scherer, 1990; Sherwood, 1929) is shown in Figure 2.2).

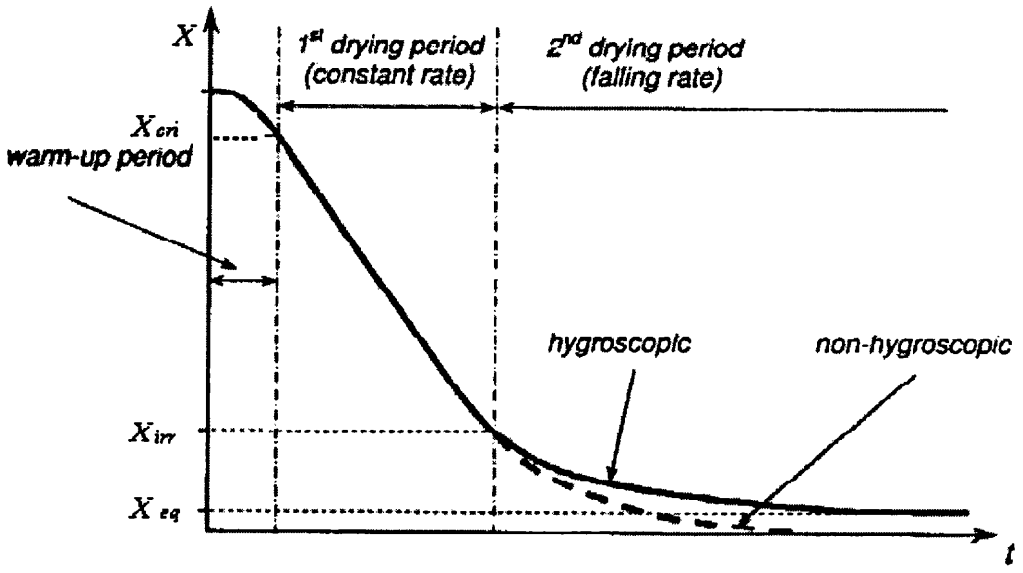

Figure 2.2: Drying curve ; an average moisture content versus time (Keey, 1975).

It is very important in drying of all porous materials to know the internal interactions that occur within the porous medium and the drying environment. Therefore the complete analysis of drying can be generally viewed to comprise several phenomenological considerations. Mainly, this involves the introduction or transfer of heat into the porous system, the transfer or movement of heat and mass (liquid or gaseous phases) within the porous system, and the removal or mass transfer of water vapour from the system through the outer surface. Obviously, all three phenomena are

coincidentally associated with any drying operation as described in many drying textbooks (Keey, 1975; Luikov, 1966). The first and last are primarily dependent on the mode of the drying employed, i.e, air drying, convective drying, hot surface drying, etc. They are referred throughout this thesis as boundary conditions. The second or middle factor, although affected by the boundary condition, is the characteristic of the porous system being dried. As mentioned earlier, drying of porous bodies involves complicated interactions that include dynamic phases and transport mechanisms of diffusion, convection and latent heat. Contributions from these transport mechanisms characterize the drying stages captured by the drying curve that has been modelled previously and implemented in several works (Stanish *et al.*, 1986; Zhang, 1999).

A complete analysis of drying involves representing the transport of heat, moisture and gas accounting for the interaction of all these mechanisms inside and outside of the body. A review of a sample of the most pertinent previous literature has showed that the transport mechanism in porous bodies has been modelled in several ways. For example, early investigation considered that liquid movement occurred as a result of diffusion under the influence of liquid concentration or moisture gradient without a heat transport gradient (Lewis, 1921). Then, this model was improved by including the coupling of heat and mass transfer (Luikov, 1966; Philip and de Vries., 1957). Recently, more complete models have been derived that account for simultaneous heat, mass and gas transport (Luikov, 1975; Whitaker, 1977). This complete model accounts for all phenomena in terms of temperature, moisture and gas and these are strongly inter-dependent. In fact it gives the best representation of the transport mechanisms in the theoretical drying model and good elaboration of the stages in the drying process as captured by the drying curve. Furthermore, some of the numerical drying models that had been published recently also couple transport in the porous body interior with transport in the form of flow around the external surface (Murugesan *et al.*, 2000).

2.2 Background of the drying model

In describing the drying of porous media, several view points have been postulated by previous researchers and scientists. Basically, there are several approaches that involve and contribute to the drying model development and these are given in the following paragraphs.

Early drying studies are commonly characterized by considering the rate of drying as a function of the moisture content of the material being dried. The general curve of this early characteristic of simple drying is given in Figure 2.3 and has been found to apply presumably without exception, to all types of materials without regard for the particular drying condition employed. This typical or characteristic drying curve has resulted in the nomenclature which refers to a short heating up period leading to a constant rate period which continues to a critical moisture content at which point a falling rate drying period is inaugurated.

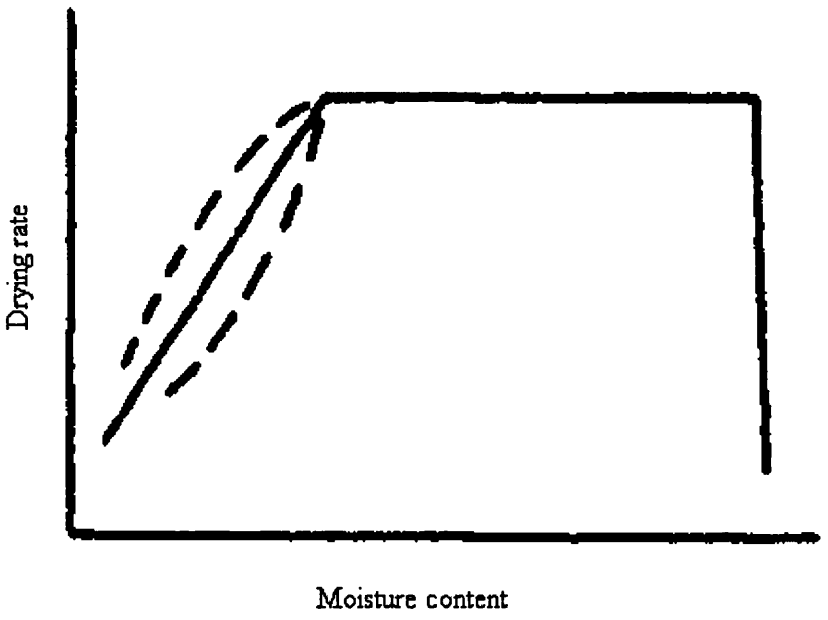

Figure 2.3: Characteristic of the simple drying curve (Higgins, 1951).

This early literature on drying deals only with the effect of boundary conditions on drying rate (Higgins, 1951; Keey, 1975). There are several methods that have been used previously to establish the drying rate. One of the most widely implemented and

still used until now is based on a gravimetric method. This is used in developing the simple drying curve, where it involves the measurement of water loss from the moist body over an increment of time where smaller increments lead to a more accurate drying curve. In fact this classic measurement is still used today in many important fields such as in soil, building, food and also in the ceramic shell build up process (Chakrabarti, 2002; Jones and Leyland, 1994). This simple measurement of drying can sometimes be supplemented, dependent on the scope of the experiment. Examples include placing a highly sensitive thermocouple to capture thermal data and a probe that uses a conductivity principle to measure moisture within the porous body. Recording this data is very important when attempting to establish an accurate benchmark dataset as demonstrated in several works (Kallel *et al.*, 1993; Shushang and Keey, 1994; Stanish *et al.*, 1986).

However this simple measurement is still very limited because it reflects the influence of boundary conditions on drying and not the transport mechanisms and the factors that influence them. Measurement of these properties becomes very challenging due to the fact that the porous medium is heterogeneous and contains multiple phases. Unless care is taken, this simple measurement of the drying can lead to the wrong interpretation especially in the drying porous medium. This had been demonstrated through drying models (Scherer, 1990; Sherwood, 1929) and experimental work under temperature gradient condition (de Vries, 1958). Most of them elaborated the drying measurement in terms of the thermodynamic and the thermo physical equilibrium in the porous section with consideration of the different phases (Scherer, 1990) through integrating the experimental measurement with the theoretical concept.

While questions about these simple theories were being raised, researchers turned their attention to search more elaborated models. Early attempts to solve the drying of a porous body using a transport analysis included both heat and mass mechanisms. Due to the fact that simultaneous heat and mass transfer is a complex process, the first attempts to solve the problem neglected the thermal dependency of mass transfer or mass dependency of heat transfer. However, Philip *et al.* (1957) and Luikov (1966) revealed that the moisture diffusion equation alone is not adequate for describing moisture movement in drying of any porous medium or in any porous system that is subjected to a temperature gradient. Thus, the transfer of moisture and heat must be

considered simultaneously in drying of a porous system. Basically, theories of coupled heat and mass transport phenomena in porous media come either from a mechanistic approach (de Vries, 1958; Philip and de Vries., 1957) or from irreversible thermodynamic concepts (Luikov, 1966). With the number of governing equations increasing and the physical properties that are contained within the 'material model' becoming more complex, the application range of these types of coupled models widens.

Luikov (1966) extended the previous treatment of the diffusion model by including effects of capillary flow and vapour transport. In his work, the thermal energy equation was also incorporated into the set of the governing equations. This set of equations represents the combination of moisture and temperature flow. He developed a set of equations and expressing conservation of mass for the moisture as well as conservation of energy by employing the principles of irreversible thermodynamics. Following the presentation set out in Equation (2.1), the basic assumption of irreversible thermodynamics is that Gibb's equation, which was derived and proven for equilibrium conditions, is a good approximation for low rate heat and mass transfer. For an incompressible system (assuming that all gases may be approximated as being pressure incompressible) this equations reads

$$Td\theta = d\gamma - \sum_{\alpha} k_{\alpha} d\eta_{\alpha} \tag{2.1}$$

where θ denotes entropy, γ internal energy, k_{α} is a chemical potential of phase α and n the number of moles. This relation contains the two mechanisms encountered in drying, via heat and mass transfer.

For pure heat transfer the thermodynamic potential follows from the change in entropy, or $Td\theta = d\gamma$,as

$$\Phi_q = \nabla\left(\frac{\partial\theta}{\partial\gamma}\right) = -\frac{1}{T^2}\nabla T \tag{2.2}$$

where the thermodynamic force is a function of temperature gradient.

For the case of isothermal mass transfer of a species α, the thermodynamic potential derived from Equation (2.1) follows

$$\Phi_m = \nabla\left(\frac{\partial\theta}{\partial \mathrm{M}_\alpha}\right) = -\nabla\frac{k_\alpha}{T} \tag{2.3}$$

where the magnitude of the thermodynamic force is a function of the gradient of both the chemical potential and absolute temperature.

This thermodynamic force is the force that causes irreversible phenomena such as the transfer of heat and mass to occur. In general, any transport phenomenon is governed by the action of all the thermodynamic forces and therefore it is assumed that each flux is linearly related to the force by

$$J_\chi = \sum_\zeta \langle L_{\chi\zeta}\rangle\langle\Phi_\zeta\rangle \qquad \text{for } \chi = l,v,g \tag{2.4}$$

This expression is known as Onsager's system of linear equations and it is the principal expression of the thermodynamics of irreversible processes. The coefficients $L_{\chi\zeta}$ are known as 'phenomenological' because they are determined by the rate at which the phenomena proceeds. The generic coupled equation states that heat transfer depends not only on thermal conduction but also the redistribution of mass (Dufour effect) while mass transfer is governed not only by differences in chemical potential, and thus concentration of matter, but also by thermal diffusion (Soret effect).

$$J_q = \frac{-L_{11}}{T^2}\nabla T - L_{12}\nabla\left(\frac{\mu}{T}\right) \tag{2.5}$$

$$J_m = \frac{-L_{21}}{T^2}\nabla T - L_{22}\nabla\left(\frac{\mu}{T}\right) \tag{2.6}$$

The employment cross-coefficients are equal and symmetrical for both the heat and mass transfer; the effect of unequal concentrations of matter on heat-energy flow is symmetrical to that of temperature differences on mass flow, i.e $L_{\chi\zeta} = L_{\zeta\chi}$. Therefore these expressions of coupled governing equations are governed by correct definition of thermodynamic forces. Unfortunately these equations are not easily applied since the chemical potential is not an easily determined quantity. More useful expressions have been obtained by Luikov's approach by replacing the thermodynamic force or the thermodynamic state by moisture content and temperature. This coupled

interrelation between liquid and heat transfer are governed by two separate differential equations (Fourier's equation for heat transfer and Fick's equation for mass transfer).

$$J_q = k_{11}\nabla T - k_{12}\nabla m \tag{2.7}$$

$$J_m = k_{21}\nabla T - k_{22}\nabla m \tag{2.8}$$

The outstanding issues in the completion of the set of governing equations are obtaining expressions for the phenomenological coefficients (Lewis *et al.*, 1996). Although such a treatment makes the process easily understood, it is more difficult to obtain the coefficients parameters that Luikov introduced in the governing equations of heat and mass transfer. In addition, some coefficients do not represent physical properties of the materials, but are process variables such as 'phase change coefficients'. This makes it very difficult to establish material parameters that are required for the simulation process.

Meanwhile, Philip and de Vries (1957) and de Vries (1958) extended the previous diffusion model by including the effects of capillary flow and vapour transport. In their work, the thermal energy equation was also incorporated into the set of the governing equation to describe the drying process. This set of coupled equations was treated under the combination of moisture and temperature gradients. In this approach, the coupled partial differential equations of mass and energy are always presented as the overall thermal mass diffusivity (as shown in Figure 2.4) and the overall isothermal mass diffusivity along with the consideration of the convective energy terms are negligible. The obtained systems consist of diffusion-like equations whose coefficients must be determined by experiment. The capillarity action is macroscopically described by Darcy's law and the gravity potential. The diffusion transport of water vapour by molecular diffusion is described as Fick's law by using the simple theory of vapour transfer. They introduced some extended treatment of vapour transfer by substituting the thermal diffusivity of vapour flux is due to the average microscopic temperature gradient in the pore section. In general, this expression of diffusive terms are functions of porosity and moisture content which can be determined experimentally. Later then, this microscopic vapour transport was extended by Ewen *et al.* (1989). In this work some validation of isothermal and

thermal diffusivities according to the liquid and vapour transport of the proposed model and experimental values were examined and a good agreement was concluded.

Most of the previous studies which are based on two-way coupled heat and mass transfer model assumed that pressure was constant throughout the drying body. However they were claimed to be successfully employed to simulate temperature and moisture movement in the drying process (Kallel *et al.*, 1993; Murugesan *et al.*, 2002). Despite this, there remains a question about the effect of pressure gradient on the heat and mass transfer, as to whether diffusion moisture movement is caused by a moisture gradient or a vapour transport as a consequence of a gas pressure gradient. It was then proved theoretically (Luikov, 1975), experimentally (Lewis and Schrefler, 1998) and numerically (Ilic and Turner, 1989; Lewis and Ferguson, 1990; Lewis and Schrefler, 1998) that a pressure gradient develops inside the capillary porous body, which causes moisture movement by filtration in addition to moisture transfer by diffusion (Hyde, October 1995). As for example the work presented by Thomas *et al.* (1980) was expanded upon by Ferguson (1991) and Lewis and Ferguson (1990) to include the effect of pressure gradient. In the latter works, the approach is based on Luikov's work or based upon on irreversible thermodynamics. As examples, these were applied to timber drying and an encapsulated electronic circuit. With comparison between a two component model (a model with coupled heat and mass transport) and a three component model (model with coupling of heat, mass and gas transport), they found that during a period of intense drying the gas pressure gradient was shown to have a significant effect on the rate at which the temperature and moisture content reach steady state conditions They concluded that because of the marked gas pressure difference, the pressure cannot be assumed constant throughout the body. This is because the gas pressure term which is dependent upon material parameters, has a significant effect on the rate of moisture migration. This suggests Luikov's (Luikov, 1975) three phase coupled heat, mass and gas transfer model, in which heat transfer, mass transfer and pressure induced transfer are fully dependent, should be used.

Even though, Luikov's three field variable model proposed a more reasonably acceptable method, it still inherited the introduction of the unknown coefficients which are still not easy to determine experimentally or otherwise, as pointed out

previously. However, Luikov's theory provides a well-established model in the treatment of simultaneous heat and mass transfer for the drying problem based on the extensive work that has been explained under the above section. In fact this approach is still commonly employed and quite often it is solved by employing the finite element method (Keum *et al.*, 2000).

Most of the literatures and reviews of porous media indicate that the theory of Philip and de Vries provides the most comprehensive basis for the prediction of heat and moisture transfer in an unsaturated medium especially for soils. Most of the works that are based on this theory derived their constitutive capillary mechanism as a wetting curve (saturation curve), which is extensively determined and evaluated through experimental works (Ferguson and Kaddouri, 2004; Thomas and He, 1995) and similarly for the vapour movement (Ewen and Thomas, 1989). The major restriction of this coupled theory is that it does not include the gradients of gas pressure; also there is no convection contribution in the heat equation. In the case of gas pressure being treated as constant, probably this is acceptable in the most cases when the total gas pressure gradient is small such as in soils. However, this assumption may not be applicable to most drying problems, where the contribution of the gas pressure plays an important role (as mentioned previously in Luikov model). This is due to the fact that the drying model involves phase changes (such as water phase to vapour phase) and circulation of the vapour pressure (vapour phase) from the drying front to the ambient condition. This is an important part in describing the drying process.

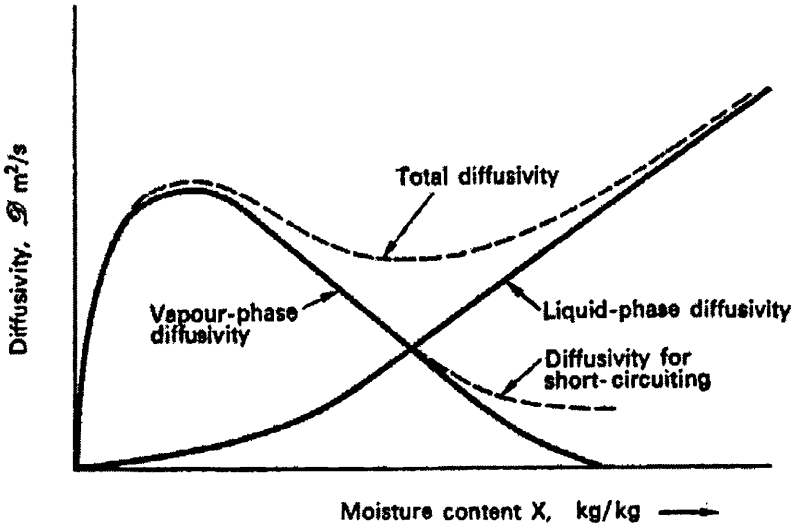

Figure 2.4: Variation of moisture diffusivity with moisture content. (adapted from de Vries (1958))

Independently of Philip de Vries and Luikov's works, Whitaker presented a set of equations to describe the simultaneous heat, mass and momentum transfer in porous media. Whitaker started from heat and mass conservation equations for each phase (solid, liquid, and vapour plus inert gas) at the microscopic level, or the representative element volume (REV). By using the volume averaging method, the macroscopic differential equations were defined in terms of average field quantities. It assumes that the physical properties of the porous medium can be associated with mathematical field variables, whose time and space dependencies are represented in the form of differential balance equations of mass, momentum and energy. The theory of Whitaker was further developed and applied in the drying analysis of various porous media, for example in the drying analysis of brick (Ilic and Turner, 1989), wood (Spolek *et al.*, 1985), sand (Whitaker *et al.*, 1983) and cellular materials (Crapiste *et al.*, 1988). In these works, the model is usually quite successfully matched against experimental data. Several listed works (Ilic and Turner, 1989; Ben Nasrallah and Perre, 1988; Nijdam *et al.*, 2000; Perre *et al.*, 1993; Zhang, 1999) have also shown that this complete set of equations based on the Whitaker continuum theoretical derivation are very good in representing the physical processes taking place in a wide range of porous systems. For example in reference (Perre *et al.*, 1993) the model was

used to simulate the transport phenomena during convective drying with superheated steam and moist air applied to the seemingly diverse systems of light concrete and softwood board. Meanwhile in reference (Nijdam *et al.*, 2000) the formulation was used to simulate a high-temperature drying model for softwood timber. In other related work, convective drying of brick with hygroscopic properties (Zhang, 1999) and nonhygroscopic properties (Ilic and Turner, 1989; Nasrallah and Perre, 1988) has been explored. In the Thermo-hydro-mechanical field, this method is widely accepted to solve a variety of slow transient phenomena involving flow of heat, water and gas in deforming porous media (Gawin, 1996) and a multiphase model of concrete drying at high temperature (Gawin *et al.*, 1998).

So with regard to the above discussion, most of the recent interest in development of drying analysis involves three field variables (temperature, moisture and gas pressure) obtained from the fundamental laws of conservation of mass, momentum and energy. The usual approaches to such an analysis have assumed that moisture moves by a range of mechanisms, including diffusion, capillarity and phase change. Heat is transported via conduction, latent heat and convection that includes contribution by gas transport, bulk flow and diffusion of the vapour. The gas phase is considered to be an ideal gas composed of dry air and vapour, which are regarded as two miscible species.

The governing equations are coupled through relationships that link the field variables with transport mechanisms that are often derived from analytical or empirical approaches. These constitutive relationships can be considered as being 'material models' as in many instances they are specific to the type of porous material that is being considered. For example, the moisture thermodynamic balance can be expressed through either the Kelvin law to describe the relationship between the pore liquid pressure, gas pressure and capillary pressure and saturation level. The saturation value can be linked directly to the gas and liquid permeability value. This approach gives a clear derivation of moisture, heat and gas transport. Furthermore, the chosen macroscopic primary variables such as gas pressure, capillary pressure and temperature correspond to real measurable quantities. In summary, this approach enables the solution of governing equations directly connected to the fluxes due to the

molecular transport mechanisms of the conserved quantities. This provides a more practical approach than Luikov, because the 'material model' may be derived through measurement of real physical quantities.

In modelling the drying process, the solution of the governing equations requires specification of boundary conditions. In their simplest form, they can be prescriptions that are linked to the field variables that reflect the drying environment in an approximate manner, for example through coefficients that reflect the average heat and mass transfer through convection at the surface. More recently surface transfer has been treated as a conjugate problem from continuum modelling point of view that allows consideration of local heat and mass transfer at the bounding surface. Thus it involves the heat and mass transfer in both the porous material and surrounding fluid flow. Also the process is transient in nature wherein the resistance to heat and mass transfer at the boundary will vary with time. Hence, the heat and moisture transfer within the porous solid should be combined with the transport processes in the surrounding flow field. Murugesan *et al.* (2000, 2001) solved the evaporative drying of a brick by treating it as a conjugate problem. The conservation equations for the solid was obtained using the continuum approach. The Navier-Stokes equations had been employed for obtaining the flow filed and the corresponding flow solutions are used for predicting the drying behaviour of the rectangular of brick, the result showed that the leading edge dried faster, as compared to other regions. This work also observed that two dimensional results differ significantly from the prediction of one-dimensional heat and mass transfer coupled with boundary layer approximations over the top surface especially in the regions away from the leading edge. In this instance, the result also indicated that it is essential to consider the buoyancy effects during forced convection drying of the brick.

Some works related to the conjugate drying problem with relevance to shell drying have also been explored. The thesis presented by Malan (September 2002) explored the isothermal drying of a brick. The emphasis of his innovation was on fluid flow modelling in which he proposed the use of an unstructured edge-based finite volume artificial compressibility modelling algorithm that was evaluated on a number of flow problems. The method proved accurate and robust (stable) when applied to inviscid,

as well as viscous flows ranging over a wide range of Reynolds and Rayleigh numbers. The proposed edge-based convective flux averaging procedure was found to result in a notable improvement in spatial accuracy. This fluid flow solver was then coupled with the model for the drying body. For both cases of a drying brick and extruded corn-meal the predicted temperature and moisture evolutions were successfully validated against experimental data. However, to date, such conjugate solutions have been applied to simple geometry and do not reflect the complexity of ceramic shells used in investment casting. Extension to such geometry still remains a challenge.

2.3 Closure

Following from the preceding review, the focus of the work in this thesis is to develop and test a comprehensive model for drying of an investment casting ceramic shell that will also include consideration of a multilayer system. Recent studies on improving the understanding of the shell making process have only focused on the effect of drying condition either by controlling the relative humidity, temperature and air flow velocity (Chakrabarti, 2002; Jones and Leyland, 1994). Usually the performance of the shell mould is measured by MOR (Modulus Of Rupture) evaluation (Hyde, October 1995). Also unfortunately, most of the works that have been done are not fully documented (Leyland and Jones, 1994; Leyland, 1996). Even until now, there are only a limited number of attempts to undertake the complete investigation of transport mechanisms in shell drying. Because of the underlying complexity of this process, this can only be achieved most effectively through application of simulation.

Therefore, in this work, effort has been put in to explore the combined heat, mass and gas transport mechanisms in ceramic shell drying. This may be contrasted against the work that has been done by previous researchers (Malan, September 2002) in which the scope focused on the development of a drying model using a mathematical formulation expressed via a volume averaged equation in one dimension. This excluded both multiple layers and the gravitational effect. Furthermore, much of the work has concentrated on the developing of the accuracy of algorithms (Malan, September 2002; Malan and Lewis, 2003) rather than exploring transport mechanisms and their influence on the drying process. Thus few of the numerical investigations presented so far explore the importance of evolution of influence variables such temperature, saturation level etc during the shell drying process. There are no studies on modelling drying in multilayer shell systems.

REFERENCES

Ben Nasrallah, S., and Perre, P., 1988, Detailed Study of A Model of Heat and Mass Transfer During Convective Drying of Porous Media: International Journal Heat Mass Transfer, v. 31, p. 957-967.

Chakrabarti, B.K., 2002, Drying Conditions and Their effect on Ceramic Shell Investment Casting Process: Material Science and Technology, v. 18, p. 935-940.

Crapiste, G.H., Whitaker, S., and Rotstein, E., 1988, Drying of Cellular Material-I. A Mass Transfer Theory: Chemical Engineering Science, v. 43, p. 2919-2928.

de Vries, D.A., 1958, Simultaneous Transfer of Heat and Moisture in Porous Media: Trans. Am Geophys Union, v. 39, p. 909-916.

Ewen J., and Thomas H.R., 1989, Heating Unsaturated Medium Sand: Geotechnique, v. 39, p. 455-470.

Ferguson, W.J., and Kaddouri, A., 2004, A Mass Conservation Non-Isothermal Subsurface Three-Phase Flow Model: Formulation and Application: Water, Air and Soil Pollution, v. 153, p. 269-291.

Ferguson, W.J., 1991, A Finite Element Model for Heat and Mass Transfer in Capillary-porous Bodies with Particular Reference to The Influence of Pressure Gradient: PhD Theses, University Of Wales.

Gawin, D., 1996, Thermo-hydro-mechanical Analysis of Partially Saturated Porous Materials: Engineering Computations, v. 13, p. 113-143.

Gawin, D., Majorana, C.E., Pesavento, F., and Schrefler, B.A., 1998, A Fully Coupled Multiphase FE Model of Hygro-thermo-mechanical Behaviour of Concrete at High Temperature: Computational Mechanics.

Higgins, J., 1951, A Study of Air Drying of Paper, The Institute Paper of Chemistry: Doctor's Dissertation, Appleton, Wis

Hyde, R., October 1995, The Rupture Of Ceramic Moulds for Investment Casting: PhD Theses, University of Birmingham, Brimingham, England.

Ilic, M., and Turner, I.W., 1989, Convective Drying of A Consolidated Slab of Wet Porous Material: International Journal Heat Mass Transfer, v. 32, p. 2351-2362.

Jones, S., Jolly Blackburn, M.R., Gebelin, S., Cendrowicz, J.C., and Lewis, K., July 2003, Effect of Moisture Upon Mechanical Properties of Ceramic Moulds During High Pressure Steam Dewaxing: Material Science and Technology, v. 19, p. 907-914.

Jones, S., and Leyland, S., 1994, Investigation into The Drying Behaviour of Water Based Slurries: I.C.I 42nd Annual Technical Meeting.

Kallel, F., Galanis, N., Perrin, B., and Javelas, R., 1993, Effects of Moisture on Temperature During Drying of Consolidated Porous Materials: Transaction of The ASME, v. 115, p. 724-733.

Keey, R.B., 1975, Drying Principles and Practice: Great Britain, Pergamon Press.

Keum, Y.T., Jeong, J.H., and Auh, K.H., 2000, Finite Element Simulation of Ceramic Drying Processes: Modelling Simulation Material Science Engineering, v. 8, p. 541-556.

Lewis, R.W., and Ferguson, W.J., 1990, The Effect of Temperature and Total Gas Pressure on The Moisture Content in A Capillary-Porous Body: International Journal Numerical Method Engineering, v. 29, p. 357-369.

Lewis, R.W., Morgan, K., and Thomas, H.R., 1996, The Finite Element Method in

Heat Transfer Analysis: West Sussex, England, John Wiley & Sons.
Lewis, R.W., and Schrefler, B.A., 1998, The Finite Element Method in The Static and Dynamic Deformation and Consolidation of Porous Media: England, Wiley.
Lewis, W. K., 1921, The Rate of Drying of Solid Materials: Ind. Eng. chem, v. 13, p. 427-432.
Leyland, S., and Jones, S., 1994, The Effect of Drying Conditions Upon The Wax/Ceramic Interface Temperature: in Internal Report for Rolls Royce plc and School of Metallurgy and Materials.
Leyland, S., 1996, Research Procedures and History of The Water Based Shell Development Programme: in Internal Memorandum Rolls-Royce plc.
Luikov, A.V., 1966, Heat and Mass Transfer in Capillary Porous Bodies: Oxford Pergamon.
Malan, A.G., September 2002, Investigation into The Continuum Thermodynamic Modelling Of Investment Casting Shell-mould Drying: PhD Theses, University Of Wales, Swansea, Swansea.
Malan, A.G., and Lewis, R.W., 2003, Modelling Coupled Heat and Mass Transfer in Drying Non-hygroscopic Capillary Particulate Materials: Communication in Numerical Methods in Engineering, v. 19, p. 669-677.
Murugesan, K., Seetharamu, K.N., Aswatha Narayana, P.A., Thomas, H.R., and Ferguson, W.J., 2000, Study of Shrinkage Stress for Drying Brick as A Conjugate Problem: International Journal for Numerical Method in Engineering, v. 48, p. 37-53.
Murugesan, K., Suresh, H.N., Seetharamu, K.N., Aswatha Narayana, P.A., and Sundararajan, T., 2001, A Theoretical Model of Brick Drying as A Conjugate Problem: International Journal of Heat and Mass Transfer, v. 44, p. 4075-4086.
Murugesan, K., Thomas, H.R., and Cleall, P.J., 2002, An Investigation of The Influence of Two Stages Drying Condition on Convective Drying of Porous Materials: International Journal of Numerical Methods for Heat and Fluid Flow, v. 12, p. 29-46.
Nijdam, J.J., Langrish, T.A.G., and Keey, R.B., 2000, A High-Temperature Drying Model for Softwood Timber: Chemical Engineering Science, v. 55, p. 3585-3598.
Onsager, L., 1931, Reciprocal Relations in Irreversible Processes: Phys. Rev, v. 37, p. 405-426.
Perre, P., Moser, M., and Martin, M., 1993, Advances in Transport Phenomena During Convective Drying with Superheated Steam and Moist Air: International Journal Heat Mass Transfer, v. 36, p. 2725-2746.
Philip, J.R., and de Vries, D.A., 1957, Moisture Movement in Porous Materials Under Temperature Gradients: Trans. Am. Geophys. Union, v. 38, p. 222-232.
Scherer, G.W., 1990, Theory of Drying: Journal America Ceramic Society, v. 73, p. 3-14.
Sherwood, T.K., 1929, The Drying of Solids-I,II: Ind Eng. Chem, v. 1,10, p. 12-16, 976-80.
Shushang, P., and Keey, R.B., 1994, Modelling The Temperature Profiles Within The Boards During The High Temperature Drying of Pinus Radiata Timber: The Influence of Airflow Reversal: International Journal Heat Mass Transfer, v. 38, p. 189-205.
Spolek, G.A., Plumb, O.A., and Olmstead, B.A., 1985, Heat and Mass Transfer in Wood During Drying: International Journal of Heat Mass Transfer, v. 28, p.

1669-1678.
Stanish M.A., Schajer, G.S., and Ferhan, K., 1986, A Mathematical Model of Drying for Hygroscopic Porous Media: AIChE, v. 32, p. 1301-1311.
Thomas, H.R., and He, Y., 1995, Analysis of Coupled Heat, Moisture and Air Transfer in A Deformable Unsaturated Soil: Geotechnique, v. 45, p. 677-689.
Thomas, H.R., Morgan, K., and Lewis, R.W., 1980, A Fully Non-linear Analysis of Heat and Mass Transfer Problem in Porous Bodies: International Journal for Numerical Methods in Engineering, v. 15, p. 1381-1393.
Whitaker, S., 1977, Simultaneous Heat, Mass and Momentum Transfer in Porous Media; A Theory of Drying: Advances in Heat Transfer, v. 13, p. 119-203.
Whitakers, S., and Chou, W., 1983, Drying Granular Porous Media-Theory and Experiment: Drying Technology 1, v. 1, p. 3-33.
Zhang, Z., 1999, Mechanism and Mathematical Model of Heat and Mass Transfer During Convective Drying of Porous Materials: Heat Transfer_Asian Research, v. 28, p. 337-351.

CHAPTER 3

MATERIAL PROPERTIES AND TRANSPORT PROPERTIES

CHAPTER LAYOUT

In this study of drying porous media, the definition of parameters, such as transport parameters and any dynamic variables that are related to the transport and material properties need to be defined in order to describe the theory and mechanism of the drying process as reviewed in Chapter 2. These will be integrated into the complete coupled derivation that will be set out in Chapter 4. In the first section, the definition and characterization of the basic hygro-properties of porous material, the physical and material properties of solid, liquid water, vapour and gas are given. In the second section the transport properties (via mass, heat and gas) that include capillarity, diffusion mechanisms (conductivity) etc are presented based on the multiphase system. This also includes consideration of both internal and external behaviour.

3.1 Introduction

This chapter contains two main sections which describe the introduction of material and physical properties and the transport properties during the drying process. The definition and characterization of the multiphase porous body is illustrated at the beginning, to give a brief idea about liquid, water and air proportion inside the body. This is followed by the classification of the liquid (saturation) which is an important parameter that defines the porous material category. In this model, the material is defined as a three-phase system comprising liquid, gas and solid (ceramic) particles. Therefore important physical and material properties for each phase are presented based on standard data or data from drying and flow in similar porous networks. These parameters are very important in closing the coupled governing equations as described in the next section and in Chapter 4. In reviewing the literature it became apparent that there are no relevant published data for ceramic shell drying for investment casting. For example, brick or concrete drying has been used extensively as a benchmark for comparing simulations and is therefore well documented (Baroghel-Bouny *et al.*, 1999; Ben Nasrallah, 1988; Ilic and Turner, 1989). There is only limited data on ceramic shell materials and generally this is aimed at end application or quality assurance and does not provide information that is directly applicable for the purpose of drying simulations (Jones, 1995; Jones and Leyland, 1994; Leyland and Jones, 1994).

In the next section, the formulations of transport properties that are relevant to the drying process are given. The derivation of these transport properties is either physically-based (measured experimentally) or based on empirical or probabilistic functions. Some of the dynamic transport relationships such as the saturation curve is taken from well documented literature in the field of soil mechanics (Mualem, 1976; Van Genuchten, 1980) and hygrothermal porous media (Baroghel-Bouny *et al.*, 1999).

3.2 Physical and material properties

The right input of parameters and their range need to be determined when undertaking simulation of the drying process and some of the materials exhibit a dependence on the dependent variables, leading to a solution that is highly nonlinear. Furthermore, the precision and range of some parameters is very important in order to facilitate and ensure an accurate solution. This is very critical especially when dealing with highly nonlinear parameters that may easily influence the convergence process and hence prevent a solution from being achieved. Due to the fact that some of the simulations studies that are carried out feature significant temperature change that reflects nonisothermal drying, therefore some physical properties that highly dependent on temperature cannot be assumed as constant (such as dynamic viscosity of air, liquid, gas or vapour). However other physical properties which are less affected or less dependent on temperature, are assumed to be constant in order to reduce complexity when dealing with the isothermal drying condition.

3.2.1 Porosity and saturation

Porosity (ϕ) is one of the main and fundamental material properties which is used to describe a porous body. This value can be measured experimentally. It can be defined as the ratio of the total void or pore volume (V_{void}) to the total volume of the material (V_{total}). Generally, it will describe how dense the body is and gives a general idea of the fluid and gas portion that may occupy the porous network.

$$\phi = \frac{V_{void}}{V_{total}} \tag{3.1}$$

In the drying of a moist porous body, the interaction of heat and mass transport inside the body will occur effectively in the large pore area. The liquid phase in the pore system will provide the opportunity for evaporation, which initiates vapour diffusion and interaction deep inside the body, leading ultimately to a dry porous system. Related to the porosity term is a saturation value (S_l), it is defined as the volume fraction of void space filled by liquid;

$$S_l = \frac{V_l}{V_{void}} \tag{3.2}$$

Saturation is dimensionless and takes values from 0 (when medium is completely dry) to 1 (when the medium is completely saturated). Saturation can be subdivided further into two contributions;

$$S_l = S_{irr} + S_{fw} \tag{3.3}$$

where S_{fw} is the moisture content of free water and the irreducible moisture content S_{irr} is adsorbed water.

3.2.2 Hygroscopic and nonhygroscopic

In the case of nonhygroscopic material adsorbed water is zero. This assumption is applied to most concrete and brick where the latter is only weakly hygroscopic (Ilic and Turner, 1989; Ben. Nasrallah, and Perre, 1988; Stanish *et al.*, 1986). On the other hand this adsorbed water cannot be ignored in the case hygroscopic materials (such as food, wood and etc). Theoretically, bound water migrates by a diffusion process that is driven by a gradient in the chemical potential of the sorbed water molecules. In the absence of free water (nearly fully dry condition), the gas phase is assumed to be saturated with respect to the local bound water content and temperature. Normally, this bound diffusivity coefficient shows a highly functional dependence on material properties. It is more influenced by high temperature and explicitly relates vapour density to the bound water and it is determined through experimentation and by data correlation (Simpson, 1971). Therefore, in this work the existence of bound water is assumed to be negligible and the structure is assumed to be nonhygroscopic (or just weakly hygroscopic). So, the transport variables that will be explained in the next section just indicate the transport mechanisms which cover zone A as shown in the Figure 3.1 below. This covers the range for which shell drying occurs as successive layers are added, the final moisture content (irreducible moisture) is removed in the final stage of manufacture when the shell is fired at typically 800°C.

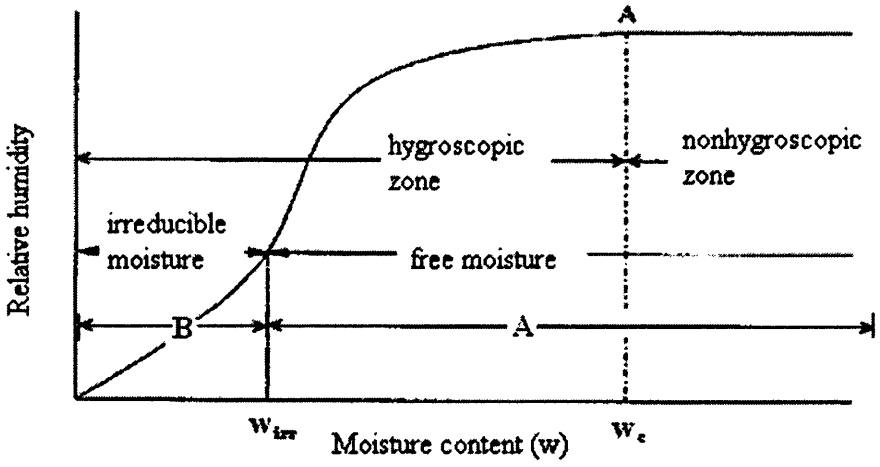

Figure 3.1: Hygroscopic and nonhygroscopic zone (Keey, 1975).

3.2.3 The properties of ceramic porous bodies (based on the concrete or brick ceramic properties)

As mentioned earlier in the introduction, due to the limited data available especially on the dynamic transport properties of the ceramic shell body (such as its saturation curve, its permeabilities) available data on similar materials, such as brick (or concrete) were selected (Baroghel-Bouny *et al.*, 1999; Ilic and Turner, 1989; Ben Nasrallah, and Perre, 1988; Stanish *et al.*, 1986; Zhe Zhang, 1999). In relationship to these critical transport properties, almost all property values such as porosity, intrinsic permeability, etc. presented in the Table 3.1 need to be used and the values need to be consistent with each other in order to maintain the nonlinearity at a realistic level.

Table 3.1: The material properties of brick are taken from the related references (Baroghel-Bouny *et al.*, 1999; Ilic and Turner, 1989; Ben. Nasrallah, and Perre, 1988; Stanish *et al.*, 1986; Zhe Zhang, 1999)

Term	Symbol	Value
Density	ρ_s	2000
Porosity	ϕ	0.12
Intrinsic permeability	K_{intc}	1×10^{-16}

Critical Saturation	S_{cri}	0.3
Irreducible saturation	S_{irr}	0.09
Thermal conductivity	λ_s	1.45
Heat capacity	C_p	920

3.2.4 The properties of liquid water

The typical values of water density, molecular weight, specific heat capacity, thermal conductivity as given in Appendix 1 are considered to be constant and are taken from standard material properties (Rogers and Mayhew, 1976). The value of dynamic liquid viscosity, μ_l is given as below from a fit to standard data given in reference (Kaye and Laby, 1973), over the range 1-100°C. When compared with other properties (as listed above), the dynamic viscosity of liquid water is highly influenced by temperature and its variation is strongly nonlinear when compared with the other properties that have been listed previously.

$$\mu_l = 661.2(T-229)^{-1.562} x\left(1x10^{-3}\right) \pm 0.5\% \tag{3.4}$$

3.2.5 The Properties of gas (vapour and air)

The gas phase, which is denoted by variables with the subscript g in this work, is a mixture of air and water vapour which may be further denoted by the additional subscripts a and v, respectively. The total gas pressure is the sum of partial air and vapour pressure and it is assumed the gas obeys the ideal gas law. Therefore the density of vapour and air are considered to be as below respectively;

$$\rho_v = \frac{M_v P_v}{RT} \tag{3.5}$$

$$\rho_a = \frac{M_a P_a}{RT} \tag{3.6}$$

The density of the gas phase is simply;

$$\rho_g = \rho_a + \rho_v \tag{3.7}$$

The dynamic viscosity of the vapour-air mixture, μ_g (Bird *et al.*, 2002; Thai Hong, 2006) is defined as below;

$$\mu_g = \frac{\mu_v}{1+\Phi_1} + \frac{\mu_a}{1+\Phi_2} \tag{3.8}$$

where;

$$\Phi_1 = \frac{1}{\sqrt{8}}\left(1+\frac{M_v}{M_a}\right)^{-\frac{1}{2}}\left[1+\left(\frac{\mu_v}{\mu_a}\right)^{1/2}\left(\frac{M_a}{M_v}\right)^{1/4}\right]^2$$

$$\Phi_1 = \frac{1}{\sqrt{8}}\left(1+\frac{M_a}{M_v}\right)^{-\frac{1}{2}}\left[1+\left(\frac{\mu_a}{\mu_v}\right)^{1/2}\left(\frac{M_v}{M_a}\right)^{1/4}\right]^2$$

This represents a combination of the dynamic viscosity from both vapour and air. Both of these values will be presented in the next sections below.

3.2.5.1 The properties of dry air

The typical values of molecular weight, the specific heat capacity are given as below are assumed to be a constant and referred to the standard data (Mayhew and Rogers, 1976) and can be found in the Appendix 1. The dynamic viscosity of dry air is again dependent on temperature. According to the study of Maitland and Smith (1972) the following equation gives the best result when compared to the experimental data at constant pressure.

$$\mu_{ga} = 182x10^{-7}\exp\left[0.63404\ln(T) - \frac{45.638}{T} + \frac{380.87}{T^2} - 3.4505\right] \quad \text{Ns/m}^2 \tag{3.9}$$

3.2.5.2 The properties of vapour

Coexisting liquid and vapour are assumed to be in local thermodynamic equilibrium. The pressure of vapour in equilibrium with the pore water is less than that of vapour in equilibrium with free water because of the effects of adsorption and capillarity. To

account for this effect, the vapour pressure is expressed as;

$$P_v = P_{sat}(h) \tag{3.10}$$

Or in terms of density of water vapour is given as;

$$\rho_v = \rho_{sat}(h) \tag{3.11}$$

where P_{sat}, ρ_{sat} and h are the saturated pressure of water vapour, vapour density and relative humidity. The relative humidity may be defined using Kelvin's equation. The relative humidity is the ratio between the actual vapour in the air-vapour mixture, and the saturation vapour pressure at a given temperature. The relative humidity is dimensionless and can take values from 0 to 1. The saturated vapour density is a function of temperature (Rogers and Mayhew, 1976; Reid and Sherwood, 1966) and is given by ;

$$\frac{1}{\rho_{sat}} = 194.4\exp\left\{-0.06374(T-273)+0.1634*10^{-3}(T-273)^2\right\} \tag{3.12}$$

Theoretically in a partially filled closed porous system, the air inside the pore will be in a good equilibrium with the water or water vapour. For the case of the saturated condition or in the existence of free water, this local water vapour is nearly close to 1 and stays in constant equilibrium across the pore section. This local water vapour is particularly different from the water vapour in the boundary layer adjacent to the porous body especially in the case of drying through a convection process. Generally, the drying process is described by having a low relative humidity in the ambient condition, so that a moist body gives out moisture in the process of attaining equilibrium with the surrounding air. However as drying proceeds and moisture continues to be drawn out from the saturated body, the evaporation front will appear inside the body and divide the system into a two regions. During this stage, the vapour transport mechanism starts to play an important role inside the porous body and therefore below a critical value there is a big drop of relative humidity across the body

(Gawin and Schrefler, 1996). Finally this is followed by the stabilization of the water vapour to the ambient condition as the body becomes nearly fully dried.

The molecular weight, the gas constant, the specific heat capacity of vapour and the latent heat of vaporisation are assumed to be a constant and referred to the standard data are (Mayhew and Rogers, 1976; Reid and Sherwood , 1966) and are given in the Appendix 1. These are assumed to be a constant and referred to as standard data. The dynamic viscosity of water vapour is again assumed to be dependent on temperature and is stated below;

$$\mu_v = 125.4x10^{-7} + 3.711(T - 373) \tag{3.13}$$

3.2.6 Effective thermal conductivity

In drying porous material, heat is conducted via liquid, gas and solid as described by Fourier's Law. As heat conduction occurs in all phases in parallel, the heat flux or thermal conductivity contribution must be weighed according to their respective volume fraction. The formulation given below is derived based on the thermal conductivity of the porous matrix together with the thermal conductivity of air and liquid contained in the pores (Thai Hong, 2006). These properties will change as the liquid portion reduces during drying; this is due to the fact that the water conducts a larger amount of heat compared with the other phases.

$$\lambda_{eff} = (1-\phi)\lambda_s + S_l\lambda_l(\phi) + (1-S_l)\lambda_a\phi \tag{3.14}$$

3.2.7 Effective heat capacity

The time–dependent terms in the energy equation (Equation 4.27) represent the storage of latent heat due to the accumulation of vapour and the local capacity for heat comprising the capacity of the ceramic solids, the liquid, the water vapour and dry air inside the porous body. Expressing this heat capacity of ceramic body gives:-

$$H = \left[(1-\phi)\rho_s C_{ps} + \phi S_l \rho_l C_{pl} + \phi S_g \rho_v C_{pv} + \phi S_g \rho_a C_{pa}\right](T - T_r) \qquad (3.15)$$

The specific heat capacity of water, vapour and air in the pores within the ceramic body, are material independent and can be obtained from standard thermodynamic tables (Rogers and Mayhew, 1976) as set out in the Appendix1.

3.3 Transport properties

As explained in the previous section, during the course of drying, transport of heat, mass and gas takes place inside the body as well as at the boundary layer. The transport properties inside the porous domain can be governed at the macroscopic range or microscopic range, and can be varied dependent on the regime of the drying process. In this work drying at the outer surface is governed by the heat and mass transfer coefficient that is determined by the environment for the convective drying process (this boundary mechanism will be explained in Chapter 4).

3.3.1 Transport of mass

Basically, in modelling most ceramic bodies (such as brick, concrete) it is assumed that the body is in the non-saturated condition (or partially filled with water and gaseous phases), (Ilic and Turner, 1989; Ben Nasrallah, and Perre, 1988). Therefore moisture transport in the non-saturated body is presented by the sum of liquid flow and vapour flow. Theoretically in the drying process, moisture transport in the porous material is described by the liquid flow due to the capillary forces, vapour flow due to the bulk gas flow and diffusion mechanism. This is presented as below;

Liquid flow; $$m_l = -(\rho_l v_l) - \dot{\bar{m}}_l \qquad (3.16)$$

Vapour Flow; $$m_v = -(\rho_v v_v + \rho_v v_g) + \dot{\bar{m}}_v \qquad (3.17)$$

The liquid velocity, v_l can be described with Darcy's law. However, now the permeability, k_l and the pressure are functions of the liquid content;

$$v_l = -\frac{k_l(s_l)}{\mu_l}\frac{\partial p(s_l)}{\partial x} = K_l\left(\frac{\partial\left(P_g - P_c - \rho_l g\right)}{\partial x}\right) \tag{3.18}$$

The proportionality constant K_l is termed hydraulic conductivity. Hydraulic potential is the sum of gas pressure, P_g and matrix potential, P_c, gravitational potentials, $\rho_l g$.

The condensation and evaporation terms of vapour flow are given as, $+\dot{m}_l$ and $-\dot{m}_l$. The pressure potential is due to hydrostatic or pneumatic pressure applied to water. The gravitational component of water potential is simply due to difference in depth in the direction of gravity from a reference point. The matrix potential measures the physical forces, such as capillarity, which bind the water to the porous matrix (this will be explained in the next section below). The retention of water is a result of attractive forces between the solid and liquid phases. In a ceramic, for example, these matrix forces enable it to hold water against such forces as gravity, evaporation, etc. This matrix potential is important as a driving force for flow in unsaturated solid ceramic. In many unsaturated systems this relationship between the matrix potential and the saturation value is given in the form of saturation curve (this will be explained under the next section on the saturation curve and capillarity mechanisms).

As described and stated in the above equation, the vapour flow can occur by diffusion and convection of the bulk flow. Vapour migration may take place by molecular diffusion, due to the differences in a partial vapour pressure gradient in a curved surface (in properly organizing this section, therefore the diffusivity term definition will be explained under the next section). Meanwhile vapour transport in the convection term may take place at high mean temperature (viz, near the boiling point of water). Convection transport of vapour can occur in unsaturated porous media because of the total gas pressure differences. These differences may be due to changes in barometric pressure, thermal gradients, velocity at the outer surface, or change of water phase. Any convective movement of gas phase within a porous media will also

move water vapour and may establish concentration gradients and diffusive fluxes in the same or opposite direction to the convective fluxes.

3.3.2 Transport of heat

Heat transfer in a porous moist body is governed by conduction of solid material, vapour diffusion and phase convection A major contribution of the heat transport comes from the conductivity term that is presented by Fourier law. Due to the fact that ceramic porous material is a three phase system that consists of solid liquid and gas, therefore the coefficients of thermal conductivity and heat capacity (as presented in the above section) are based on the proportions of solid liquid and gas phases. This is very important when dealing with the drying of a moist body because their proportions are always changing as drying continues. As for example, in the early stage of drying, the body may have higher saturation, and therefore at this stage the thermal conductivity of a ceramic porous body is more influenced by the water conductivity compared to the other phases. Furthermore, the water phase shows the highest value in conductivity compared to the components. As given below the transport of heat by conduction through the porous medium is stated as;

$$q_c = -\lambda_{eff}(\nabla T) \tag{3.19}$$

Heat transfer in a capillary porous body is no longer confined to the transport properties of conduction; other factors also need to be included. During drying heat transport plays an important role in initiating the moisture flow from the moist body. Heat is consumed in capillary porous materials in the vaporisation of water. Consequently, when moisture transfer takes place in the form of vapour the component of latent heat captured in the vaporisation process is also transferred. In order to evaporate a certain amount inside the pores the latent heat of evaporation must be supplied, which is relatively large in comparison with other terms in the energy balance. Therefore, latent heat is very important especially when drying at higher temperature because it contributes to the water loss significantly (Gawin, 1996). Basically, the transfer of vapour is due to the diffusion and bulk flow

contribution, therefore, this latent heat contribution can be represented by;

$$q_v = (\rho_v v_v + \rho_v v_g)L \tag{3.20}$$

Furthermore, in some capillary porous materials, where the permeability is high, sensible heat may be transferred by the bulk flow of liquid and vapour. In other words convection of the flow phases driven by the gas and capillary action. This effect is very important in drying and widely introduced in models of drying for porous media (Liu *et al.*, 2005; Thai Hong, 2006; Harun, *et al.*, April 2007). Previously works have excluded this contribution due to the assumption that this is very small (Kallel *et al.*, 1993; Mauri Fortes and Okos, 1981)

$$q_{conv} = (C_{pl}\rho_l v_l + C_{pv}\rho_v v_v + C_{pv}\rho_v v_g + C_{pa}\rho_a v_g)(T - T_r) \tag{3.21}$$

3.3.3 Transport of gas

The total mass flux that is removed from the body can include a contribution from the gas phase (Luikov, 1975; Whitaker, 1997). As stated previously, the gas phase is modelled as an ideal gas that is composed of dry air and water vapour, which are considered as two miscible species. So therefore, the gas transport equation is governed by the gas bulk flow and the contribution of the vapour diffusion to the gas medium. As mentioned earlier the porous medium that is dealt with in this work is an unsaturated porous medium, where the pores contain a moisture and gas portion dependent on the properties of the material itself. In a porous medium, the gas phase starts to change inside the body when there is a change in the water phase in the pore section. The vapour diffusion mechanism effectively starts to occur when the porous domain exceeds the percolation threshold. At this time the vapour diffusion mechanism plays an important role in transferring moisture to the air as described in many drying sources (Keey, 1975; Scherer, 1990; Zhe Zhang, 1999). Meanwhile the air bulk flow is governed by the Darcy's law as determined by the gas permeability value (that will be explained in the next section below).

$$q_g = (\rho_g V_g) + \dot{m} \tag{3.22}$$

3.3.4 Constitutive equations of the coupled heat, mass and gas transport

All the transport variables that represent the heat, mass and gas transport properties are governed by the constitutive equations that describe the flow mechanism such as capillarity and diffusion. Most derivations of the diffusivity or flow variables show that these parameters are always a function of material properties and sometimes depend on the process variables, such as temperature, saturation etc. In these drying models, all constitutive transport derivations and also other dynamic state variables (i.e. saturation curve) are expressed as a function of three working variables, pore water pressure, temperature and gas pressure and this will be presented and explained further in Chapter 4.

3.3.4.1 Capillary mechanism

It has been recognized that the inclusion of the capillary effect in drying of nonhygroscopic porous media is essential since it distinguishes between transport when there is a high water content (where the surface of the porous matrix is covered with a continuous layer of free water) and transport under a regime of lower water content. Generally, mass transport in the saturated condition is governed by capillary action which may be described by a high permeability at the beginning of the process. This capillary action captures the condition of free water movement within the pore network and the reduction of this value indicates the starting of vapour diffusion in the critical stage.

Capillary pressure or potential is governed by the difference between the gas pressure and liquid pore pressure across the pore section. This also needs to take into consideration the surface energy and wetting contact angle. This is given in the Equation below.

$$P_c = P_g - P_l = \frac{2\sigma \cos\theta}{r} = \rho_l g h \tag{3.23}$$

and r is the radius of the capillary tube and θ is the contact angle between the water and solid.

Capillary flow is due to the difference between the relative attraction of the molecules of the liquid for each other and for those of the solid. As the radius becomes very small, capillary rise increases significantly. Capillarity is the reason, for example, the ceramic tissue does not completely drain by gravity. In a porous solid ceramic, the liquid will be attracted or held more tightly when there is less of it, i.e., at lower concentrations. Conversely, the liquid will be held less tightly when there is more of it. Due to the differences in capillary attraction, flow of liquid can occur from locations in the solid having more water to locations of having less water. This is referred to as unsaturated flow and is extremely important in drying of porous system such as a ceramic (or brick) body

As indicated previously by other researchers, the capillary curve can be deduced from experiment and commonly, this is expressed in terms of a water retention curve (Sung *et al.*, 2006). This is represented by the matrix potential and amount of water retained, related to the size of pore spaces which is highly dependent on the shape and angularity of individual pores. Hence it is strongly influenced by the porous structure (Tuller and Or, 2005). Practically, the experiment involves several procedures that have been developed particularly for unsaturated soil systems. However, this kind of method and measurement is now more widely used in various fields, other than soils. This will be covered under the next section on the water retention curve.

3.3.4.2 Water retention curve (water capillary curve)

There exists a non-linear relationship between the porous body moisture content and matric potential. This relationship is usually presented in the form of a water retention curve. Theoretically, the shape of the curve is different if the water content and potential data are generated by drying or wetting. When drying, the volumetric water content is larger for any value of matric potential than when wetting and this phenomenon is called hysteresis. This is shown as in Figure 3.3 below.

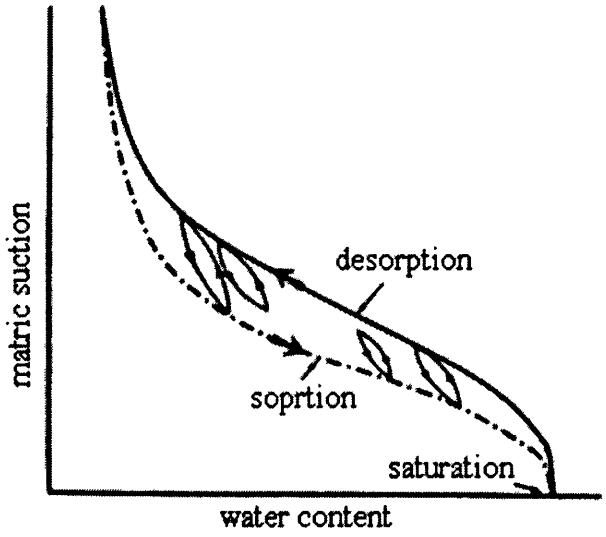

Figure 3.2: Hysteresis of drying and wetting branches of a soil or cementatious material characteristics curve (Baroghel-Bouny *et al.*, 1999).

Numerous empirical equations have been proposed to simulate the water retention curve. Among the earliest is an equation proposed by Brooks and Corey (1964), it is in the form of a power-law relationship. Another effective and commonly used parametric model for relating water content or effective saturation to the matric potential was proposed by Van Genucthen (1980). This model is also widely used in the application of drying of the nonhygroscopic cementitious materials (Baroghel-Bouny *et al.*, 1999; Gawin, 1996) and also hygroscopic porous systems, such as foodstuff (Weerts *et al.*, 2005). The Van Genuchten relationship can be written as;

$$S_l = \left(\frac{1}{1+(\alpha\varphi(T))^n} \right)^m \tag{3.24}$$

where ; $S_l = \dfrac{\theta - \theta_r}{\theta_{sat} - \theta_r}$

φ = suction

α = the air-entry value

θ = actual water content

θ_r = residual water content

θ_{sat} = saturated water content

and the parameters α, n and m are three parameters that define the shape of the θ(φ) curve. The degree of saturation with liquid water S_l, considering together hygroscopic and capillary water (if the latter is contained in the pores) is an experimentally determined function of capillary pressure (matric potential) *Pc* and the temperature T as given below and will be explained under the next section.

$$S_l = S_l(P_c, T) \tag{3.25}$$

A good fit of the capillary curve with experimental work on the water vapour desorption isotherm (in an isothermal drying process at relative humidity 50%) can be obtained through Equation 3.24. This has been shown for example by Baroghel *et al.* (1999), where the best fit of parameters α, *n* and *m* showed a good agreement with the plotted experimental water vapour desorption characteristic for the case of cement pastes and concrete. Due to the fact that, there is not enough information or not many works that are concerned with obtaining the saturation curve (especially in the case of drying) for the ceramic shell and brick, the available data from similar groups of materials (ceramics), was used in this work and their parameter values for the saturation curve are given in Appendix 1 (Section A1.5). In this work the best fit of a desorption saturation curve for concrete was selected, due to the fact that this material shows the nearest characteristic to ceramic brick and shell possibly drying

3.3.4.3 Effect of temperature on the capillarity

Due to the fact that this work also deals with non isothermal drying (for the purpose of validation), it is also appropriate to include the effect of temperature on capillarity. Grant and Salehzadeh (1996) explored the extent to which capillarity is due to temperature-induced changes in the contact angle. The temperature effect on the capillarity pressure can be expressed through the relationship as below.

$$P_c = \frac{P_c(T^r)}{\sigma(T^r)}\sigma(T) \tag{3.26}$$

where T^r is a reference temperature and σ is the surface tension. The temperature dependence of σ has been obtained from a semi-empirical correlation based on data from Grant and Salehzadeh (1996). In their recent paper, Grant and Salehzadeh developed a theory that connected assessable physical quantities like P_c with theory describing surface properties of the solid phase. In their derivation they partitioned the temperature effect of σ and γ on the capillary pressure-saturation relationship by comparison with some experimental works. This derivation can be considered as a thermodynamic extension of the mechanistic Philip and de Vries (1957) model.

To describe this relationship, they introduced a theory to allow the formulation of the wetting coefficient as a function of temperature based on the thermodynamics of interfacial phenomena. Since the surface tension of water decreases with increasing temperature and vanishes at the critical point (T= 647.4 K), the simplest possible form of empirical relationship between σ and T is a linear fit, which describes the temperature effect and is given by:

$$\sigma = a + bT \tag{3.27}$$

The estimates for the two parameters are; a: 0.11766±0.00045 $Nm^{-1}K^{-1}$ and b = -0.0001533±0.0000015 $Nm^{-1}K^{-1}$. Therefore

$$P_c = P_c^0\left(\frac{a+bT}{a+bT_r}\right) \tag{3.28}$$

and T is an arbitrary temperature and T_r is a reference temperature. Combination of Equation 3.28 with the Van Genuchten derivation in Equation 3.24 yields:

$$S_l = S_{irr} + \left(\frac{S_{sat} - S_{irr}}{\left(1+(\alpha P_c(T))^n\right)^m}\right) \tag{3.29}$$

3.3.4.4 Diffusion

In the domain of liquid migration by capillarity, the vapour pressure is equal to saturated vapour pressure and so the gradient of vapour is negligible. Therefore, the effective diffusivity has no influence upon drying during this period. On the other hand in the hygroscopic domain (when the liquid phase becomes discontinuous and a curved meniscus is formed), the value of vapour diffusivity coefficient directly controls the migration of moisture especially in the later stage. Thus as capillary action falls away and air starts to diffuse into the pore this signals the starting point for vapour diffusion which also contributes to the loss of water.

In many cases of the drying of a porous body, vapour moves together with non-condensible gas (air) due to the pressure difference (hence density difference) in the moist porous media. In this work, some combination of the diffusive motion of vapour with the motion of gaseous mixture that have been proposed in by Liu *et. al* (2005) and implemented also in other drying studies (Zhe Zhang, 1999) was chosen. Following this approach, the vapour diffusion term that has been defined in the vapour transport flow (in Equation 3.17) can be written as below. This diffusion term is presented in the form of the Fick's law.

$$q_v = \rho_v V_v = (\rho_v)\frac{-D_{atm} v \alpha \theta_a \nabla \rho_v}{\rho_v} \tag{3.30}$$

where $D_{atm}, v, \alpha, \theta_a$ are the molecular diffusivity of water vapour through dry air, mass factor, tortuosity factor and volumetric air term respectively. The available area for vapour flow is assumed to be equal to the volumetric air content, θ_a or the part of the pores which are not filled with liquid. In a ceramic, the void structure presents a tortuous path for gas flow, which is taken into consideration by an empirical attenuation factor. The tortuosity factor was set to a value of 0.5 (Baggio *et al.*, 1997; Stanish *et al.*, 1986) in both the vertical and horizontal directions, assuming that the pathway is similar for diffusion horizontally and vertically in the ceramic structure. In this work, the expression for water vapour diffusion in air as given by Stanish *et. al* (1986) is used;

$$D_{atm} = 2.20 * 10^{-5} \left(\frac{101325}{P_a + P_v} \right) \left(\frac{T}{273.15} \right)^{1.75} \tag{3.31}$$

A mass flow factor is also introduced to allow for the mass flow of vapour arising from the difference in boundary conditions governing the air and vapour components of the diffusing system. It is calculated from the expression developed by Partington (1949):

$$\nu = \frac{P_g}{P_g - P_v} \tag{3.32}$$

3.3.4.5 Permeabilities

In defining the capillarity mechanism and gas bulk flow using the Darcy's law, both these actions that are influenced by the saturation value are defined by the permeability parameters. The permeability of a material is simply defined as its openness to the transmission of fluid. Permeability is an important property which determines the rate of flow of phases in the porous structure during drying. The intrinsic permeability characterizes the aptitude of a single fluid to migrate within the porous medium. In the case of drying where two fluid phases exist together, this parameter is used for the calculation of the relative permeability for each phase. These parameters that are functions of relative saturation determine the resistance to migration of each phase (liquid and gas) with regard to those where the porous medium is fully saturated. Both have different significant influence where the gas relative permeability is effective when drying approaches the dry medium condition. Theoretically, the permeability in porous material depends on the porosity and also material properties itself (either very hygroscopic or weakly hygroscopic). The function is usually empirically determined and highly dependent on the saturation or saturation curve (Van Genuchten, 1980). Therefore in this work, the same corresponding parameters that have been used in the above saturation curve are chosen. In this selected work (Baroghel-Bouny *et al.*, 1999), both the permeabilities of water and gas were approached using Mualem's model. These formulations are given here as below.

$$k_l(S_l) = \sqrt{S_l}\left(1-\left(1-S_l^{1/m}\right)^m\right)^2, \qquad S_l > S_{irr} \tag{3.33}$$

$$k_l(S_l) = 0, \qquad S_l < S_{irr} \tag{3.34}$$

$$k_g(S_l) = \sqrt{1-S_l}\left(1-S_l^{1/m}\right)^{2m}, \qquad S_l < S_{cri(g)}(0.3) \tag{3.35}$$

$$k_g(S_l) = 0, \qquad S_l > S_{cri(g)}(0.3) \tag{3.36}$$

where $S_{cri(g)}$ is a critical saturation for the gas permeability where the gas porous body starts to form the wet patched area (Zhe Zhang, 1999) and S_{irr} is a irreducible saturation and is given in the range of (0.09-0.1) (Ben Nasrallah and Perre, 1988; Zhe Zhang, 1999).

In the present work an assumption is made that above this value of S_{irr}, both Kelvin's and Darcy's laws can be implemented. Further, it is assumed that this value is small enough for brick, so that for most computing work this number is close to zero and when $S_l = S_{irr}$ the medium is assumed to be dry. This assumption has been reported in many simulation and theoretical works either for brick or wood based material (Ben Nasrallah , 1988; Ilic and Turner, 1989; Nidjam *et al.*, 2000).

Based on the above permeability values, the hydraulic conductivity tensor for water flow, K_l and gas flow, K_g are given as below;

$$K_l(S_l) = \frac{K_{intc}(k_l)}{\mu_l} \tag{3.37}$$

$$K_g(S_g) = \frac{K_{intc}(k_g)}{\mu_g} \tag{3.38}$$

where K_{intc} is the intrinsic permeability and μ_l and μ_g are the dynamic viscosity of water and gas respectively.

3.4 Closure

The physical and material properties of the porous body, liquid water, air, vapour and gas phases are presented in this Chapter as required for the derivations in Chapter 4. Most of the physical and material properties are based on the materials that only approximate ceramics. The important transport properties of drying porous media via heat, mass and gas are governed by flow and diffusion mechanisms. These flow and diffusion mechanisms are derived based on the dynamic transport relationship for every phase during the drying process. Some of the constitutive equations of dynamic transport are given in the open literature for porous unsaturated media are implemented in this work. The values given are typical at a reference temperature of 20°C (293 K) and a reference gas pressure of 101320 Pa (1 atm).

REFERENCES

Baggio, P., Bonacina, C., and Schrefler, B.A., 1997, Some Considerations on Modelling Heat and Mass Transfer in Porous Media: Transport in Porous Media, v. 28, p. 233-251.

Baroghel-Bouny, V., Mainguy, M., Lassabatere, T., and Coussy, O., 1999, Characterization and Identification of Equilibrium and Transfer Moisture Properties for Ordinary and High-performance Cementitious Materials: Cement and Concrete Research, v. 29, p. 1225-1238.

Ben Nasrallah, S., and Perre, P., 1988, Detailed Study of A Model of Heat and Mass Transfer During Convective Drying of Porous Media: International Journal Heat Mass Transfer, v. 31, p. 957-967.

Bird, R.B., Steward, W.E., and Lighfoot, E.N., 2002, Transport Phenomena: New York, J. Wiley.

Brooks, R.H, and Corey, A.T.C., 1964, Hydraulic Properties of Porous Medium: Hydrology Paper 3: Colo. State Univ. Fort Collin.

Gawin, D., and Schrefler, B.A., 1996, Thermo-hydro-mechanical Analysis of Partially Saturated Porous Materials: Engineering Computations, v. 13, p. 113-143.

Grant, S.A, and Salehzadeh, H., 1996, Calculation of Temperature Effects on Wetting Coefficients of Porous Solids and Their Capillary Functions: Water Resources Research Journal, p. 261-270.

Ilic, M., and Turner, I.W., 1989, Convective Drying of A Consolidated Slab of Wet Porous Material: International Journal Heat Mass Transfer, v. 32, p. 2351-2362.

Jones, S., 1995, The Use of Conductivity as A Means Of Assessing The Extent Of Wet Back in An Investment Mould, England, Material and Metallurgy Dept., The University of Birmingham.

Jones, S., and Leyland, S., 1994, Investigation into the Drying Behaviour of Water Based Slurries: I.C.I 42nd Annual Technical Meeting.

Kallel, F., Galanis N., Perrin, B., and Javales, R., 1993, Effects of Moisture on Temperature During Drying of Consolidated Porous Materials: Transaction of ASME, v. 32, p. 1301-1311.

Kaye, G.W.C., and Laby T.M., 1973, Tables of Physical and Chemical Constants: Harlow, Longman.

Keey, R.B., 1975, Drying Principles and Practice: Great Britain, Pergamon Press.

Leyland, S., and Jones, S., 1994, The Effect of Drying Conditions Upon The Wax/Ceramic Interface Temperature: In Internal Report for Rolls Royce plc and School of Metallurgy and Materials.

Liu, B.C., Lui, W., and Peng, S.W., 2005, Study of Heat and Moisture Transfer in Soil with A Dry Surface Layer: International Journal of Heat and Mass Transfer, v. 48, p. 4579-4589.

Luikov, A.V., 1975, Heat and Mass Transfer in Capillary Porous Bodies: Oxford Pergamon.

Maitland, G.C., and Smith, E.B., 1972, Critical Reassessment of Viscosities of 11 Common Gases: Journal of Chemical of Engineering Data, v. 17.

Mauri, F., and Okos, M.R., 1981, Heat and Mass Transfer in Hygroscopic Capillary Extruded Products: AIChE, v. 27, p. 255-262.

Mayhew, Y.R, and Rogers, G.F.C., 1976, Thermodynamic and Transport Properties of Fluids: Oxford, Blackwell.

Mualem, Y., 1976, New Model for Predicting Hydraulic Conductivity of Unsaturated

Porous-Media: Water Resources Research Journal, v. 12, p. 513-522.
Nidjam, J.J., Langrish, T.A.G., and Keey, R.B., 2000, A High-Temperature Drying Model for Softwood Timber: Chemical Engineering Science, v. 55, p. 3585-3598.
Partington, J.R., 1949, Advanced Treatise on Physical Chemistry, v. 1: London, Longman, 912 p.
Reid, R.C., and Sherwood, T.K., 1966, The Properties of Gases and Liquids: New York, McGraw-Hill.
Scherer, G.W., 1990, Theory of Drying: Journal of American Ceramic Society, v. 73(1), p. 3-14.
Simpson, W.T., 1971, Equilibrium Moisture Content Prediction for Wood: for Proceeding Journal, v. 21, p. 48.
Stanish, M.A., Schajer, G.S., and Ferhan, K., 1986, A Mathematical Model of Drying for Hygroscopic Porous Media: AIChE, v. 32, p. 1301-1311.
Sung, S.G., Lee, I., Cho, G., and Reddi, L.N., 2006: Geothechnique, v. 55, p. 569-573.
Thai Hong, V., 2006, Influence of Pore Size Distribution on Drying Behaviour of Porous Media by A Continuous Model: Doctorate thesis Universitat, Magdeburg.
Tuller, M., and Or, D., 2005, Water Retention and Characteristic Curve: *in* E. Ltd. ed., Moscow, University of Idaho.
Van Genuchten, M.T., 1980, A Closed-form Equation for Predicting The Hydraulic Conductivity of An Saturated Soils: Soil Science Soc. Am Journal, v. 44, p. 892-898.
Weerts, A.H., Martin, D.R., Lian, G., and Melrose, J.R., 2005, Modelling The Hydration of Foodstuff: Simulation Modelling Practice and Theory, v. 13, p. 119-128.
Whitaker, S., 1997, A Theory of Drying Advances in Heat Transfer, v. 13, 199-203 p.
Harun, Z., Gethin, D.T., Lewis, R.W., and Ferguson, W.J., April 2007, Drying of A Multilayer Ceramic Shell Body: The Fifteenth UK Conference of The Association of Computational Mechanics in Engineering.
Zhe Zhang, 1999, Mechanism and Mathematical Model of Heat and Mass Transfer During Convective Drying of Porous Materials: Heat Transfer Asian Research, v. 28, p. 337-351.

CHAPTER 4

MATHEMATICAL FORMULATIONS AND THEORETICAL MODELLING

CHAPTER LAYOUT

This chapter discusses the development of a two-dimensional mathematical model, describing the heat, mass and gas transfer during the drying of brick and ceramic shell multilayer bodies. The mathematical model that is used in this drying modelling and simulating process was extracted from the comprehensive model by Whitaker and incorporates Fick's law for the vapour transport mechanism. Three primary variables were considered during the model development: pore water pressure, temperature and gas pressure. The heat was transported by conduction; convection due to the fluid phase movement and the latent heat of evaporation. Water phases were transported by capillarity, convection of the bulk flow and diffusion due to the partial vapour pressure. Gas phase (vapour and air) was transported via air bulk flow due to the gas pressure gradient and vapour diffusion flow. By employing a constitutive derivative in expressing the related effective coefficients (diffusion and saturation coefficients) and incorporating the thermodynamic concept, leads to the integrating of variables into a coupled solution.

4.1 Introduction

The analysis of heat and mass transfer in drying a ceramic porous system is very important because most ceramic properties change with temperature and moisture content. There have been various models available for porous material for prediction of temperature and moisture variation during drying. Most of the previous models neglect the gas transport (which is very important in the drying case study) or the model is presented in a one dimensional framework. So in this work, a comprehensive model which includes heat, mass and gas transport was selected to model the drying of a porous ceramic structure.

A ceramic porous material can be represented as a three phase (gas, liquid and solid) system. In this study, the liquid phase is considered to be pure water and in equilibrium with the gas phase that is a mixture of vapour and air. Both the liquid and gas phases are assumed to flow through a rigid porous matrix, hence the model reduces to a two-phase flow system. During the drying of ceramic, the internal conditions (capillarity, moisture and vapour content, gas and water pressure and temperature which are all linked together in terms of thermodynamics) will change according to the external conditions that prevail together with the initial conditions that have been prescribed. Also, the transport coefficients that were previously defined in Chapter 3 depend on the state of the ceramic body and are often also a function of the field variables, such as water potential, temperature, gas pressure etc. This illustrates the fact that the system is a highly complex and highly nonlinear problem. So, by considering, the interaction of heat, mass and gas transport in the porous domain, the fully coupled model is derived based on two-dimensional temporal variations in temperature, pore water pressure, and gas pressure. The extension to three dimensions follows a similar path and is relatively straight forward to derive.

4.2 Background of the proposed model in this work

The analysis of drying porous media either through experimental work, theoretical or analytical research that has focused on the heat and mass transfer (two equation

approach) or heat, mass and and gas transfer (three equation approach) has been reviewed and discussed in detail previously in Chapter 2. So therefore, this section will be focussed on the elaboration of the selected model, experimental and theoretical works that has led to the development of the fully coupled model in this work.

Various models have been developed to describe the drying of a porous structure. At the end of the 1980s, Whitaker (1977) proposed one of the most comprehensive models to describe drying in a porous structure. By using a volume average method, Whitaker presented a set of equations to describe the simultaneous heat, mass and momentum transfer in porous media within a continuum framework. Based on the conservation laws, the model proposed by Whitaker, is an important milestone in the development of drying theory. It incorporates all mechanisms for heat and mass transfer: liquid flow due to capillarity forces, vapour and gas flow due to convection and diffusion, internal evaporation of moisture and heat transfer by convection, diffusion and conduction. By using the volume averaging method, the macroscopic differential equations were defined in terms of average field quantities. This theory of Whitaker was further developed and applied in the drying analysis of various porous media, for example in the drying of sand (Whitaker and Chou, 1983), brick (Ben Nasrallah and Perre, 1988), cellular material (Crapiste, 1988), wood (Spolek and Plumb, 1980) and etc. In these works, the model is usually quite successfully matched against experimental data. Some of the important advances made in developing Whitaker's theory are selected for discussion below.

One of the most significant advances in developing Whitaker's theory as well as in modelling the drying of porous media comes from the work of Ben Nasrallah *et al.* (1988). They proposed a model of heat and mass transfer of porous media under convective drying within a one dimensional framework for two different porous media (clay brick and softwood). The model comprised a set of comprehensive equations, with three variables (temperature, pore water and gas pressure), with the gas pressure incorporating a mixture of vapour and dry air. The theoretical equations were obtained by averaging the classical fluid mechanics, diffusion and transfer equations over a control volume and the system of equations was solved by a finite differences method based on the notation of a control domain described by Patankar

(1980). The evolution of variables as well as the overall drying kinetics was calculated for two different porous media in order to study the sensitivity of the model to the internal parameters and conditions at the interface as well as the effect of some simplifications within the model. A detailed study and some comparisons on the model reduction were discussed and it was concluded that it seems to give the best approximation for drying modelling. This is the reason why this model was selected to derive the basic governing equations in this work.

Stanish *et al.* (1986) presents one of the most comprehensive of the one dimensional mathematical models for simultaneous heat and moisture transfer in hygroscopic and nonhygroscopic porous material. The basis of the model was a set of fundamental transport equations (considering moisture water, bound and free water, water vapour and air content), coupled with a thermodynamic equilibrium equation. Different transport mechanisms were established for the separate phases. The heat transfer occurred via conduction, latent heat movement and convection. The mass transfer of the gaseous air and vapour was via combined diffusion and bulk (hydrodynamic) flow. The bound water only by diffusion and the free water only by the bulk flow. Some experimental works were set up for testing the model performance and verification of its predictions in a one dimensional scale, and the same experimental result was also chosen for the validation through a study of brick drying in this work.

It is clear either from the previous literature review in Chapter 2 and the previous models that are presented in the above paragraph that they have inherent limitations; either they were one-dimensional, the coupled problem neglected the gas transport mechanism, or gross simplifications were made concerning the transfer mechanisms to ambient conditions. In fact, none of them proposed an approach for modelling the drying of a multilayer system. The most commonly used approach is to treat the multilayer as a single layer or homogenous layer. However the drying of a multilayer is different from the drying of a single layer. For example, a multilayer shell may contain several layers each having a different moisture and gas content. Traditionally, the multilayer shell making mould involves the dipping and drying of slurry layers for a certain time. Due to the fact that multilayer shell systems are built with similar materials, thus it may be assumed that there is no discontinuity between each layer and there is no interface to generate a contact resistance. This is due to the high

absorption of water at the dipping part of the layering cycle leading to good wetting as layers are built up. This has been demonstrated by extensive works (Jones, 1995; Jones and Leyland, 1994) on assessing fluid uptake as the dry shell is immersed in slurry within the fabrication cycle. Eliminating consideration of this interface resistance simplifies the mathematical formulation and simulation of this layering influence (Mendes, 2005).

In this work, a general approach as mentioned above was followed during the model development, which allowed a comprehensive description of the heat and mass transfer along with the gas transport phenomena during the ceramic shell drying that is part of the build-up sequence. Other factors that need to be considered when developing simultaneous heat, mass and gas transport equations are constitutive equations describing the specific behaviour of the considered material and phases that have been given in Chapter 3 are also included.

4.3 Model development: Theoretical and Mathematical formulation

In the present investigation, the complete theoretical formulation of the drying model proposed by Ben Nasrallah (1988) is presented. The model was developed and extended to two spatial dimensions (from which further generalisation into the three dimensional domain is relatively straight forward) and is expressed in terms of the three interdependent variables (moisture potential, temperature and gas pressure as working variables) in the form of partial differential equations, reflecting the conservation of mass, heat and gas transport. The transport properties which govern the thermophysical relationships in porous and ceramic media, drawn from several related references, were selected and used in these derivations. The key assumptions applied when developing this model are as follows;

- Solid, liquid and gaseous phases are considered, and these three phases are always in local thermodynamic equilibrium.
- The fluid is present in liquid and vapour phases.

- The movement of moisture in the porous skeleton is sufficiently slow so that in practice the temperatures of the liquid and vapour phases in the body are equal at coincident points.
- The gas phase located in the voids is composed of an air and vapour mixture, and the components follow the Ideal Gas Law.
- Dimensional changes which occur within the material, due to a temperature or moisture content change, are comparatively small and will be ignored.
- In this work, the brick and ceramic shell body are nonhygroscopic materials, so in this case also the sorption isotherm effect from bound water that is present below irreducible saturation is negligible. Bound water plays an important role in drying hygroscopic material such as wood, food and etc when the water contained within the cell structure is removed in the final stages of the drying process.
- Below irreducible saturation, the capillary mechanism becomes inoperative and the mechanism of water loss is only from vapour diffusion transport described through Kelvin's equilibrium equation.
- No contact resistance exists between layers in drying multilayer structures.
- The matrix is rigid and homogenous and isotropic.
- Darcy's law holds for the gas and liquid phases.
- Gravity is important for liquid, but not for the gas phase.
- Stresses developed through hygrothermal action are excluded from the scope of this study.

4.3.1 Derivation of mass transfer

An essential difference between solid and porous material is the potential for a substantial amount of water to be present in the material structure. Additionally, the water can be in the form of free (liquid), water partially filling the pore, vapour and bound water. In this work the ceramic body was considered to have the same properties as a nonhygroscopic brick. Based on the above consideration, moisture exists in two states i.e. liquid water and water vapour. The volumetric water content, θ, is defined as the sum of these two phases.

$$\theta = \theta_l + \theta_v \tag{4.1}$$

where θ_l is the volumetric liquid content and θ_v is the volumetric vapour content.

To obtain the drying conservation law of mass flow, Equation 4.1 can be utilised to combine the laws of conservation of mass for its component phases, namely liquid and vapour during drying. Firstly the liquid phase is considered. The mass conservation law dictates that the time derivative of the liquid content is equal to the gradient of the liquid flux as given in Equation 3.16. Mathematically this can be expressed as:

$$\frac{\partial \phi S_l \rho_l}{\partial t} = \frac{\partial \theta_l \rho_l}{\partial t} = -\frac{\partial \rho_l v_l}{\partial x} - \dot{m} \tag{4.2}$$

where ϕ, ρ_l, v_l, S_l, $\left(-\dot{m}\right)$ are the porosity, liquid density, liquid water velocity, liquid saturation and evaporation term (the evaporated water in units of time and volume) respectively.

As illustrated in Chapter 3, vapour flow in a porous medium under drying conditions is due to the vapour diffusion under the influence of a partial vapour pressure and as part of the bulk flow of gas. Therefore, applying the mass conservation law to the vapour flow in Equation (3.17) gives;

$$\frac{\partial \phi S_g \rho_v}{\partial t} = \frac{\partial \theta_v \rho_v}{\partial t} = -\frac{\rho_v v_v}{\partial x} - \frac{\partial \rho_v v_g}{\partial x} + \dot{m} \tag{4.3}$$

where v_l and v_g are the velocity of vapour and pore air , ρ_v is density of water vapour and $\left(+\dot{m}\right)$ is the condensation term (the condensation of water in units of time and volume) respectively.

The mass balance of the liquid water and water vapour, summed together to eliminate

the occurrence of sources and sinks being equal zero (since the moisture is neither lost nor gained by the material). This forms the mass balance equation for the total amount of water inside the pores;

$$\frac{\partial \phi S_l \rho_l}{\partial t} + \frac{\partial (\phi S_g \rho_v)}{\partial t} = -\nabla(\rho_l v_l) - \nabla(\rho_v v_v) - \nabla(\rho_v v_g) \tag{4.4}$$

Derivation of the left hand side term (the temporal change of water inside a control volume) based on Philip and de Vries approach uses the vapour density derivation (Liu *et al.*, 2005). The vapour density is given by

$$\rho_v = \rho_{sat} h \tag{4.5}$$

where, ρ_{sat} is the density of the saturated vapour and h is the relative humidity.

The relative humidity as given by Kelvin's law states that;

$$h = \exp\left(\frac{P_l - P_g}{\rho_l R_v T}\right) \tag{4.6}$$

where P_l and P_g are the pore water pressure and total gas pressure respectively, and R_v is the specific gas constant for water vapour (461.5 J/kg K).

The saturated vapour density is a function of temperature (Rogers and Mayhew, 1976)

$$\frac{1}{\rho_{sat}} = 194.4 \exp\left\{-0.06374(T - 273) + 0.1634 * 10^{-3}(T - 273)^2\right\} \tag{4.7}$$

Therefore,

$$\frac{\partial \rho_{sat}}{\partial t} = \frac{\partial \rho_{sat}}{\partial T}\frac{\partial T}{\partial t} \tag{4.8}$$

$$\frac{\partial \rho_{sat}}{\partial t} = \beta \frac{\partial T}{\partial t} \tag{4.9}$$

where,

$$\beta = \frac{\partial \rho_{sat}}{\partial T}$$

According to chain rule,

$$\frac{\partial h}{\partial t} = \frac{\partial h}{\partial P_l}\nabla P_l + \frac{\partial h}{\partial T}\nabla T + \frac{\partial h}{\partial P_g}\nabla P_g \tag{4.10}$$

$$\frac{\partial S_l}{\partial t} = \frac{\partial S_l}{\partial P_l}\nabla P_l + \frac{\partial S_l}{\partial T}\nabla T + \frac{\partial S_l}{\partial P_g}\nabla P_g \tag{4.11}$$

$$\frac{\partial \rho_l}{\partial t} = \frac{\partial \rho_l}{\partial P_l}\nabla P_l + \frac{\partial \rho_l}{\partial T}\nabla T + \frac{\partial \rho_l}{\partial P_g}\nabla P_g \tag{4.12}$$

Note also,

$$\frac{\partial S_l}{\partial t} = -\frac{\partial S_g}{\partial t} \quad \text{where } (S_g + S_l = 1) \tag{4.13}$$

Expanding the left hand side of Equation 4.4 and applying Equation 4.5 gives,

$$\begin{aligned} &\phi \rho_l \frac{\partial S_l}{\partial t} + \phi S_l \frac{\partial \rho_l}{\partial t} - \rho_{sat} h \phi \frac{\partial S_l}{\partial t} + \rho_{sat} \phi S_g \frac{\partial h}{\partial t} + h \phi S_g \frac{\partial \rho_{sat}}{\partial t} \\ &= -\nabla(\rho_l v_l) - \nabla(\rho_v v_v) - \nabla(\rho_v v_g) \end{aligned} \tag{4.14}$$

Replacing equations (4.9), (4.10), (4.11) and (4.12) for $\frac{\partial \rho_{sat}}{\partial t}, \frac{\partial h}{\partial t}, \frac{\partial S_l}{\partial t}$ and $\frac{\partial \rho_l}{\partial t}$ in (4.14) gives

$$\begin{aligned} &\phi(\rho_l - \rho_v)\left\{\frac{\partial S_l}{\partial P_l}\frac{\partial P_l}{\partial t} + \frac{\partial S_l}{\partial T}\frac{\partial T}{\partial t} + \frac{\partial S_l}{\partial P_g}\frac{\partial P_g}{\partial t}\right\} \\ &+ \phi S_l\left\{\frac{\partial \rho_l}{\partial P_l}\frac{\partial P_l}{\partial t} + \frac{\partial \rho_l}{\partial T}\frac{\partial T}{\partial t} + \frac{\partial \rho_l}{\partial P_g}\frac{\partial P_g}{\partial t}\right\} + \rho_{sat}\phi S_g\left\{\frac{\partial h}{\partial P_l}\frac{\partial P_l}{\partial t} + \frac{\partial h}{\partial T}\frac{\partial T}{\partial t} + \frac{\partial h}{\partial P_g}\frac{\partial P_g}{\partial t}\right\} \\ &+ h\phi S_g\left\{\frac{\partial \rho_{sat}}{\partial T}\right\}\frac{\partial T}{\partial t} = -\nabla(\rho_l v_l) - \nabla(\rho_v v_v) - \nabla(\rho_v v_g) \end{aligned} \tag{4.15}$$

Equation 4.15 can be rearranged as follows,

$$C_{11}\frac{\partial P_l}{\partial t}+C_{12}\frac{\partial T}{\partial t}+C_{13}\frac{\partial P_g}{\partial t}=-\nabla(\rho_l v_l)-\nabla(\rho_v v_v)-\nabla(\rho_v v_g) \quad (4.16)$$

where,

$$C_{11}=\phi(\rho_l-\rho_v)\frac{\partial S_l}{\partial P_w}+\rho_{sat}\phi S_g\frac{\partial h}{\partial P_w}+\phi S_l\frac{\partial \rho_l}{\partial P_w}$$

$$C_{12}=\phi(\rho_l-\rho_v)\frac{\partial S_l}{\partial T}+\rho_{sat}\phi S_g\frac{\partial h}{\partial T}+\phi S_l\frac{\partial \rho_l}{\partial T}+\phi S_g h\beta$$

$$C_{13}=\phi(\rho_l-\rho_v)\frac{\partial S_l}{\partial P_g}+\rho_{sat}\phi S_g\frac{\partial h}{\partial P_g}+\phi S_l\frac{\partial \rho_l}{\partial P_g}$$

Equation 4.16 can be written as:

$$C_{11}\frac{\partial P_l}{\partial t}+C_{12}\frac{\partial T}{\partial t}+C_{13}\frac{\partial P_g}{\partial t}=J_m \quad (4.17)$$

where J_m is total moisture flux and can be defined as:

$$J_m=-\nabla(\rho_l v_l)-\nabla(\rho_v v_v)-\nabla(\rho_v v_g) \quad \text{or} \quad J_m=-\nabla.(J_l)-\nabla.(J_v)-\nabla.(J_{vg})$$

Constitutive derivation of the right hand side term in the Equation 4.17 (the sum of water leaving or entering the control volume across its boundaries) takes consideration of vapour, gas and liquid velocity in the mass flows of fluid and gaseous water. The generalised form of Darcy's law for the gas and liquid velocities, incorporating the effect of gravity, can be written as:

$$v_l=-\frac{K_{intc}k_l}{\mu_l}[\nabla(P_l+Z)] \quad (4.18)$$

$$v_g=-\frac{K_{intc}k_g}{\mu_g}[\nabla(P_g)] \quad (4.19)$$

where, k_l is the relative permeability to the liquid phase, k_g is the relative permeability to the gaseous gas permeability, K_{intc} is a intrinsic permeability and Z is the vertical elevation from a datum (positive upward).

The diffusion of water vapour was assumed to take place in the part of the pores not filled with liquid and this was represented previously in Equation 3.30. The gradient of vapour density that is given in the vapour diffusion equation can be derived as:

$$\nabla \rho_v = \rho_{sat} \nabla h + h \nabla \rho_{sat} \tag{4.20}$$

Substituting Equation 4.9 and Equation 4.10 for ρ_o and h into Equation 4.20 yields

$$\nabla \rho_v = \rho_{sat} \frac{\partial h}{\partial P_l} \nabla P_l + \rho_{sat} \frac{\partial h}{\partial T} \nabla T + \rho_{sat} \frac{\partial h}{\partial P_g} \nabla P_g + h\beta \nabla T \tag{4.21}$$

Substituting Equation 4.21 in the expression for the vapour velocity Equation 3.30 gives;

$$v_v = \frac{-D_{atm} v \alpha \theta_a}{\rho_v} \left\{ \rho_{sat} \frac{\partial h}{\partial P_l} \nabla P_l + (\rho_{sat} \frac{\partial h}{\partial T} + h\beta) \nabla T + \rho_{sat} \frac{\partial h}{\partial P_g} \nabla P_g \right\} \tag{4.22}$$

Based on the above constitutive equation for liquid transport, diffusion of vapour and bulk flow of vapour, the right hand side term of Equation 4.17 can then be written as;

$$\begin{aligned} J_m &= \nabla \left\{ \rho_l \left(- \frac{K_{int\,c} k_l}{\mu_l} [\nabla (P_l + Z)] \right) \right\} \\ &+ D_{atm} v \alpha \theta_a \left\{ \rho_{sat} \frac{\partial h}{\partial P_l} \nabla P_l + (\rho_{sat} \frac{\partial h}{\partial T} + h\beta) \nabla T + \rho_{sat} \frac{\partial h}{\partial P_g} \nabla P_g \right\} \\ &+ \nabla \{ \rho_v K_g [\nabla P_g] \} \end{aligned} \tag{4.23}$$

Therefore, from Equation 4.17 the governing equation for moisture flow can be written in the following form:

$$\begin{aligned} &C_{11} \frac{\partial P_l}{\partial t} + C_{12} \frac{\partial T}{\partial t} + C_{13} \frac{\partial P_g}{\partial t} = \\ &\nabla(K_{11} \nabla P_w) + \nabla(K_{12} \nabla T) + \nabla(K_{13} \nabla P_g) + \nabla(K_{14} \nabla Z) \end{aligned} \tag{4.24}$$

where,

$$K_{11} = \frac{K_l}{g} + D_{atm} v \alpha \theta_a \left(\rho_{sat} \frac{\partial h}{\partial P_l} \right)$$

$$K_{12} = D_{atm} v \alpha \theta_a \left[(\rho_{sat} \frac{\partial h}{\partial T} + h\beta) \right]$$

$$K_{13} = \rho_v K_g + D_{atm} v \alpha \theta_a \left(\rho_{sat} \frac{\partial h}{\partial P_g} \right)$$

$$K_{14} = \rho_l K_l$$

4.3.2 Derivation of heat transfer

The generated heat is transported by the combination of the three basic mechanisms: conduction, convection and radiation. Conduction involves energy transfer through the contact of materials of different temperature, convection involves the heat transfer between a surface and a moving fluid at different temperatures, and the radiation is the energy transfer through electromagnetic waves when there is no conveying medium present. Although all three modes are manifested during the drying process, their relative importance is different and their contribution to heat transfer changes during the drying of porous media. For example, radiation has negligible contribution to heat transfer during convective drying, and therefore it is not considered in this study. The conservation equation for transport of energy is given by;

$$\begin{aligned} Q = -\lambda_{eff} \nabla T + (T - T_r) \{ \rho_l C_{pl} v_l + \rho_v C_{pv} v_v + \rho_v C_{pv} v_g + \rho_a C_{pa} v_g \} \\ + \{ \rho_v v_v + \rho_v v_g \} L \end{aligned} \tag{4.25}$$

Applying the energy conservation law to the heat flow through the porous shell body indicates that the time derivative of the heat content, $\overline{H}$, is equal to the spatial derivative of the heat flux, Q. Mathematically this can be expressed as;

$$\frac{\partial \overline{H}}{\partial t} = -\nabla . Q \tag{4.26}$$

The heat content of the ceramic porous body per unit volume is defined as

$$\overline{H} = H(T - T_r) + \phi S_g \rho_v L \tag{4.27}$$

where L is the latent heat of vaporisation, T_r is the reference temperature and heat capacity of ceramic body is previously defined in Equation 3.15.

By substituting Equation 4.27 for $\overline{H}$, Equation 4.26 can be expressed as:

$$H\frac{\partial T}{\partial t} + (T - T_r)\frac{\partial H}{\partial t} + \phi\rho_v L\frac{\partial S_g}{\partial t} + \phi S_g L\frac{\partial \rho_v}{\partial t} = -\nabla.Q \tag{4.28}$$

From Equation 3.15, the partial differentiation of the heat capacity in Equation 4.28 with respect to time can be expressed as:

$$\begin{aligned}\frac{\partial H}{\partial t} &= \phi S_l C_{pl}\frac{\partial \rho_l}{\partial t} + \phi\rho_l C_{pl}\frac{\partial S_l}{\partial t} + \phi S_g C_{pv}\frac{\partial \rho_v}{\partial t} \\ &- \phi\rho_v C_{pv}\frac{\partial S_l}{\partial t} + \phi S_g C_{pa}\frac{\partial \rho_a}{\partial t} - \phi_a C_{pa}\rho_a\frac{\partial S_l}{\partial t}\end{aligned} \tag{4.29}$$

Dalton's law of partial pressure states that the total gas pressure is equal to the sum of the partial pressure of each gas component as stated in Equation 3.5 and in Equation 3.6. Mathematically, this can be expressed using the ideal gas laws as follows,

$$P_g = P_v + P_a = \rho_v R_v T + \rho_a RT \tag{4.30}$$

where R is specific gas constant for ideal gas (8.314 J/ mole K) .

Therefore, the density of dry air (ρ_a) is given by,

$$\rho_a = \frac{P_g}{RT} - \frac{\rho_v R_v}{R} \tag{4.31}$$

Using the chain rule, $\nabla\rho_a$ can be written as follows,

$$\nabla \rho_a = \frac{\partial \rho_a}{\partial P_l} \nabla P_l + \frac{\partial \rho_a}{\partial T} \nabla T + \frac{\partial \rho_a}{\partial P_g} \nabla P_g \qquad (4.32)$$

where,

$$\frac{\partial \rho_a}{\partial P_l} = -\frac{\rho_{sat} R_v}{R} \frac{\partial h}{\partial P_w}$$

$$\frac{\partial \rho_a}{\partial T} = -\frac{P_g}{RT^2} - \frac{R_v}{R}\left\{ h\beta + \rho_{sat} \frac{\partial h}{\partial T} \right\}$$

$$\frac{\partial \rho_a}{\partial P_g} = \frac{1}{RT} - \frac{\rho_{sat} R_v}{R} \frac{\partial h}{\partial P_g}$$

Incorporating equations (4.11), (4.12),(4.13),(4.21),(4.32) in Equation 4.28 gives,

$$C_{21} \frac{\partial P_l}{\partial t} + C_{22} \frac{\partial T}{\partial t} + C_{23} \frac{\partial P_g}{\partial t} = -\nabla . Q \qquad (4.33)$$

where,

$$C_{21} = (T - T_r)\left\{ A_{T1} \frac{\partial S_l}{\partial P_l} + \phi S_g C_{pa} \frac{\partial \rho_a}{\partial P_l} + \phi S_g C_{pv} \rho_{sat} \frac{\partial h}{\partial P_l} + \phi S_l C_{pl} \frac{\partial \rho_l}{\partial P_l} \right\}$$

$$- \phi \rho_v L \frac{\partial S_l}{\partial P_l} + \phi S_g L \rho_{sat} \frac{\partial h}{\partial P_l}$$

$$C_{22} = H + (T - T_r)\left\{ A_{T1} \frac{\partial S_l}{\partial T} + \phi S_g C_{pa} \frac{\partial \rho_a}{\partial T} + \phi S_g C_{pv} (h\beta + \rho_{sat} \frac{\partial h}{\partial T}) + \phi S_l C_{pl} \frac{\partial \rho_l}{\partial T} \right\}$$

$$- \phi \rho_v L \frac{\partial S_l}{\partial T} + \phi S_g L (h\beta + \rho_{sat} \frac{\partial h}{\partial T})$$

$$C_{23} = (T - T_r)\left\{ A_{T1} \frac{\partial S_l}{\partial P_g} + \phi S_g C_{pa} \frac{\partial \rho_a}{\partial P_g} + \phi S_g C_{pv} \rho_{sat} \frac{\partial h}{\partial P_g} + \phi S_l C_{pl} \frac{\partial \rho_l}{\partial P_g} \right\}$$

$$- \phi \rho_v L \frac{\partial S_l}{\partial P_g} + \phi S_g L \rho_{sat} \frac{\partial h}{\partial P_g}$$

And,

$$A_{T1} = \phi \rho_l C_{pl} - \phi C_{pv} \rho_v - \phi C_{pa} \rho_a$$

The heat flux per unit area, Q, is defined as

$$\begin{aligned} Q &= -\lambda_{eff}\nabla T + (\rho_v v_v + \rho_v v_g)L \\ &+ (T - T_r)\{\rho_l C_{pl} v_l + \rho_v C_{pv} v_v + \rho_v C_{pv} v_g + \rho_a C_{pa} v_g\} \end{aligned} \tag{4.34}$$

or;

$$Q = \lambda_{eff}\nabla T + (J_v + J_{vg})L + \nabla T(J_l C_{pl} + J_v C_{pv} + J_a C_{pa})$$

where λ_{eff} is the effective (is given in Equation 3.14) thermal conductivity of the ceramic shell body. Interrogation of Equation 4.34 shows the heat flux includes heat transfer due to:

i) Conduction as inter-molecular flow of heat energy

ii) Latent heat flow associated with movement of vapour due to both mechanisms of vapour flow.

iii) Convection of heat due to the mass flow i.e. liquid phase, vapour phase associated with the diffusion mechanism and bulk flow

By substituting Equation 4.34 for Q, Equation 4.33 can be expanded as:

$$\begin{aligned} &C_{21}\frac{\partial P_l}{\partial t} + C_{22}\frac{\partial T}{\partial t} + C_{23}\frac{\partial P_g}{\partial t} \\ &= \nabla(\lambda_{eff}\nabla T) - \nabla(\rho_v v_v + \rho_v v_g)L - \nabla\{(T - T_r)\rho_l C_{pl} v_l\} \\ &- \nabla\{(T - T_r)\rho_v C_{pv} v_v\} - \nabla\{(T - T_r)\rho_v C_{pv} v_g\} - \nabla\{(T - T_r)\rho_a C_{pa} v_g\} \end{aligned} \tag{4.35}$$

Substituting equations (4.18), (4.19) and (4.22) for v_l, v_g and v_v respectively in Equation 4.35, the governing equation for heat transfer can be written as:

$$\begin{aligned} &C_{21}\frac{\partial P_l}{\partial t} + C_{22}\frac{\partial T}{\partial t} + C_{23}\frac{\partial P_g}{\partial t} \\ &= \nabla.(\mathrm{K}_{21}\nabla P_w) + \nabla.(\mathrm{K}_{22}\nabla \mathrm{T}) + \nabla.(\mathrm{K}_{23}\nabla P_g) + \nabla.(\mathrm{K}_{24}\nabla \mathrm{Z}) \end{aligned} \tag{4.36}$$

where,

$$\mathrm{K}_{21} = \rho_v L K_{v1} + C_{pv}\rho_v K_{v2}(T - T_r) + \frac{C_{pl}\rho_l K_l}{\gamma_l}(T - T_r)$$

$$K_{22} = \lambda_{eff} + \rho_v L K_{v2} + C_{pv}\rho_v K_{v2}(T - T_r)$$

$$K_{23} = \rho_v L K_{v3} + \rho_v L K_g + C_{pv}\rho_v K_{v3}(T - T_r) + (T - T_r)K_g\{C_{pv}\rho_v + C_{pa}\rho_a\}$$

$$K_{24} = C_{pl}\rho_l K_l (T - T_r)$$

and

$$K_{v1} = D_{atm} v \alpha \theta_a \left(\rho_{sat} \frac{\partial h}{\partial P_l} \right)$$

$$K_{v2} = D_{atm} v \alpha \theta_a \left[(\rho_{sat} \frac{\partial h}{\partial T} + h\beta) \right]$$

$$K_{v3} = D_{atm} v \alpha \theta_a \left(\rho_{sat} \frac{\partial h}{\partial P_g} \right)$$

4.4.3 Dry gas transfer derivation

The gas phase is more complicated than the solid and the liquid phase since it contains two components: air and vapour as defined in Section 3.2.5. So, in this work other gases that might be exist or produce during the process were neglected. Applying a mass balance to the flow of dry gas within the pores of the ceramic shell body dictates that the time derivative of the dry gas content is equal to the spatial derivative of the dry gas flux plus a condensation term, $\dot{m}$ that has been defined previously in Equation 3.22. Mathematically this can be expressed as

$$\frac{\partial \phi \rho_g S_g}{\partial t} = -\frac{\partial \rho_g v_g}{\partial x} + \dot{m} \tag{4.37}$$

By substituting the evaporation term in Equation (4.3) into the Equation (4.37), reduces the equation to;

$$\frac{\partial \phi S_g \rho_a}{\partial t} = -\frac{\partial \rho_a v_g}{\partial x} - \frac{\partial \rho_v v_v}{\partial x} \tag{4.38}$$

The bulk flow is given by Darcy's law and is governed by the relative gas

permeability, k_g, and at the same time the gas bulk flow due to gravity is assumed not exist in the case of convective drying (Ben Nasrallah, and Perre, 1988). The molecular diffusion rate depends on the effective diffusivity, D_{atm} which was given in the previous derivation and formulation under vapour transport flow in Equation 3.30. By considering the partial differential equation of air gas transport above with respect to time, gives:

$$\frac{\partial \phi S_g \rho_a}{\partial t} = \phi S_g \frac{\partial \rho_a}{\partial t} + \phi \rho_a \frac{\partial S_g}{\partial x} \tag{4.39}$$

Substitute Equation 4.31 and Equation 4.12 into Equation 4.39 and expanding gives;

$$C_{31}\frac{\partial P_l}{\partial t} + C_{32}\frac{\partial T}{\partial t} + C_{33}\frac{\partial P_g}{\partial t} = -\nabla(\rho_a v_g) - \nabla(\rho_v v_v) \tag{4.40}$$

where,

$$C_{33} = \phi S_g \frac{\partial \rho_a}{\partial P_l} - \phi \rho_a \frac{\partial S_l}{\partial P_l}$$

$$C_{32} = \phi S_g \frac{\partial \rho_a}{\partial T} - \phi \rho_a \frac{\partial S_l}{\partial T}$$

$$C_{33} = \phi S_g \frac{\partial \rho_a}{\partial P_g} - \phi \rho_a \frac{\partial S_l}{\partial P_g}$$

The spatial derivative in the right hand side term of Equation 4.38 is obtained by substituting Equation 4.22 and Equation 4.19 to give;

$$C_{31}\frac{\partial P_l}{\partial t} + C_{32}\frac{\partial T}{\partial t} + C_{33}\frac{\partial P_g}{\partial t} = K_{31} + K_{32} + K_{33} \tag{4.41}$$

where,

$$K_{31} = \nabla\left(D_{atm} \alpha v \theta_a \left(\rho_{sat} \frac{\partial h}{\partial P_l} \right) \right)$$

$$K_{32} = \nabla\left(D_{atm} \alpha v \theta_a \left(\rho_{sat} \frac{\partial h}{\partial T} + h\beta \right) \right)$$

$$K_{33} = \nabla\left(D_{atm}\alpha v\theta_a \left(\rho_{sat} \frac{\partial h}{\partial P_g} \right) \right) + \nabla\left(\rho_a K_g \nabla P_g\right)$$

4.3.4 Boundary Conditions

In solving the above governing equations, the conditions for mass heat transfer and gas transport at the external surfaces must be specified in order to establish the flux boundary condition in the convective drying. Both the boundary prescription and the flux boundary condition that were implemented in this work are expanded fully as below.

4.3.4.1 Convection boundary condition

This section will present the boundary conditions calculated using heat and mass transfer coefficients and the consequent fluxes (on the outward normal) on the body surface. The boundary conditions govern the heat and moisture transfer phenomena between the exposed surfaces of the body with the external environment. The magnitude of convection of the heat and mass depends also on the amount of water available in the structure and the void fraction. The higher the initial moisture, the more water is vaporized, increasing the pressure differential and mass flux, thus increasing the rate of the convective mass transfer. The voids in the structure create pathways for convection. The general formulation is given below for convection of mass and heat transfer at the boundary for many drying porous materials such as brick and concerte (Baggio *et al.*, 1997; Nidjam *et al.*, 2000; Zhe Zhang, 1999):

$$J_m = h_m\left(P_{v(\infty)} - P_{v(calculated)}\right) \tag{4.42}$$

$$J_h = h_T\left(T_\infty - T_{calculated}\right) \tag{4.43}$$

At the same time, this condition is balanced by the continuity of moisture transfer normal to the surface as the drying proceeds. This can be expressed as;

$$h_m\left(P_\infty^v - P_{calculated}^{\ v}\right) = \left[-\nabla.(J_v) + \nabla(J_l)\right]n \qquad (4.44a)$$

Or by neglecting the liquid flux contribution to water loss, Equation 4.44a can be written as;

$$-h_m\left(P_\infty^v - P_{calculated}^{\ v}\right) = \left[-\nabla.(J_v)\right]n \qquad (4.44b)$$

By setting the ambient temperature higher than the porous body, heat is transferred to the matrix through the convection process. This will continue until the temperature outside and inside the body are in equilibrium, which must also occur concurrently with the mass convection process. Below is the equation for heat transfer at the convective boundary when considering the continuation of heat flux movement from the body (in Equation 4.25) towards normal the heat convective boundary surface;

$$h_T\left(T_\infty - T_s\right) = \left[\lambda_{eff}\nabla T\right]n \qquad (4.45)$$

where n is the unit outward normal to the surface.

4.3.4.2 Dirichlet boundary conditions

These are applicable to the mass, heat and gas transport equations as specified water potential, temperature and gas pressure at the boundaries respectively. These may be constant or be allowed to vary with time, i.e,

$$P_l(x,t) = \hat{P}_l(x,t) \qquad \text{on } \Gamma_{P_l} \qquad (4.46)$$

$$T(x,t) = \hat{T}(x,t) \qquad \text{on } \Gamma_T \qquad (4.47)$$

$$P_g(x,t) = \hat{P}_g(x,t) \qquad \text{on } \Gamma_{P_g} \qquad (4.48)$$

where $\hat{P}_l, \hat{T}, \hat{P}_g$ are the specified pore water pressure, temperature and gas pressure respectively.

4.3.4.3 The relationship between the heat and mass transfer coefficient and the surface water content

The analogy between heat and mass transfer at the surface of a drying material is covered in standard textbooks (Keey, 1975) where the mass transfer coefficient is applicable principally in the falling rate period. The experimental results Nissan *et. al* (1959) show that the relation between the heat and mass transfer coefficient and the surface water content is as given below and was introduced in this work;

$$h_T = h_{T,0}\left[\eta_T + (1-\eta_T)\frac{S_l - S_{irr}}{S_{cri} - S_{irr}}\right] \tag{4.49}$$

$$h_m = h_{m,0}\left[\eta_h + (1-\eta_h)\frac{S_l - S_{irr}}{S_{cri} - S_{irr}}\right] \tag{4.50}$$

where the S_{irr} is the irreducible saturation, S_{cri} is the critical saturation, and η_T and η_m are constants, determined experimentally and the values are given in Appendix 1 (see Section A1.6). This is not a standard boundary condition, but was explored during the course of this work. This exploration is reported in (Harun *et al.*, April 2007; Harun *et al.*, 2006; Zhang, 1999).

4.4 Closure

The chapter has focused on the derivation of the governing equations that will need to be solved to simulate the drying of a porous material accounting for moisture, heat and gas transport. The governing equations describing moisture transfer, heat transfer and gas transport through a partially saturated ceramic porous body are presented in Equation 4.16, Equation 4.36 and Equation 4.41 respectively. These equations are expressed in terms of three system variables pore-water pressure (P_w), temperature (T) and gas pressure (mixture of air and vapour) (P_g). The model also assigns a convective heat and mass transfer boundary condition to capture the drying mechanism. The formulation of a finite element scheme to solve these equations will be set out in the following chapter.

REFERENCES

Baggio, P., Bonacina, C., and Schrefler, B.A., 1997, Some Considerations on Modelling Heat and Mass Transfer in Porous Media: Transport in Porous Media, v. 28, p. 233-251.

Ben Nasrallah, S., 1988, Detailed Study of A Model of Heat and Mass Transfer During Convective Drying of Porous Media: International Journal Heat and Mass Transfer, v. 31, p. 957-967.

Crapiste, G.H., 1988, Drying of Cellular Material-I, A Mass Theory: Chemical Engineering Science, v. 43, p. 2919-2928.

de Vries, D.A., 1987, The Theory of Heat and Moisture Transfer in Porous Media Revisited: International Journal Heat and Mass Transfer, v. 30, p. 1343-1350.

Jones, S., 1995, The Use of Conductivity as A Means of Assessing The Extent of Wet Back in An Investment Mould: PhD Theses, England, Material and Metallurgy Dept., The University of Birmingham.

Jones, S., and Leyland, S., 1994, Investigation into The Drying Behaviour of Water Based Slurries: I.C.I 42nd Annual Technical Meeting.

Keey, R.B., 1975, Drying Principles and Practice: Great Britain, Pergamon Press.

Liu, B.C., Lui, W., and Peng, S.W., 2005, Study of Heat and Moisture Transfer in Soil with A Dry Surface Layer: International Journal of Heat and Mass Transfer, v. 48, p. 4579-4589.

Mendes, N.P., C. P., 2005, A Method for Predicting Heat and Moisture Transfer Through Multilayered Walls Based on Temperature and Moisture Content Gradients: International Journal of Heat and Mass Transfer, v. 48, p. 37-51.

Nidjam, J.J., Langrish, T.A.G., and Keey, R.B., 2000, A High-Temperature Drying Model for Softwood Timber: Chemical Engineering Science, v. 55, p. 3585-3598.

Nissan, A.H., Kaye, W.G., and Bell, J.R., 1959, Mechanism of Drying Thick Porous Bodies During The Falling Rate Period: AIChE, v. 5.

Patankar, S.V., 1980, Numerical Heat Transfer and Fluid Flow: New York, McGraw-Hill.

Spolek, G.A., and Plumb, O.A., 1980, A Numerical Model of Heat and Mass Transport in Wood During Drying: Drying '80, p. 84-92.

Stanish, M.A, Schajer, G.S., and Kayihan, F., 1986, A Mathematical Model of Drying for Hygroscopic Porous Media: AIChE, v. 32, p. 1301-1311.

Whitaker, S., 1977, Simultaneous Heat, Mass and Momentum Transfer in Porous Media; A Theory of Drying: Advances in Heat Transfer, v. 13, p. 119-203.

Whitaker, S., and Chou, W.T.H., 1983, Drying Granular Porous Media-Theory and Experiment: Drying Technology, v. 1, p. 3-33.

Harun, Z., Gethin, D.T., Lewis, R.W., and Ferguson, W.J., April 2007, Drying of A Multilayer Ceramic Shell Body: The Fifteenth UK Conference of The Association of Computational Mechanics in Engineering.

Harun, Z., Gethin, D.T., Lewis, R.W., and Ferguson, W.J., 2006, Combined Heat and Mass Transfer for Drying Ceramic Shell: The International Symposium on Multiphysics.

Zhang, Z., 1999, Mechanism and Mathematical Model of Heat and Mass Transfer During Convective Drying of Porous Materials: Heat Transfer_Asian Research, v. 28, p. 337-351.

CHAPTER 5

NUMERICAL SOLUTION

CHAPTER LAYOUT

The theoretical formulation of the proposed two-phase flow of the drying model presented in Chapter 4 is complex and governed by a set of second order partial differential equations that need to be solved, subject to incorporating principally convective boundary conditions. The solution is complex because the variables are coupled and the governing equations are nonlinear due to the dependence on the coefficients on the field variables. Analytical solution is unattainable unless the system is one-dimensional with simple boundary conditions and the equation coefficients are linear. Therefore a numerical approximation method is needed to obtain a solution to the governing non-linear partial differential equation set and this will be discussed in this chapter. In this work a weak formulation of the governing equations is obtained by applying Galerkin's procedure for weighted residuals. Terms involving second spatial derivatives are transformed by means of Greens theorem. Then, the field variables are approximated in space using the usual finite element technique, and expressed in terms of their nodal variables. This analysis must include the temporal discretization to capture the transient nature of the drying process. This was achieved by the implementation of a fully implicit backward time stepping scheme and coupled equation set was solved by a skyline solver. Iterations need to be included during the solution process to capture and stabilize the nonlinearity associated with the governing equations describing the drying process. Convergence is monitored between every successive solution steps and is deemed to have been achieved when the specified tolerance criteria have been satisfied. The principles used in the implementation in the finite element method are documented in the work of (Palananthakumar, 2004), but are included here for completeness. Within this work, some numerical developments were undertaken to incorporate boundary conditions that represent a surface that is partially or fully covered by water.

5.1 Introduction

Since the 1950's much literature has been published on coupled heat and mass transfer (de Vries, 1958; Luikov, 1975; Philip and de Vries, 1957; Whitaker, 1977) in which the basic principles of numerical modelling for the drying process, water permeation in soil and hygrothermal flow problems etc are described. In fact, this coupled analysis is being applied to problems, such as drying in unsaturated porous bodies, such as brick, wood, fibre etc. These are characterised by a combination of three phases (solid, liquid and gas). The integration of these mathematical models into a numerical scheme and programming solution has led to the exploration and development of the coupled model to represent heat and flow in a porous structure that has application in various fields. In fact, the use of computer models and solutions has provided a better understanding of the whole process, leading to innovative process improvements. Furthermore, most of the numerical analysis is validated against well documented experimental data and extensive data is available in the open literature (Lewis *et al.*, 1975; Ben Nasrallah and Perre, 1988; Stanish *et al.*, 1986). Simulation is being applied to both hygroscopic (Nijdam *et al.*, 2000) and nonhygroscopic systems (Malan and Lewis, 2003).

To treat the porous medium as a system in which the properties are continuous functions of the space coordinates, numerical methods such as the Finite Element method (FEM), the Finite Difference Method (FDM), Boundary Element Method (BEM), Finite Volume Method (FVM) are very meaningful. The application of the FEM to porous media is becoming increasingly relevant to the application of drying problem, in particular when involving the coupling of fluid and heat flow phases (Lewis *et al.*, 1996; Lewis and Schrefler, 1998). The recognised advantages of using the FEM that remain up to today are:

- Representation of the true physical geometry is easier than with the finite difference method where the geometry is usually adjusted to fit the grid spacing.
- Boundary conditions associated with complicated geometries can be applied in a straight forward consistent manner.

- Variable grid spacing can be used, whereby small elements are used in regions of interest or zones in which rapid changes occur and large elements are used in regions of little interest or slowly changing conditions.
- Universal programs can be written and applied to any geometry and a large number of physically different situations without changing the code.

Because of the aforementioned facts, the FEM is employed for the spatial discretisation in the present work. The methodology is well established and the basic principle of the method is that the behaviour of continuous body can be represented by the combined behaviour of a finite number of subregions, known as elements (Zienkiewicz, 1989). Approximating functions are used to define the response of individual elements to applied load and adjoining elements are interconnected through a finite number of nodal points. Continuity of the variables across element boundaries is satisfied by suitably choosing functions which uniquely define the variables within each element in terms of the nodal values.

In realising a numerical solution, the governing differential equations need to be expressed in a spatially discretised form, and the time variation captured by a finite difference recurrence relationship. This method is widely used in the solution of almost all coupled equations and the strategy and limitations are well documented for a range of transport problems (Murugesan *et al.*, 2002; Tenchev *et al.*, 2001; Thomas and Ferguson, 1999). When handling multiphase flow, multi-component transport, and heat transfer in a multiphase flow system, investigators predominantly use a fully implicit scheme. Although it may be less accurate than an explicit scheme, it does allow larger time steps and is unconditionally stable. Also, this approach was adopted because it had been shown previously to provide stable solutions to the highly non-linear problem under consideration. So in this work, a fully implicit time stepping scheme has been used in the temporal discretisation of the coupled equations.

Transient algorithms must have the property of convergence to be viable. This means that the time discretisation error must approach zero as the size of the time internal, Δt approaches zero. According to the Lax equivalence theorem, if the algorithm is stable and consistent it will converge. It is advantageous in most transient problems to adapt

the time step-size to the temporal gradients of the solution to reduce running costs. This may be done by simply reducing or increasing the time step-size depending upon the number of iterations required for convergence in the previous step. The time step increment is controlled by two factors, maximum iterations and minimum iterations. Should the actual number of iterations for convergence exceed the maximum specified, the time step is reduced. Likewise, should the iteration number be less than minimum, the time step size will be increased. This procedure enables a variables time step size to be employed, which will benefit in the analysis of heat and moisture transfer taking place over a long period of time but with more rapid variations taking place during the initial stages of the process.

In a computational implementation, the solution of the discretized equations leads to the formation of element stiffness and mass matrices of equations that can be assembled and solved conveniently using an appropriate solver. In the present investigation the solution matrix is diagonally dominant and symmetric, so therefore a skyline solver provides the best solution method, saving storage and is easily incorporated into any existing program (Trikha *et al.*, 1996).

The approach adopted in this study employs two-dimensional, eight node iso-parametric elements. Fluid pressures and temperature are taken as the primary unknown variables. The basic concepts and programming method for the finite element formulation employed have been described in detail elsewhere (Hinton and Owen, 1977).

5.2 Implementation of the Finite Element method to spatial discretization of the equations

In Section 4.2, the moisture, heat and gas transport equation have been formulated based on the three variables which are pore water pressure, temperature and gas pressure. The variation of the temperature, gas pressure and water pressure content throughout the domain of interest,Ω, is approximated in terms of the nodal values T_s, P_g, and P_l as follows

$$P_l \approx \hat{P}_l = \sum_{s=1}^{s=n} N_s(x,y) P_{ls} \tag{5.1}$$

$$T \approx \hat{T} = \sum_{s=1}^{s=n} N_s(x,y) T_s \tag{5.2}$$

$$P_g \approx \hat{P}_g = \sum_{s=1}^{s=n} N_s(x,y) P_{gs} \tag{5.3}$$

where $N_s(x,y)$ is the shape function, n is number of nodes in a element (Ω^e) and P_{ls}, T_s and P_{gs} are the nodal values of pore-water pressure, temperature and gas pressure.

The shape functions are normally stated based on the element nodes. Many types of shape function are available e.g. linear, quadratic, cubic, 3-node, 4-node, 6-node, 8-node, 9-node elements, etc and these are well documented in the literature (Zienkiewicz, 1989).

In this work, the eight node serendipity element was selected. By coupling and assembling the discretized equations of moisture, heat and gas transport that have different coupling coefficients leads to non-symmetrical formation of K and C matrices. For a linearised set of governing differential equations these can be expressed in the form shown below.

$$\nabla\begin{pmatrix} K_{11}\nabla P_l + K_{12}\nabla T + K_{13}\nabla P_g + K_{14}\nabla Z \\ K_{21}\nabla P_l + K_{22}\nabla T + K_{23}\nabla P_g + K_{24}\nabla Z \\ K_{31}\nabla P_l + K_{32}\nabla T + K_{33}\nabla P_g + 0 \end{pmatrix} - \begin{pmatrix} C_{11} + C_{12} + C_{13} \\ C_{21} + C_{22} + C_{23} \\ C_{31} + C_{32} + C_{33} \end{pmatrix} \begin{pmatrix} \frac{\partial P_l}{\partial t} \\ \frac{\partial T}{\partial t} \\ \frac{\partial P_g}{\partial t} \end{pmatrix} = 0 \tag{5.4}$$

If the approximations for variables value given by Equations 5.1, Equation 5.2 and Equation 5.3 are substituted into Equations 5.4 a residual error (R_Ω) is obtained. The residual error can be written as:

$$\nabla\begin{pmatrix}(K_{11}\nabla\hat{P}_l)+.(K_{12}\nabla\hat{T})+.(K_{13}\nabla\hat{P}_g)+(K_{14}\nabla Z)\\(K_{21}\nabla\hat{P}_l)+.(K_{22}\nabla\hat{T})+.(K_{23}\nabla\hat{P}_g)+(K_{24}\nabla Z)\\(K_{31}\nabla\hat{P}_l)+.(K_{32}\nabla\hat{T})+.(K_{33}\nabla\hat{P}_g)+0\end{pmatrix}-\begin{pmatrix}C_{11}+C_{12}+C_{13}\\C_{21}+C_{22}+C_{23}\\C_{31}+C_{32}+C_{33}\end{pmatrix}\begin{pmatrix}\frac{\partial\hat{P}_l}{\partial t}\\\frac{\partial\hat{T}}{\partial t}\\\frac{\partial\hat{P}_g}{\partial t}\end{pmatrix}=R_\Omega \quad (5.5)$$

The Galerkin weighted residual approach can be used to minimise this residual error (R_Ω) in Equation 5.5. This states that the integral of the weighted errors (R_Ω) over the element, Ω^e, must be zero and is written mathematically as:

$$\int_{\Omega^e} N_r R_\Omega d\Omega^e = 0 \quad (5.6)$$

with the shape function N_r being used as the weighting for errors over the domain Ω. Substituting Equation 5.5 into Equation 5.6 yields,

$$\int_\Omega N_r\left(\nabla\begin{pmatrix}(K_{11}\nabla\hat{P}_l)+.(K_{12}\nabla\hat{T})+.(K_{13}\nabla\hat{P}_g)+(K_{14}\nabla Z)\\(K_{21}\nabla\hat{P}_l)+.(K_{22}\nabla\hat{T})+.(K_{23}\nabla\hat{P}_g)+(K_{24}\nabla Z)\\(K_{31}\nabla\hat{P}_l)+.(K_{32}\nabla\hat{T})+.(K_{33}\nabla\hat{P}_g)+0\end{pmatrix}-\begin{pmatrix}C_{11}+C_{12}+C_{13}\\C_{21}+C_{22}+C_{23}\\C_{31}+C_{32}+C_{33}\end{pmatrix}\begin{pmatrix}\frac{\partial\hat{P}_l}{\partial t}\\\frac{\partial\hat{T}}{\partial t}\\\frac{\partial\hat{P}_g}{\partial t}\end{pmatrix}\right)d\Omega^e=0 \quad (5.7)$$

A simplified form of Equation 5.7 can be obtained by integrating the dispersive terms by parts. Considering the first term of Equation 5.7 and the first governing equation, integration by parts yields;

$$\int_{\Omega^e} N_r[\nabla.(K_{11}\nabla\hat{P}_l)]d\Omega^e = \int_{\Omega^e}\nabla.(N_r K_{11}\nabla\hat{P}_l)d\Omega^e - \int_{\Omega^e} K_{11}\nabla\hat{P}_l\,\nabla N_r d\Omega^e \quad (5.8)$$

Similarly, the remaining dispersive term are simplified by employing this procedure. Equation 5.7 is therefore written as;

$$\int_{\Omega^e}\left[\begin{bmatrix}\nabla.(N_rK_{11}\nabla\hat{P}_l)-K_{11}\nabla\hat{P}_l\nabla N_r+\nabla.(N_rK_{12}\nabla\hat{T})-K_{12}\nabla\hat{T}\nabla N_r+\\ \nabla.(N_rK_{13}\nabla\hat{P}_g)-K_{13}\nabla\hat{P}_g\nabla N_r+\nabla.(N_rK_{14}\nabla Z)-K_{14}\nabla Z\nabla N_r\end{bmatrix}\right.$$
$$\left.\begin{bmatrix}\nabla.(N_rK_{21}\nabla\hat{P}_l)-K_{21}\nabla\hat{P}_l\nabla N_r+\nabla.(N_rK_{22}\nabla\hat{T})-K_{22}\nabla\hat{T}\nabla N_r+\\ \nabla.(N_rK_{23}\nabla\hat{P}_l)-K_{23}\nabla\hat{P}_l\nabla N_r+\nabla.(N_rK_{24}\nabla Z)-K_{24}\nabla Z\nabla N_r\end{bmatrix}\right.$$
$$\left.\begin{bmatrix}\nabla.(N_rK_{31}\nabla\hat{P}_l)-K_{31}\nabla\hat{P}_l\nabla N_r+\nabla.(N_rK_{32}\nabla\hat{T})-K_{32}\nabla\hat{T}\nabla N_r+\\ \nabla.(N_rK_{33}\nabla\hat{P}_g)-K_{33}\nabla\hat{P}_g\nabla N_r\end{bmatrix}\right]-\begin{bmatrix}N_r(C_{11}\frac{\partial\hat{P}_l}{\partial\hat{a}}+C_{12}\frac{\partial\hat{T}}{\partial\hat{a}}+C_{13}\frac{\partial\hat{P}_g}{\partial\hat{a}})\\ N_r(C_{21}\frac{\partial\hat{P}_l}{\partial\hat{a}}+C_{22}\frac{\partial\hat{T}}{\partial\hat{a}}+C_{23}\frac{\partial\hat{P}_g}{\partial\hat{a}})\\ N_r(C_{31}\frac{\partial\hat{P}_l}{\partial\hat{a}}+C_{32}\frac{\partial\hat{T}}{\partial\hat{a}}+C_{33}\frac{\partial\hat{P}_g}{\partial\hat{a}})\end{bmatrix}d\Omega^e=0 \quad (5.9)$$

Application of Green's theorem to Equation 5.9 gives;

$$\int_{\Omega^e}\left[\begin{bmatrix}-K_{11}\nabla\hat{P}_l\nabla N_r-K_{12}\nabla\hat{T}\nabla N_r-K_{13}\nabla\hat{P}_g\nabla N_r-K_{14}\nabla Z\nabla N_r-\\ N_r(C_{11}\frac{\partial\hat{P}_l}{\partial t}+C_{12}\frac{\partial\hat{T}}{\partial t}+C_{13}\frac{\partial\hat{P}_g}{\partial t})\end{bmatrix}\right.$$
$$\left.\begin{bmatrix}-K_{21}\nabla\hat{P}_l\nabla N_r-K_{22}\nabla\hat{T}\nabla N_r-K_{23}\nabla\hat{P}_g\nabla N_r-K_{24}\nabla Z\nabla N_r-\\ N_r(C_{21}\frac{\partial\hat{P}_l}{\partial t}+C_{22}\frac{\partial\hat{T}}{\partial t}+C_{23}\frac{\partial\hat{P}_g}{\partial t})\end{bmatrix}\right.$$
$$\left.\begin{bmatrix}-K_{31}\nabla\hat{P}_l\nabla N_r-K_{32}\nabla\hat{T}\nabla N_r-K_{33}\nabla\hat{P}_g\nabla N_r-\\ N_r(C_{31}\frac{\partial\hat{P}_l}{\partial t}+C_{32}\frac{\partial\hat{T}}{\partial t}+C_{33}\frac{\partial\hat{P}_g}{\partial t})\end{bmatrix}\right]d\Omega^e$$
$$+\int_{\Gamma^e}\begin{bmatrix}K_{11}\nabla\hat{P}_l+K_{12}\nabla\hat{T}+K_{13}\nabla\hat{P}_g+K_{14}\nabla Z\\ K_{21}\nabla\hat{P}_l+K_{22}\nabla\hat{T}+K_{23}\nabla\hat{P}_g+K_{24}\nabla Z\\ K_{31}\nabla\hat{P}_l+K_{32}\nabla\hat{T}+K_{33}\nabla\hat{P}_g+0\end{bmatrix}n\,d\Gamma^e\Bigg)=0 \quad (5.10)$$

where Γ^e is the element boundary surface.

The surface integrals introduced by Green's theorem in Equation 5.10 will be zero in adjacent elements and will only contribute at the boundary to the domain. From Equation 5.10, the vector of total moisture flux, $\underline{J}_m$, through the domain boundary Γ can be written as:

$$\underline{J}_m=(K_{11}\nabla\hat{P}_w+K_{12}\nabla\hat{T}+K_{13}\nabla\hat{P}_g+K_{14}\nabla Z).\underline{n} \quad (5.11)$$

where ($\bar{n}$ - outward normal vector to the boundary, Γ, of the domain Ω).

Equation 5.10 is further simplified by substitution of the derivatives of the shape function approximation given in Equations 5.1 to 5.3 and Equation 5.11 to give

$$\left(\begin{array}{l}
\left[\begin{array}{l}\int_{\Omega^e}[K_{11}\nabla\underline{N}_r\nabla\underline{N}_s]d\Omega^e\underline{P}_{ls}+\int_{\Omega^e}[K_{12}\nabla\underline{N}_r\nabla\underline{N}_s]d\Omega^e\underline{T}_s+\int_{\Omega^e}[K_{13}\nabla\underline{N}_r\nabla\underline{N}_s]d\Omega^e\underline{P}_{gs}\\ +\int_{\Omega^e}[\underline{N}_rC_{11}\underline{N}_s]d\Omega^e\frac{\partial\underline{P}_{ls}}{\partial t}+\int_{\Omega^e}\underline{N}_rC_{12}\underline{N}_s]d\Omega^e\frac{\partial\underline{T}_s}{\partial t}+\int_{\Omega^e}[\underline{N}_rC_{13}\underline{N}_s]d\Omega^e\frac{\partial\underline{P}_{gs}}{\partial t}-\int_{\Gamma^e}N_r\underline{J}_md\Gamma\end{array}\right]=0\\
\left[\begin{array}{l}\int_{\Omega^e}[K_{21}\nabla\underline{N}_r\nabla\underline{N}_s]d\Omega^e\underline{P}_{ls}+\int_{\Omega^e}[K_{22}\nabla\underline{N}_r\nabla\underline{N}_s]d\Omega^e\underline{T}_s+\int_{\Omega^e}[K_{23}\nabla\underline{N}_r\nabla\underline{N}_s]d\Omega^e\underline{P}_{gs}\\ +\int_{\Omega^e}[\underline{N}_rC_{21}\underline{N}_s]d\Omega^e\frac{\partial\underline{P}_{ls}}{\partial t}+\int_{\Omega^e}\underline{N}_rC_{22}\underline{N}_s]d\Omega^e\frac{\partial\underline{T}_s}{\partial t}+\int_{\Omega^e}[\underline{N}_rC_{23}\underline{N}_s]d\Omega^e\frac{\partial\underline{P}_{gs}}{\partial t}-\int_{\Gamma^e}N_r\underline{J}_md\Gamma\end{array}\right]=0\\
\left[\begin{array}{l}\int_{\Omega^e}[K_{31}\nabla\underline{N}_r\nabla\underline{N}_s]d\Omega^e\underline{P}_{ls}+\int_{\Omega^e}[K_{32}\nabla\underline{N}_r\nabla\underline{N}_s]d\Omega^e\underline{T}_s+\int_{\Omega^e}[K_{33}\nabla\underline{N}_r\nabla\underline{N}_s]d\Omega^e\underline{P}_{gs}\\ +\int_{\Omega^e}[\underline{N}_rC_{31}\underline{N}_s]d\Omega^e\frac{\partial\underline{P}_{ls}}{\partial t}+\int_{\Omega^e}\underline{N}_rC_{32}\underline{N}_s]d\Omega^e\frac{\partial\underline{T}_s}{\partial t}+\int_{\Omega^e}[\underline{N}_rC_{33}\underline{N}_s]d\Omega^e\frac{\partial\underline{P}_{gs}}{\partial t}-\int_{\Gamma^e}N_r\underline{J}_md\Gamma\end{array}\right]=0
\end{array}\right) \quad (5.12)$$

where $\underline{N}_r$ and $\underline{N}_s$ is the shape function in a matrix form and $\underline{P}_{ls}$, $\underline{T}_s$ and $\underline{P}_{gs}$ are the nodal values of the three system variables in a matrix form as follows,

$$\underline{P}_{ls} = \{P_{l1} \quad P_{l2} \quad \ldots \quad \ldots \quad \ldots \quad P_{ln}\}^T \quad (5.13)$$

$$\underline{T}_s = \{T_1 \quad T_2 \quad \ldots \quad \ldots \quad \ldots \quad T_n\}^T \quad (5.14)$$

$$\underline{P}_{gs} = \{P_{g1} \quad P_{g2} \quad \ldots \quad \ldots \quad \ldots \quad P_{gn}\}^T \quad (5.15)$$

(n-number of nodes per elements)

The first part of the Equation 5.12 can be written in a concise matrix as:

$$\underline{K}_{11}\underline{P}_{ls}+\underline{K}_{12}\underline{T}_s+\underline{K}_{13}\underline{P}_{gs}+\underline{C}_{11}\frac{\partial\underline{P}_{ls}}{\partial t}+\underline{C}_{12}\frac{\partial\underline{T}_s}{\partial t}+\underline{C}_{13}\frac{\partial\underline{P}_{gs}}{\partial t}+\underline{J}_1=0 \quad (5.16)$$

where

$$\underline{K}_{11}=\sum_{s=1}^{s=n}\int_{\Omega^e}K_{11}\nabla\underline{N}_r\nabla\underline{N}_sd\Omega^e \quad (5.17)$$

$$\underline{K}_{12}=\sum_{s=1}^{s=n}\int_{\Omega^e}K_{12}\nabla\underline{N}_r\nabla\underline{N}_sd\Omega^e \quad (5.18)$$

$$\underline{K}_{13}=\sum_{s=1}^{s=n}\int_{\Omega^e}K_{13}\nabla\underline{N}_r\nabla\underline{N}_sd\Omega^e \quad (5.19)$$

$$\underline{C}_{11} = \sum_{s=1}^{s=n} \int_{\Omega^e} C_{11} \underline{N}_r \underline{N}_s d\Omega^e \tag{5.20}$$

$$\underline{C}_{12} = \sum_{s=1}^{s=n} \int_{\Omega^e} C_{12} \underline{N}_r \underline{N}_s d\Omega^e \tag{5.21}$$

$$\underline{C}_{13} = \sum_{s=1}^{s=n} \int_{\Omega^e} C_{13} \underline{N}_r \underline{N}_s d\Omega^e \tag{5.22}$$

$$\underline{J}_1 = \int_{\Omega^e} K_{14} \nabla \underline{N}_r \nabla Z d\Omega^e - \int_{\Gamma^e} N_r \underline{J}_m d\Gamma^e \tag{5.23}$$

The same concise form can be written to the others part in Equation 5.12 The whole equations can be combined and expressed more conveniently in matrix form as:

$$\underline{K}(\Phi)\underline{\Phi} + \underline{C}(\Phi)\dot{\underline{\Phi}} + \underline{J}(\Phi) = \{0\} \tag{5.24}$$

where,

$$\underline{K} = \begin{bmatrix} \underline{K}_{11} & \underline{K}_{12} & \underline{K}_{13} \\ \underline{K}_{21} & \underline{K}_{22} & \underline{K}_{23} \\ K_{31} & \underline{K}_{32} & K_{32} \end{bmatrix} \tag{5.25}$$

$$\underline{C} = \begin{bmatrix} \underline{C}_{11} & \underline{C}_{12} & \underline{C}_{13} \\ \underline{C}_{21} & \underline{C}_{22} & \underline{C}_{23} \\ \underline{C}_{31} & \underline{C}_{32} & \underline{C}_{33} \end{bmatrix} \tag{5.26}$$

$$\underline{J} = \begin{Bmatrix} \underline{J}_1 \\ \underline{J}_2 \\ \underline{J}_3 \end{Bmatrix} \tag{5.27}$$

$$\underline{\Phi} = \begin{Bmatrix} \underline{P}_{ls} \\ \underline{T}_s \\ \underline{P}_{gs} \end{Bmatrix} \tag{5.28}$$

$$\dot{\underline{\Phi}} = \begin{Bmatrix} \dfrac{\partial \underline{P}_{ls}}{\partial t} \\ \dfrac{\partial \underline{T}_s}{\partial t} \\ \dfrac{\partial \underline{P}_{gs}}{\partial t} \end{Bmatrix} \tag{5.29}$$

In which typical elements of the matrix are

$$\underline{K}_{ij} = \sum_{s=1}^{n} \int_{\Omega^e} K_{ij} \nabla N_r \nabla N_s d\Omega^e \qquad \text{(i, j=1,2,3)} \tag{5.30}$$

$$\underline{C}_{ij} = \sum_{s=1}^{n} \int_{\Omega^e} C_{ij} N_r N_s d\Omega^e \tag{5.31}$$

$$\underline{J}_i = \int_{\Omega^e} K_{i4} \nabla N_r \nabla z d\Omega^e - \int_{\Gamma^e} N_r \underline{J}_i . n d\Gamma^e \tag{5.32}$$

($\bar{n}$ - outward normal vector to the boundary, Γ, of the domain Ω)

5.3 Temporal Discretisation - Time Stepping Algorithms

The matrix Equation 5.24 generates a system of first order linearised differential equations. This can be written in a more concise form as follows:

$$\underline{K}(\Phi)\underline{\Phi} + \underline{C}(\Phi)\dot{\underline{\Phi}} + \underline{J}(\Phi) = \{0\} \tag{5.33}$$

where, K, C, J and Φ are the matrices defined in Equations 5.25 to 5.28.

The time derivative is replaced by a finite difference approximation and, consequently, a fully implicit backward level time stepping scheme results:

$$\underline{K}(\underline{\Phi}^{\bar{n}}).\underline{\Phi}^{n+1} + \underline{C}(\underline{\Phi}^{\bar{n}}) \frac{\underline{\Phi}^{n+1} - \underline{\Phi}^{n}}{\Delta t} + \underline{J}(\underline{\Phi}^{\bar{n}}) = 0 \tag{5.34}$$

where $\underline{\Phi}^{\bar{n}}$, the level at which the matrices $\underline{K}$, $\underline{C}$ and $\underline{J}$ are to be evaluated, is given by,

$$\underline{\Phi}^{\bar{n}} = \left(\frac{\underline{\Phi}^{n+1} + \underline{\Phi}^{n}}{2} \right) \tag{5.35}$$

where ϖ defines the required interval, with value 1 for the

Equation 5.34 can be rearranged as:

$$\left\{\underline{K}(\underline{\Phi}^{\bar{n}})+\frac{\underline{\underline{C}}(\Phi^{\bar{n}})}{\Delta t}\right\}\underline{\Phi}^{n+1}=\left\{\frac{\underline{\underline{C}}(\Phi^{\bar{n}})\underline{\Phi}^{n}}{\Delta t}-\underline{J}(\Phi^{\bar{n}})\right\} \tag{5.36}$$

From Equation 5.36, $\underline{\Phi}^{n+1}$ can be computed as follows.

$$\underline{\Phi}^{n+1}=\left\{\underline{K}(\underline{\Phi}^{\bar{n}})+\frac{\underline{\underline{C}}(\Phi^{\bar{n}})}{\Delta t}\right\}^{-1}\left\{\frac{\underline{\underline{C}}(\Phi^{\bar{n}})\underline{\Phi}^{n}}{\Delta t}-\underline{J}(\Phi^{\bar{n}})\right\} \tag{5.37}$$

The superscript $\bar{n}$ refers to the time level and Δt is time step. It can be seen that the solution for $\underline{\Phi}$ at time level n+1 ($\underline{\Phi}^{n+1}$) can be obtained directly from the matrices of coefficients $\underline{K}$, $\underline{\underline{C}}$ and $\underline{J}$, and $\underline{\Phi}$ at time level n ($\underline{\Phi}^{n}$).

The procedure for solving the above algorithm is iterative because of the non-linear nature of the phenomenological coefficients i.e. $\underline{K}$, $\underline{\underline{C}}$ and $\underline{J}$. A Picard iterative method is utilised to account for non-linearity (Skorokho *et al.*, 1973). A converged solution is deemed to have been achieved when the iteration error (the difference of Φ between successive iterations) falls below a specified tolerance at all nodes. This can be expressed mathematically as:

$$\left|\Phi_{s}^{n+1}-\Phi_{s-1}^{n+1}\right|<\varepsilon \tag{5.38}$$

where ε is a prescribed tolerance and subscript 's' is the iteration number.

In order to stabilise and to increase the convergence rate of the iterative procedure, it is often desirable to slow down the changes that occur in the system variable from one iteration to the next. This process is known as under-relaxation and is given by:

$$\Phi_{s+1}=\omega\Phi_{s}+(1-\omega)\Phi_{s-1} \qquad \text{where } 0<\omega\leq 1 \tag{5.39}$$

The system of simultaneous equations, generated within each iteration, is diagonally dominant and block symmetric and this property assures a stable solution may be achieved using a range of direct or iterative solvers. In this work a well established

memory efficient Skyline scheme was used (Balasubramanian P. *et al.*, 1991).

For an efficient solution over a long time scale (a few hours) that is also capable of capturing transient details, early in the drying process requires the implementation of a variable time stepping scheme. The number of iterations required to reach convergence plays an important role in determining the time step increment. In implementation, two constants, a minimum and maximum number of iterations, are set. When the number of iterations required for convergence falls below the minimum, the time-step size is increased. Similarly, when the number of iteration exceeds the specified maximum, the time-step size is reduced. This condition enables a variable time stepping scheme to be employed. When the time step is reduced, the current time step is factored by A ($A<1.0$) and when it is increased, the factor value assigned is B ($B>1.0$).

5.4 Incorporation of Boundary Conditions

The discretised governing equations are to be solved simultaneously within a domain Ω, bound by a closed curve Γ, subject to boundary conditions and to initial conditions.

Dirichlet boundary conditions take the form of prescribed values for the system variables along all or part of the boundary. This is implemented in the model by equating the prescribed values of system variables to $\underline{\Phi}$ in Equation 5.27.

Convective boundary conditions take the form of prescribed fluxes for moisture and heat loss across the boundary Γ or part of the boundary. The relationship between moisture content, vapour and temperature through thermodynamic equilibrium, results in an air phase flux (as a gas pressure) that changes through convection at the boundary. This can be modelled in the boundary system by substituting the prescribed flux into the J matrix.

5.5 Closure

The finite element solution of the governing system of three fully coupled non-linear partial differential equations described in Chapter 4 has been described. This macroscopic balance equations, after introduction of the This includes a spatial solution by the finite element method using the Galerkin Weighted Residual technique. his This was followed by the temporal discretization of the coupled set by the finite difference method using a fully implicit backward time-stepping algorithm. Nonlinearity was taken into account by implementing an iterative procedure incorporating an under relaxation to stabilise and increase the convergence rate. The simultaneous equation set within each iteration was solved using a skyline solver due to the fact that the generated system was diagonally dominant and block symmetric.

REFERENCES

Balasubramanian, P., Suhas, H.K., and Ramamurti, V., 1991, Skyline Solver for The Static Analysis of Cyclic Symmetrical Structures: Computers & Structures, v. 38, p. 259-268.

Ben Nasrallah, S., and Perre, P., 1988, Detailed Study of A Model of Heat and Mass Transfer During Convective Drying of Porous Media: International Journal Heat Mass Transfer, v. vol 31, p. 957-967.

de Vries, D.A., 1958, Simultaneous Transfer of Heat and Moisture in Porous Media: Trans. Am Geophys Union, v. 39, p. 909-916.

Hinton, E., and Owen, D.R.J., 1977, Finite Element Programming: London.

Lewis, R.W., Comini, G., and Humpheson, C., 1975, Finite Element Application to Heat and Mass Transfer Problems in Porous Bodies: Inzh. Fiz. Zh, v. 20, p. 483-489.

Lewis, R.W., Morgan, K., and Thomas, H.R., 1996, The Finite Element Method in Heat Transfer Analysis: West Sussex, England, John Wiley & Sons.

Lewis, R.W., and Schrefler, B.A., 1998, The Finite Element Method in The Static and Dynamic Deformation and Consolidation of Porous Media: England, Wiley.

Luikov, A.V., 1975, Heat and Mass Transfer in Capillary Porous Bodies: Oxford Pergamon.

Malan, A.G., and Lewis, R.W., 2003, Modelling Coupled Heat and Mass Transfer in Drying Non-hygroscopic Capillary Particulate Materials: Communication in Numerical Method in Engineering, v. 19, p. 669-677.

Murugesan, K., Thomas, H.R., and Cleall, P.J., 2002, An Investigation of The Influence of Two-Stages Drying Conditions on Convective Drying of Porous Materials: International Journal of Numerical Methods for Heat and Fluid Flow, v. 12, p. 29-46.

Nijdam, J.J., Langrish, T.A.G., and Keey, R.B., 2000, A High Temperature Drying Model for Softwood Timber: Chemical Engineering Science, v. 55, p. 3585-3598.

Palananthakumar, B., 2004, A Finite Element Analysis of The Migration and Generation of Landfill Gas through Unsaturated Soil: PhD Theses, Herriot-watt University.

Philip, J. R., and de Vries, D.A., 1957, Moisture movement in Porous Materials Under Temperature Gradients: Trans. Am. Geophys. Union, v. 38, p. 222-232.

Skorokho, V.B., Khariton, P.M., and Dobryako,V.M., 1973, Calculation of Nonlinear Thermal-Conductivities by Picard Method: High Temperature, v. 11, p. 621-622.

Stanish, M.A, Schajer, G.S., and Ferhan, K., 1986, A Mathematical Model of Drying for Hygroscopic Porous Media: AIChE, v. 32, p. 1301-1311.

Tenchev, R.T., Li, L.Y., Purkiss, J.A., and Khalafallah, B.H., 2001, Finite Element Analysis of Coupled Heat and Mass Transfer in Concrete When It Is in A Fire: Magazine of Concrete Research, p. 117-125.

Thomas, H.R., and Ferguson, W.J., 1999, A Fully Coupled Heat and Mass Transfer Model Incorporating Contaminat Gas transfer in An Unsaturated Porous Medium: Computers and Geotechnics, v. 24, p. 65-87.

Trikha, D.N., Bhandari, N.M., and Saxena, N.K., 1996, Modified Profile Solver for Finite-Infinite Coupled Problems: Computers and Structures, v. 59, p. 387-390.

Whitaker, S., 1977, Simultaneous Heat, Mass and Momentum Transfer in Porous Media; A Theory of Drying: Advances in Heat Transfer, v. 13, p. 119-203.
Zienkiewicz, O.C., Taylor R.L., 1989, The Finite Element Method: London, Mc-Graw-Hill.

CHAPTER 6

RESULTS AND VALIDATIONS

CHAPTER LAYOUT

This chapter describes the exploration of the proposed model that is governed by the theoretical formulation and implemented in the numerical scheme set out in the previous chapters. The validation comprises three parts. The first is the problem of one dimensional heat transfer, accounting for Dirchlet and flux boundary conditions. This is followed by the validation of the coupled heat, mass and gas transport model where validation is based on experiment and numerical work. The third stage of validation of the fully coupled model is extended to include shell drying, including a multilayer system. Finally, the proposed model is used to explore drying of a generic corner shape to illustrate the transport mechanisms that take place.

6.1 Introduction

This chapter deals with the validation and the verification of the proposed model in order to test the scheme described in Chapter 3 and to examine the accuracy of the numerical solution methods described in Chapter 4. A series of case studies was chosen with the aim of rigorously testing the developed model by comparison against a variety of analytical solutions, previously verified numerical works and experimental results.

Verification of the model is carried out with different related problems. In Section 6.2, the linear heat flow incorporating the prescribed (Dirichlet) and the flux (Neumann) boundary conditions were solved numerically using the thermal model incorporated into the code, and the computed numerical results compared with analytical solutions given by Carslaw and Jaeger (1959).

In Section 6.3, a one dimensional verification of the fully coupled proposed model which has been derived in Chapter 4 was tested for a convection drying process with application to the benchmark brick drying problem. This exercise considers the simulation of temperature, pore water and gas pressure, moisture movement, relative humidity and the other related transport parameters within the brick. The results obtained from the proposed model are compared with the experimental results presented by Stanish *et al.* (1986).

Section 6.4 describes the implementation of the proposed model that has been verified against the brick benchmark to a two dimensional shell drying problem. This section considers the simulation of a single and a multilayer shell in which the wet layering of the ceramic shell build-up process is approximated. In these works, a plain linear shell section and a generic corner shape was investigated and compared against some experimental data from industrial work. Two different case studies (for the linear section) which describe the layering process in the ceramic shell build up process were proposed in order to determine the ability of the model to capture shell drying. Some comparison between the two proposed methods are also included here.

6.2 Thermal model verification against analytical solution

In analysing the thermo-physical response for the drying of a porous body, heat conduction plays an important role in providing information for the moisture and gas transport contribution. The solutions to thermal problems have been studied extensively and have led to analytical solutions that may be used to benchmark numerical approximations. These have been formulated, principally in one and two dimensions and in this work a one dimensional linear heat flow accommodating various initial conditions and boundary conditions is used to examine the accuracy of the solutions obtained by the numerical solution technique. Two case studies, which incorporate Dirichlet and flux boundary conditions are solved numerically using the proposed model. The computed numerical results are compared with the analytical solutions derived from a series expansion (Carlaw and Jaeger , 1959).

6.2.1 Dirichlet boundary conditions

In this case, a simple problem with a Dirichlet boundary condition is considered, featuring the non-steady heat flow in a solid bounded by a pair of parallel planes, usually referred to as a 'slab 0<x<l'. The slab of length L, has an initial temperature T_o, and both ends are held fixed at the 0°C and with no loss of heat from top and bottom surfaces. The temperature along the length of the slab, after a certain time, is computed using the model.

Using the energy balance, the heat transfer across a domain in the rod can be written as;

$$\frac{\partial\left(\rho C_p\left(T-T_r\right)\right)}{\partial t}=\nabla\left(\lambda_{con}\nabla T\right) \tag{6.1}$$

where ρ, C_p and λ_{con} are the density, the heat capacity and thermal conductivity of the medium respectively.

Equation 6.1 can be simplified into one dimensional systems as follows;

$$\frac{\partial T}{\partial t} = k_T \frac{\partial^2 T}{\partial x^2} \tag{6.2}$$

where $k_T = \frac{\lambda_{con}}{\rho C_p}$

Expressed mathematically, the boundary conditions are:

$T(x, 0) = T_0\ ^\circ C$

$T(0,t) = 0\ ^\circ C$

$T(L,t) = 0\ ^\circ C$

The series expansion analytical solution for the problem described above is given by Carslaw and Jaeger (1959) and is expressed in Equation 6.3. The series expansion comprising up to 100 terms was found to be adequate.

$$T(x,t) = 4\frac{T_0}{\pi}\sum_{n=0}^{100}\frac{1}{2n+1}\sin\left[(2n+1)\pi\frac{x}{L}\right]e^{-K(2n+1)^2\pi^2\frac{t}{L^2}} \tag{6.3}$$

The following values were taken for this test case.

L=1m, $k_T=10^{-5}\ m^2/sec$, $T_o=30\ ^\circ C$.

The problem considered in this case was solved numerically using a domain of 1.0 m length and 0.05 m width. The initial temperature of the sample was set as 30°C. The temperature at both ends was fixed at 0°C. To simulate heat transfer in the slab, a uniform mesh comprising 200 elements, each 5mm thick, was used. The spatial discretisation is shown in Figure 6.1. A variable time step, based on an initial and maximum time step size of 0.001 and 1 sec respectively, was employed for the simulation. The analytical solution for the temperature along the sample was computed from Equation 6.3.

Numerical and analytical results of temperature along the sample from x=0 to x= 0.5 m at times of 240 seconds and 2400 seconds are itemised in Table 6.1. The same result was recorded for the other half (from x=0.5m to x=1.0m) due to the symmetry of the specimen and boundary conditions. The comparison and errors between numerical and analytical results are shown in Figures 6.2 and 6.3. The percentage error was computed as follows:

$$error(\%) = \frac{anal.solution - num.solution}{anal.solution} * 100 \qquad (6.4)$$

In the early stage of simulation, for example at t=240 sec in Figure 6.2, the numerical results deviate slightly from the analytical, but the maximum observed error is only 0.0026%. This error shows the dispersion in the numerical solution at the beginning of the process. However, as time proceeds and as the steady state is approached, the effect of this numerical phenomenon is minimised and the deviation of the numerical results from the analytical results becomes very low at 2400 seconds (see Figure 6.3). These trends are identical to those observed in (Palananthakumar, 2004).

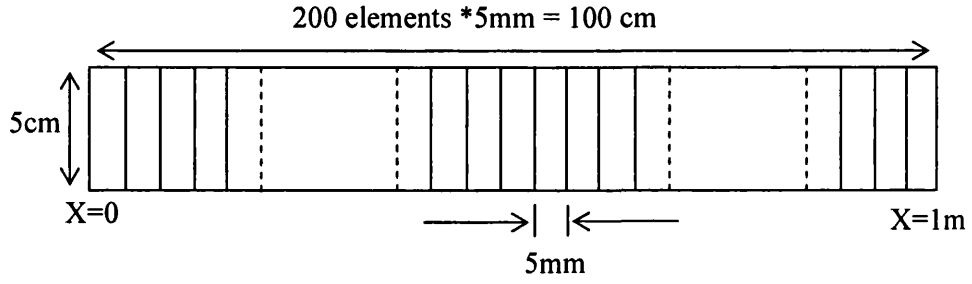

Figure 6.1: Schematic of the figure and finite element mesh for the thermal case study.

Table 6.1: Comparison between analytical and numerical results – case study one - Dirichlet boundary conditions.

x(m)	t = 240 seconds		t = 2400 seconds	
	Analytical	Numerical	Analytical	Numerical
0	0	0	0	0
0.025	8.4535200	8.4309001	2.7252900	2.7209416
0.05	15.8854000	15.8648877	5.4153100	5.4125692
0.075	21.6295000	21.6109351	8.0361500	8.0344318
0.1	25.5326000	25.5158253	10.5565000	10.5554153
0.125	27.8641000	27.8489628	12.9488000	12.9481221

0.15	29.0885000	29.0748599	15.1900000	15.1895932
0.175	29.6538000	29.6415287	17.2622000	17.2619737
0.2	29.8833000	29.8722826	19.1529000	19.1527847
0.225	29.9651000	29.9552341	20.8550000	20.8549498
0.25	29.9908000	29.9819937	22.3665000	22.3664795
0.275	29.9979000	29.9900804	23.6897000	23.6896915
0.3	29.9996000	29.9926970	24.8310000	24.8309966
0.325	29.9999000	29.9938649	25.7992000	25.7992001
0.35	30.0000000	29.9947925	26.6053000	26.6052995
0.375	30.0000000	29.9955931	27.2611000	27.2610999
0.4	30.0000000	29.9963835	27.7783000	27.7783000
0.425	30.0000000	29.9971789	28.1678000	28.1678000
0.45	30.0000000	29.9979959	28.4389000	28.4389000
0.475	30.0000000	29.9988559	28.5986000	28.5986000
0.5	30.0000000	29.9997808	28.6513000	28.6513000

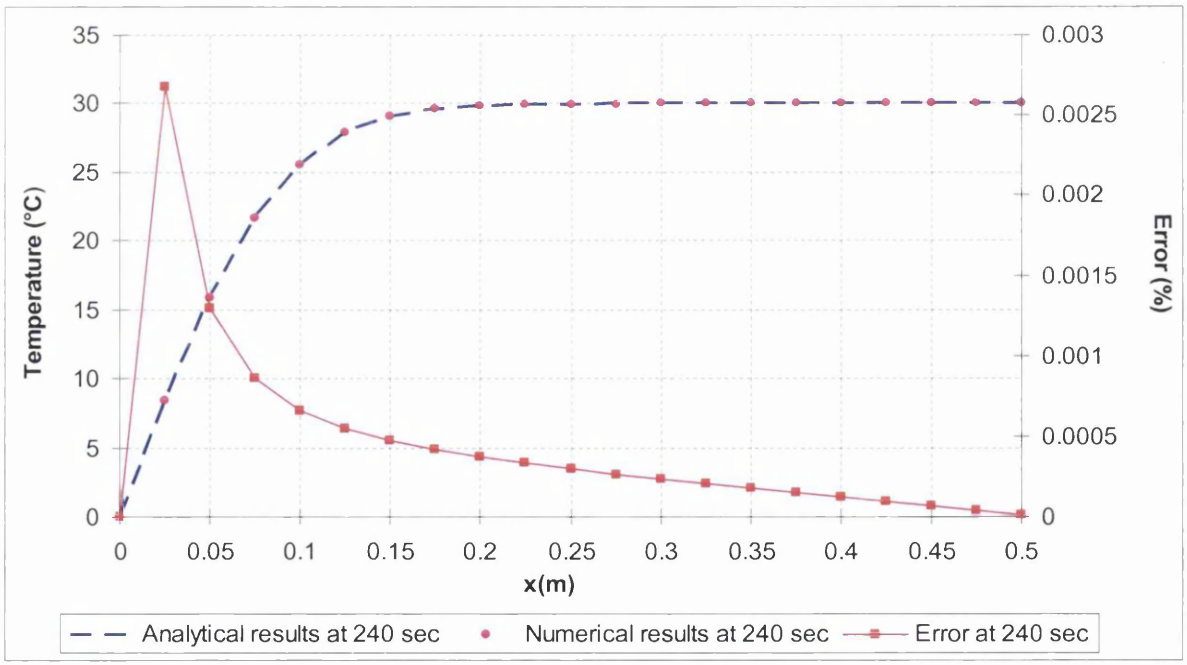

Figure 6.2: Comparison between the analytical and numerical results in case study one at 240 seconds.

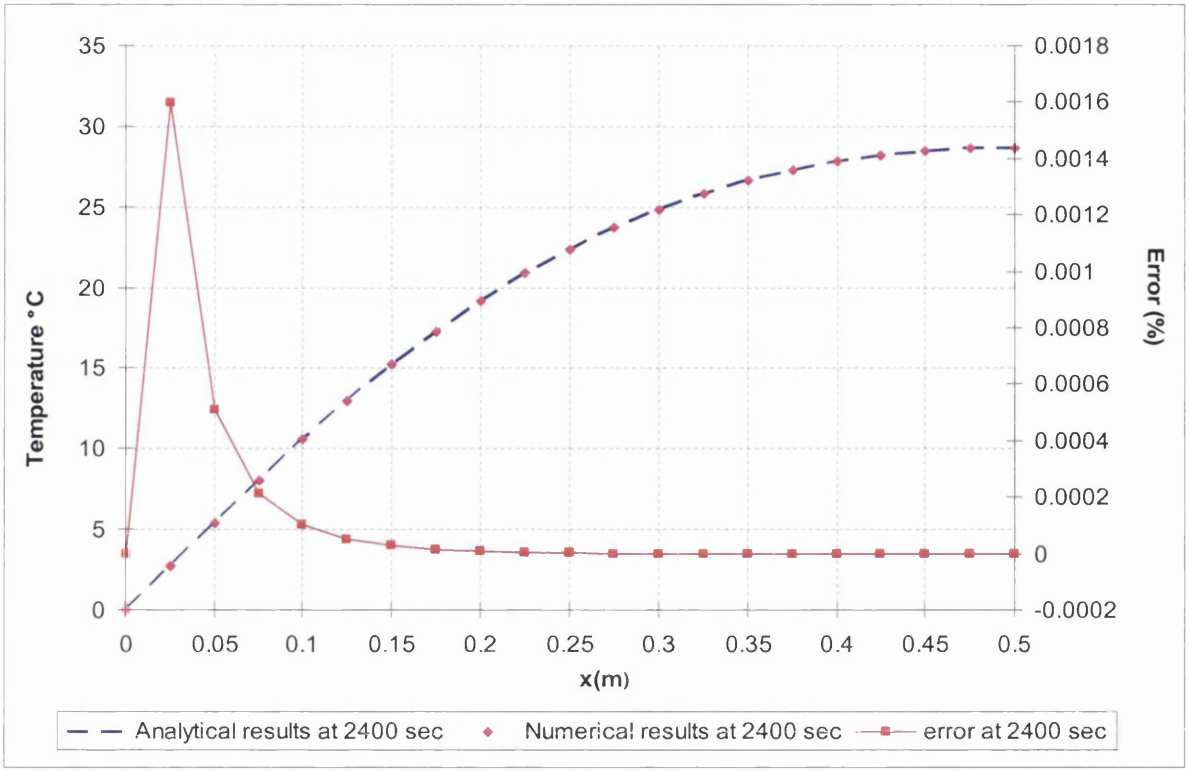

Figure 6.3: Comparison between the analytical and numerical results in case study one at 2400 seconds.

In general, both Figures 6.2 and 6.3 show a very good agreement both spatially and temporally. This leads to the conclusion that the thermal model gives accurate answers when solving numerically the heat conduction and diffusion equations when subjected to prescribed temperature (Dirichlet) boundary conditions.

6.2.2 Flux boundary condition

This case study determines the capability of the numerical model to solve the energy equation (as presented in Equation 6.1) when subjected to a combination of prescribed and flux type boundary conditions. In this case, the slab (Figure 6.1) has a zero initial temperature. A non-zero flux is applied at one end of the slab, the other end is maintained at the initial temperature. There is no loss of heat from its surface. Expressed mathematically, these can be stated as follows:

$T(x, 0)= 0$

$T(0, t) = 0$

$F_T(L, t) = F_o$

The series expansion analytical solution for the problem described above is given in Carslaw and Jaeger (1959) and is expressed in Equation 6.3. An expansion comprising up to 200 terms (n=200) was found to be adequate.

$$T(x,t) = \frac{F_o x}{K} - \frac{8F_o L}{K\pi^2}\sum_{n=0}^{200}\frac{(-1)^n}{(2n+1)^2}\sin\left[\frac{(2n+1)\pi x}{2L}\right].e^{\frac{-K(2n+1)^2\pi^2 t}{4L^2}}dx \qquad (6.5)$$

The following values were taken for this case study.

L=1m, $K=10^{-5}$ m^2/sec, $F_o = 0.002$ J/m^2/sec.

A variable time step, based on an initial and a maximum time step size of 0.01 and 1 sec respectively, was employed for the simulation. The analytical solution for the temperature along the sample was computed from Equation 6.5.

Table 6.2: Comparison between numerical and analytical results– case study 2 - Flux boundary condition.

	t = 1000 sec		t = 2000 sec	
x(m)	Numerical	Analytical	Numerical	Analytical
0	0	0	0	0
0.025	0	0	6.3E-06	2.1E-06
0.05	0	0	1.53E-05	0.000006
0.075	0	0	3.03E-05	1.79E-05
0.1	0	0	5.68E-05	3.75E-05
0.125	0	0	0.000104	8.36E-05
0.15	0	0	0.000187	0.000159
0.175	0	5E-09	0.000333	0.000292
0.2	1E-07	8E-08	0.000582	0.000542
0.225	2E-07	2.5E-07	0.001003	0.000958
0.25	6E-07	5.5E-07	0.001706	0.001642
0.275	1.7E-06	1.9E-06	0.00286	0.002775
0.3	4.3E-06	0.000005	0.004728	0.004629
0.325	1.07E-05	0.00001	0.007708	0.007584
0.35	2.59E-05	0.00003	0.012394	0.012244
0.375	6.11E-05	0.000009	0.019657	0.019455

0.4	0.00014	6.51E-05	0.03075	0.030498
0.425	0.000313	0.000252	0.047451	0.047155
0.45	0.000678	0.000588	0.072235	0.07186
0.475	0.00143	0.00132	0.108495	0.108036
0.5	0.002933	0.002772	0.160791	0.160246
0.525	0.005854	0.005692	0.235153	0.234515
0.55	0.011365	0.011105	0.339412	0.338662
0.575	0.021472	0.021146	0.48355	0.482707
0.6	0.039483	0.039014	0.680066	0.679153
0.625	0.070677	0.070072	0.944313	0.943334
0.65	0.123193	0.122407	1.294793	1.29378
0.675	0.209149	0.208176	1.753369	1.75237
0.7	0.345954	0.34479	2.345353	2.34441
0.725	0.557733	0.556416	3.099442	3.0986
0.75	0.876685	0.875298	4.047463	4.0468
0.775	1.344167	1.34279	5.223907	5.22345
0.8	2.011219	2.01001	6.665238	6.66504
0.825	2.938225	2.93735	8.408995	8.40911
0.85	4.193492	4.19311	10.4927	10.4931
0.875	5.850596	5.8508	12.9526	12.9534
0.9	7.984551	7.98542	15.82241	15.8235
0.925	10.66705	10.6685	19.1319	19.1332
0.95	13.96123	13.9632	22.90576	22.9073
0.975	17.9166	17.919	27.16245	27.1641
1	22.56476	22.5672	31.91339	31.915

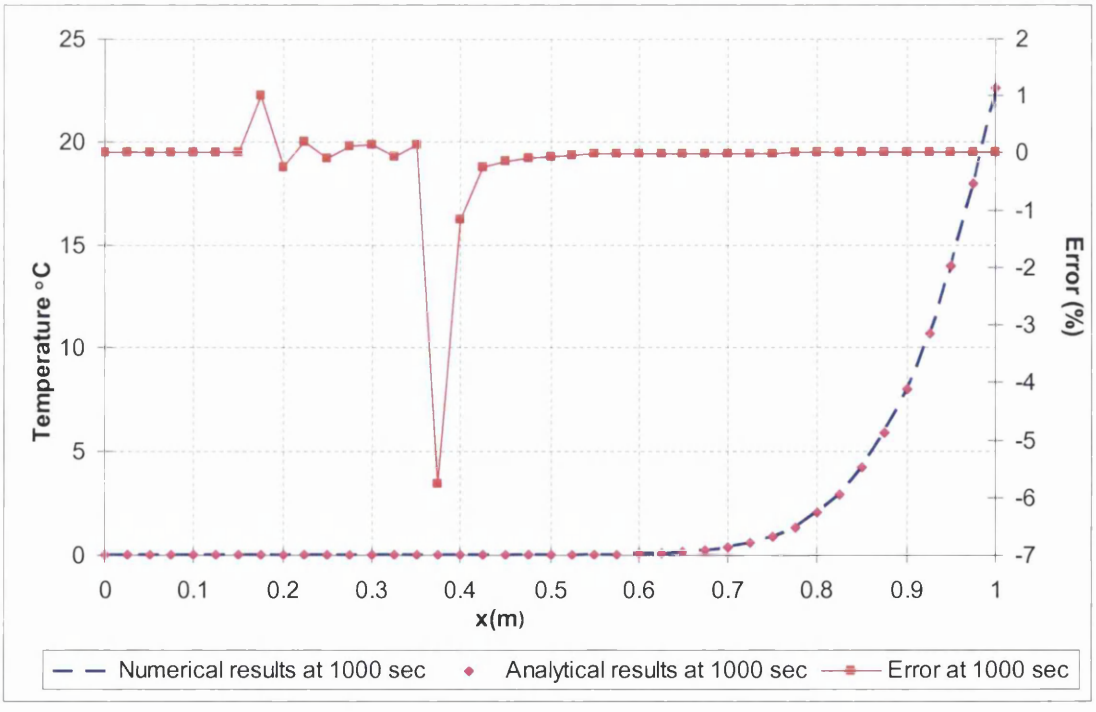

Figure 6.4: Comparison between the analytical and numerical results in case study two at 1000 seconds.

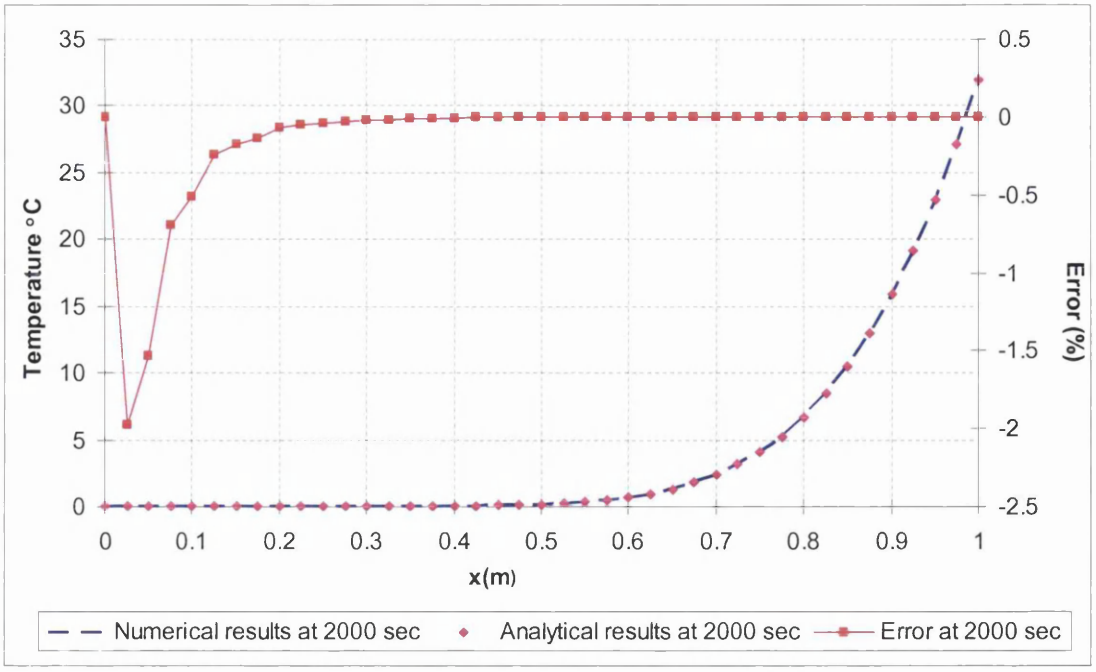

Figure 6.5: Comparison between the analytical and numerical results in case study two at 2000 seconds.

Analytical and numerical results of temperature along the sample at time of 1000 sec and 2000 sec are presented in Table 6.2. The percentage error has also been computed and the differences between the analytical and numerical results are also shown in Figure 6.4 and 6.5. Some numerical dispersion in the early stages indicates that the computed nodal temperatures are slightly higher than the analytical solution. Again, the same reduction in dispersion is recorded in this case study as time increases. The results also show differences at discrete points (x=0.375 at 1000s and x=0.025 at 2000s). However, the numerical values are small and so the analytical and numerical values of temperature are actually very close together.

In general, a very good agreement, spatially and temporally, between analytical and numerical results is observed at both t=1000 seconds and t=2000 seconds. The same pattern of dispersion and its reduction with time as reported in (Palananthakumar, 2004) is again experienced. The conclusion from these case studies is that the numerical implementation of the thermal model is functional and accurate for both prescribed and flux type boundary conditions. Thus it is suitable for coupling with the equations for moisture and gas transport.

6.3 Mathematical model validation on convection drying of a brick

This section explains the verification of the fully coupled heat and mass transfer along with the gas transport equation when applied to convective drying of a brick. This fully coupled model consists of moisture transport by capillary and vapour diffusion together with the gas transport mechanism. Energy transfer accounts for conduction, latent heat and convection. The gas transport is governed by the air pressure gradient due to the bulk condition and vapour diffusion due to the partial vapour pressure. The problem chosen to validate this coupled model was a drying experiment reported by Stanish *et al.* (1986). For convenience, this experimental work is summarised in the next section.

6.3.1 Background to the drying brick case study problem by Stanish *et al* (1986)

In this work, a comprehensive mathematical model was developed to simulate the drying of a non-hygroscopic (brick) body and a hygroscopic material (wood). The model equations are fully coupled heat transfer (by both conduction and convection) together with mass transfer (by gaseous diffusion and bulk flow of gas and liquid through the void space). The governing equation was solved using the continuous time approach (finite_space) and the spatial approximation of derivatives was expressed in finite-difference form.

To complement the numerical work an experimental programme was also conducted to facilitate validation of predicted temperature variation and moisture movement during the drying process for both nonhygroscopic and hygroscopic materials. With a focus on the nonhygroscopic material, the drying rate experiment was performed using a porous ceramic brick with geometry 22.7cm long x 10.4cm wide x 3.2cm high. The sample was dried to achieve an initial dry weight of 1.55kg and after repeated pressure impregnation cycles, the brick absorbed a maximum of 200g of water. The saturated brick was then inserted flush into a well that had been machined in a 40 cm long section of dry 2 x 6 inches wood. The side and bottom surfaces of the brick were sealed with 3 mm thick rubber sheets, thus ensuring a tight fit, preventing moisture loss from those five surfaces with an added benefit of providing a level of

thermal insulation. Drying rate experiments were performed in a specially designed drying chamber. The specimen was suspended from a load cell and positioned so that its upper and lower surfaces were flush with an air flow divider both upstream and downstream of the sample. Air at controlled and measured dry bulb temperature, dew point temperature, and linear velocity was circulated past the specimen, and the sample weight and internal body temperature at 3 points (at the centreline, quarter line and within approximately 1 mm of the surface) were recorded over a period of time. Flow in the channel below the specimen was blocked. In this work, the test was carried out at two different drying conditions, at 75°C and 125°C. In general, this experiment is a basic or simple procedure that captures the temperature and total moisture loss from the brick in an approximately one dimensional manner. However this measurement could be improved by measuring temperature and moisture levels at points through the brick depth so that a more detailed description of temperature and moisture level could be obtained. Further, statistical confidence could be obtained by repeating the same schedule experiments several times. However, for now it remains as the best benchmark and so it has been adopted in this study.

6.3.2 Results validation on the drying convection of a brick problem

The geometry was described by a rectangular domain having the dimensions of the component described in the above section, i.e. length 22.7 cm by depth 3.2 cm. This effectively represents a section through the centre plane of the brick. The domain was mapped using an uniform finite element mesh comprising 51 nodes and 12 quadratic serendipity elements, was used to represent the sample. A variable time step, based on initial, minimum and maximum time step size of 1sec, 0.001sec and 9 hr respectively, was employed for the simulation. The above mentioned spatial and temporal discretisations were applied after a thorough investigation to obtain a converged solution. The short sides and bottom were treated as being insulated and impermeable and therefore the heat transfer and drying process takes place at the top exposed surface only. For this purpose, heat and mass transfer by convection is assumed to take place captured by the heat and mass transfer coefficients of h_T= 5 W/m^2/K and h_m = 0.0086 ms^{-1} and a reference temperature of 75°C and an ambient relative humidity

of 50% respectively. These are compatible with drying within a slow airflow environment and these may be derived from a number of sources in the literature, such as (Ilic and Turner, 1989; Ben Nasrallah and Perre, 1988) and (Zhang, 1999). This enables validation against the work by Stanish *et. al* (1986). The relevant material properties are presented in Table A1 (in Appendix 1) and transport related equations such as permeability, saturation curve, including all flow phases and solid properties are defined as presented in Chapter 3. The matrix is assumed to be saturated uniformly at 60% at the commencement of the drying process as defined by the benchmark. This is similar to other related work on concrete and brick (Baroghel-Bouny *et al.*, 1999; Kallel *et al.*, 1993; Zhang, 1999).

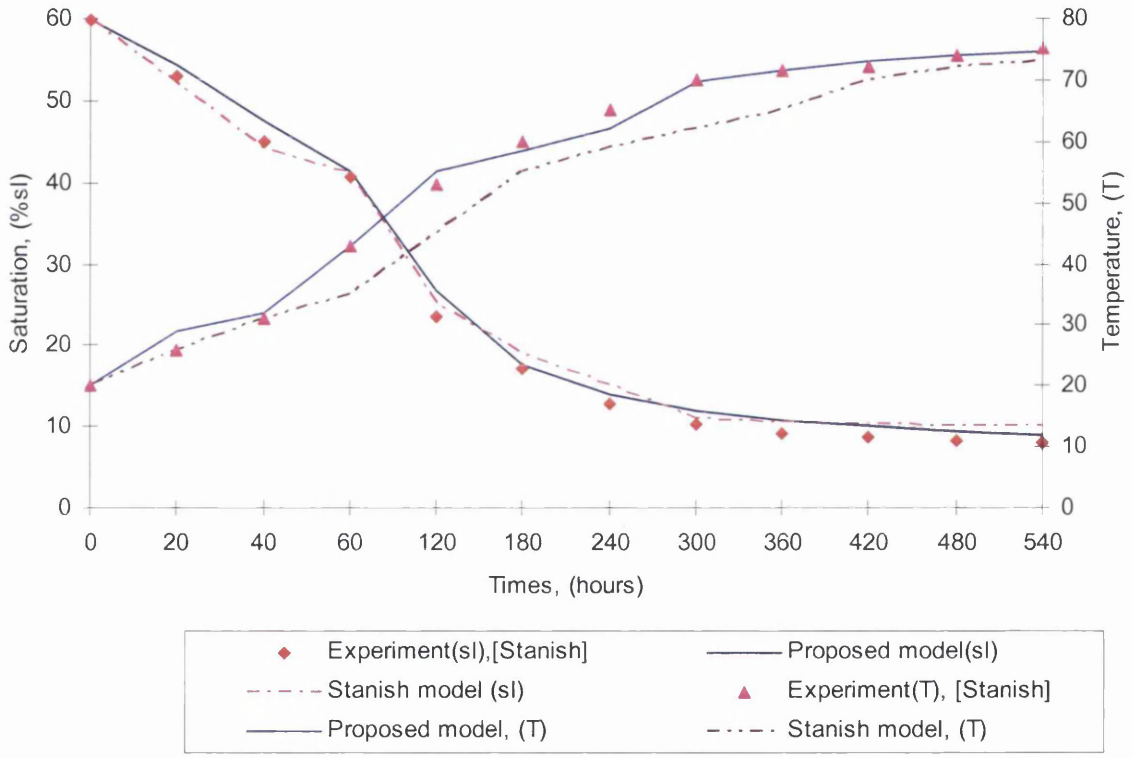

Figure 6.6: Liquid saturation and temperature changing over the drying time.

Comparison between the experimental data from the above related work (Stanish, *et al.*, 1986) and the simulation results for brick drying at 75°C are shown in Figure 6.6, in which moisture and temperature at the mid height of the brick are depicted over time. The temperature prediction coincides with a thermocouple positioned in the brick, whereas the moisture level at the centre is assumed to approximate the average value in the brick, reflecting the trend in gravimetric loss as captured in the

experiment.

The result shows that the moisture drops quickly at the beginning, corresponding to the constant drying rate period. At this point, the internal moisture transfers to the surface nearly as rapidly as it evaporates from the surface. During this stage the movement of liquid is maintained by the capillary action and the surface experiences a film of free water that evaporates steadily and continuously, and thus the drying rate is determined by the rates of external heat and mass transfer. Under these conditions, the temperature gradient is low and consequently the diffusion mechanism that is determined by the temperature gradient is small. Over the drying duration, the saturation level decreases and at nearly 60-70 minutes, it displays the characteristics of a falling rate period where there is a reduction in the rate of moisture loss. Theoretically, the saturation level will recede continuously into the interior of the material and the dry zone will extend gradually. Normally this corresponds to a critical saturation at about 0.3 for most porous material (de Vries, 1958.; Zhang, 1999). This shows the start of the falling rate period. During this period the drying process will slow down and it is now controlled by the water vapour movement. The same trend of the drying curve has been demonstrated by others researcher while validating their numerical models for drying (Ilic and Turner, 1989; Ben Nasrallah and Perre, 1988). In general, the proposed model shows a very good agreement. The moisture loss response is comparable with that predicted by Stanish *et al.* whereas superior agreement has been achieved for the thermal characteristic. This may due to the fact that, as explained in Chapter 4, the model proposed in this work takes into account the latent heat contribution which is not presented in the numerical work by Stansih *et al.* Clearly, this comparison with experimental data displayed in Figure 6.6 is very good, confirming the basis and quality of the simulation model that has been developed and applied in this case study.

Given this agreement with temperature evolution and moisture loss, it is appropriate to explore and illustrate the variation of other parameters and material properties during the drying process. This will be presented in the following paragraphs.

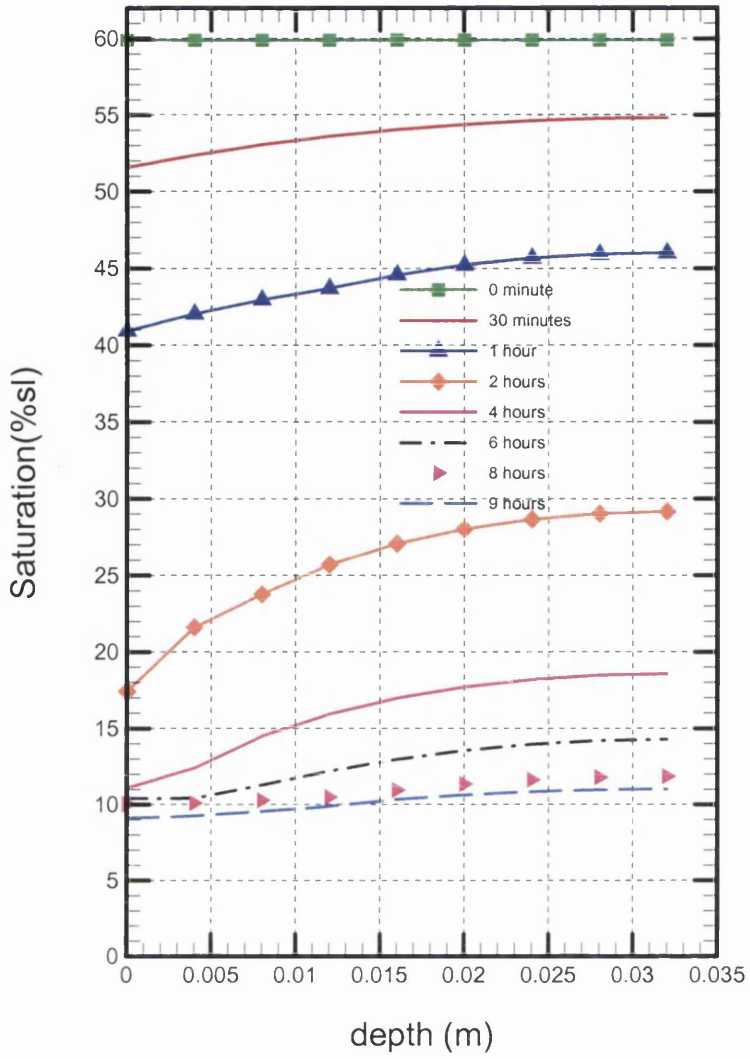

Figure 6.7: Saturation variation along the depth.

Figure 6.7, depicts the change in saturation over the brick depth at discrete times, showing the gradient through the depth and that the moisture content decreased slowly after the falling rate period. The same pattern for temperature is also exhibited in Figure 6.8, showing a small increment during the constant rate period, a big increment after falling rate period and finally stabilizing towards the ambient condition of 75°C. This is also reflected in the permeability properties in Figure 6.9, where the permeability change starts to show a small reduction when nearing hygroscopic saturation. Also, as can be seen from this figure, the permeability properties drop close to zero at the saturation value 0.09 (or 0.1).

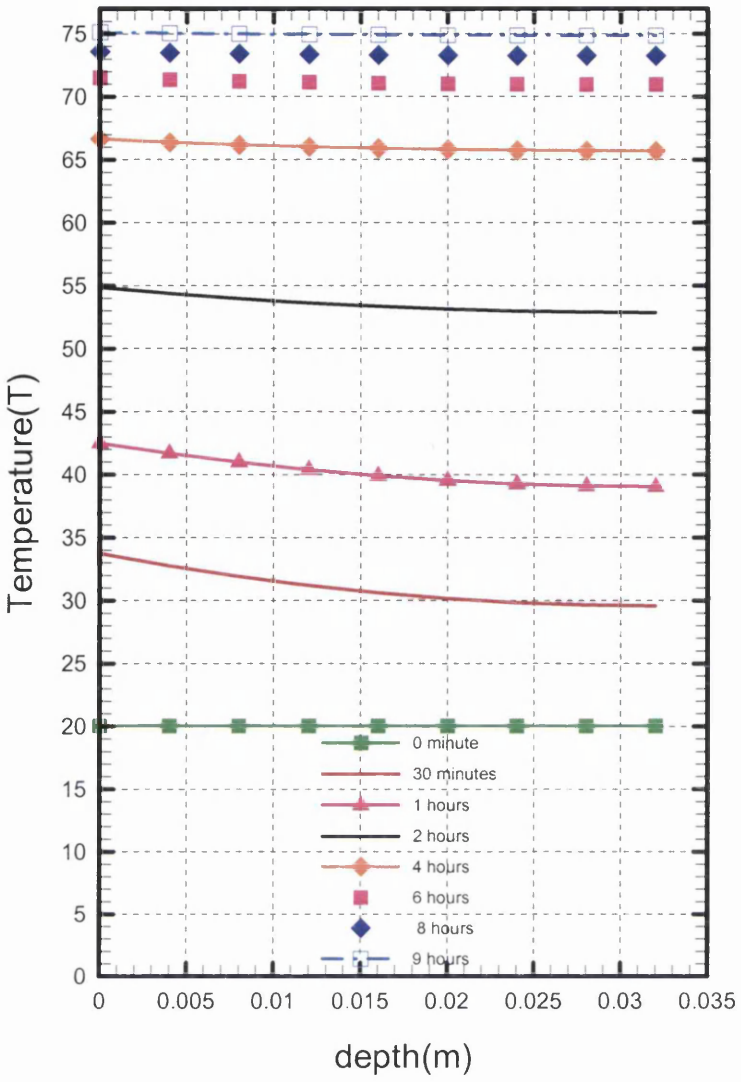

Figure 6.8: Temperature variation along the depth.

This is due to failure of liquid transport by capillary action and this is no longer possible below the irreducible saturation level (Ilic and Turner, 1989; Ben Nasrallah and Perre, 1988; Spolek *et al*, 1981; Tesoro, 1974). It has been found that the experimental detection of very low permeability is extremely difficult and it is generally taken as equal to zero in the drying process. Figure 6.9, also includes the variation of relative humidity within the porous matrix as a function of saturation. Above the critical saturation, the humidity remains close to a saturated humidity condition and below this value it showed the falling rate condition where the vapour transport mechanism plays an important role in changing the local humidity within the matrix. When near to the irreducible saturation level, the relative humidity just shows

a very small change, indicating the minimum water content to which the material can theoretically be dried under the non hygroscopic condition.

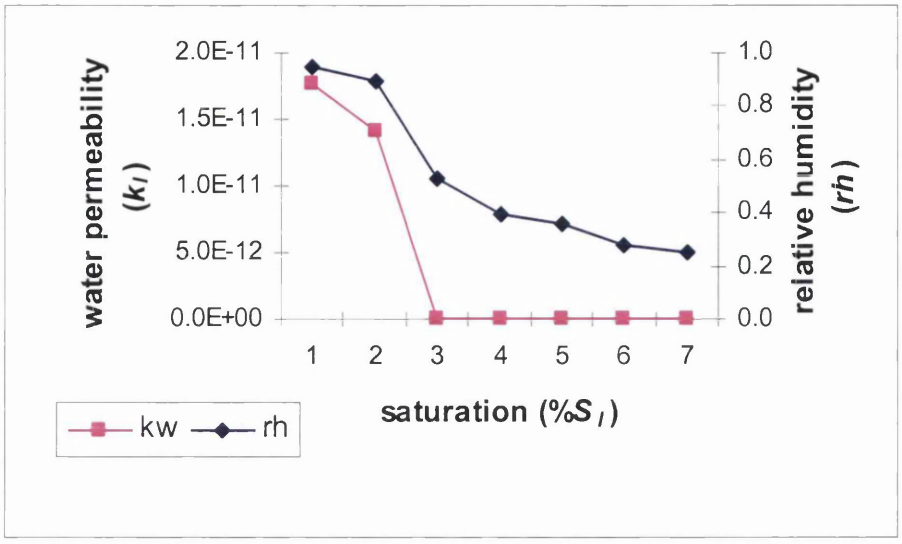

Figure 6.9: Permeability and relative humidity against saturation.

The gas pressure variation is presented in Figure 6.10. In the beginning, the moisture variation through the capillary body is assumed to be uniform and the gas pressure stays constant at the atmospheric level. As soon as the dry zone occurs, the temperature starts increasing, and consequently there is a rise in gas pressure. As the drying proceeds and approaches the falling rate period, the body temperature starts to increase more rapidly and this increases the gas pressure in the body. The pressure inside the sample increases to its maximum value whereas the pressure at the surface always stays at the atmospheric level, reflecting the boundary condition at this surface. This is shown clearly in Figure 6.10. A large increment in gas pressure is shown during the falling rate drying period. However, when the body approaches irreducible saturation and is therefore nearly fully dried, the temperature increment also reduces, settling at the ambient condition after sufficient duration of 6 hours drying time. This is also reflected in the gas pressure which now decays towards the atmospheric condition as the drying process is allowed to continue for a long time. The same kind of evolution in gas pressure during convective drying has been presented in several other works, such as in brick drying (Ben Nasrallah and Perre, 1988), in consolidating a slab of porous material (Ilic and Turner, 1989), in drying of a concrete wall (Gawin and Schrefler, 1996) and in drying of light concrete (Tai

Hong, 2006).

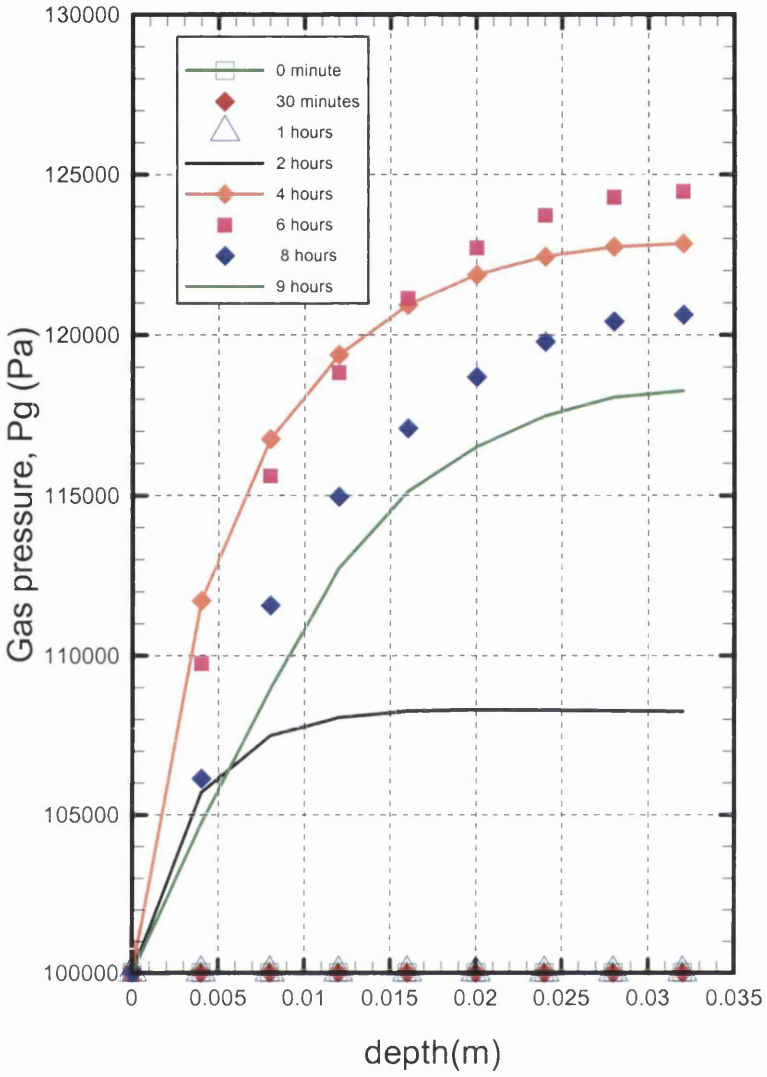

Figure 6.10: Gas pressure variation with different time along the depth.

Pore water pressure evolution is shown in Figure 6.11. At the beginning, the pore water pressure remains at a nearly constant condition. This drying regime indicates a free water movement at nearly atmospheric ambient pressure. The same trends of change in the pore water pressure are clearly shown in the falling rate period where a big decrement is recorded as drying proceeds within this range This shows the condition when water recedes into the inner of the body and the capillary action is slowly diminished as water is strongly bonded to the porous matrix. Reduction of capillary action in the porous body is accompanied by a gas pressure that is higher at the outer surface. This restricts moisture transport that is achieved through convection by the gas phase. As drying proceeds towards the irreducible value, the pore water

pressure decrement start to slow down indicating that the body is in a nearly fully dry state. In general the range of computed values for the pore water pressure that is presented in Figure 6.11 is high. However, it is appropriate for the suction curve for concrete and cement paste that has been assigned in this case (Baroghel-Bouny, *et al*,1999). Some further case studies (as presented in Appendix 2) based on different material property values has been carried out to determine response sensitivity of this parameter to the measured variables or to the final computed value. Based on the comparison with the benchmark case study as presented in this section, it can be concluded that all the results are appropriate to describe the drying process according to the selected material properties.

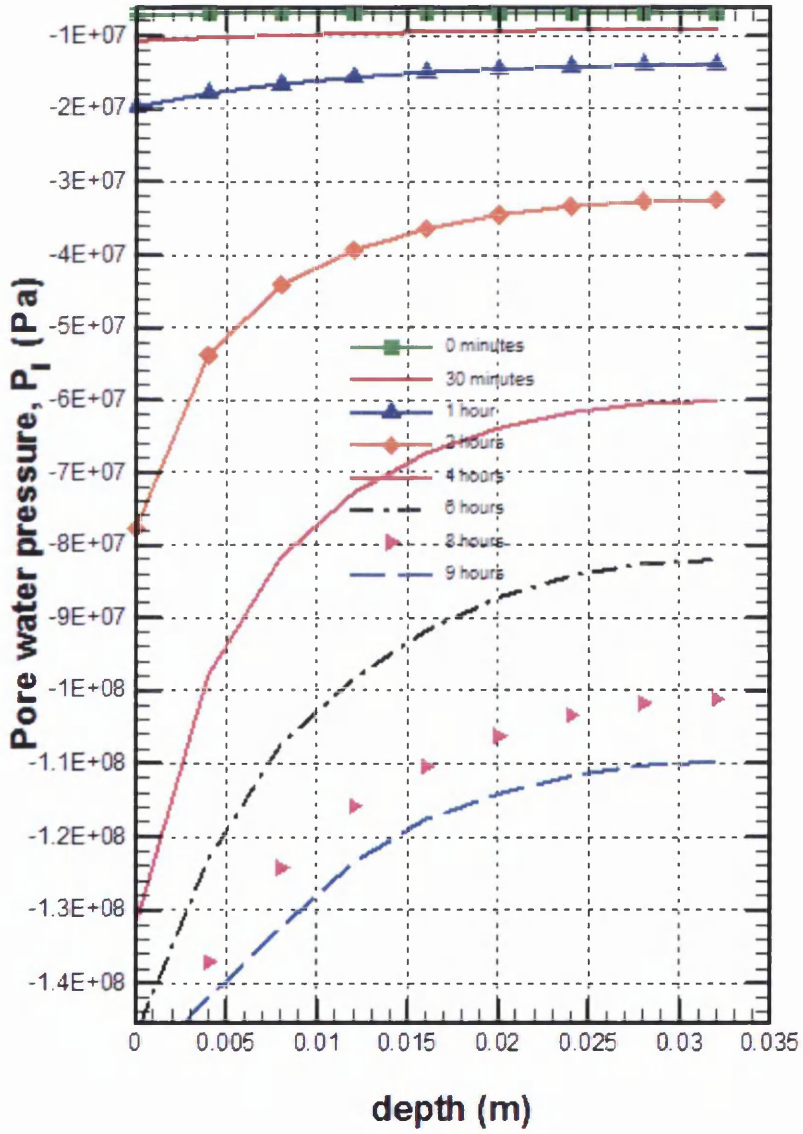

Figure 6.11: Pore water pressure variation with different time along the depth.

6.4 Shell drying on a simple linear section

Based on the validation case studies described above, the simulation was extended to address the drying of a ceramic that forms the shell for the investment casting process. This work includes single and multilayer systems and incorporates simple linear and corner geometries that are generic to a range of investment cast parts. Where possible, results will be compared with experimental data. Principally this will be drawn from the work described by Leyland and Jones (11-14 September 1995)

In general, there are differences between the drying response of a ceramic shell mould and a brick. As explained and elaborated in the works by Leyland and Jones, drying of the ceramic shell mould is presented by the drying curve of a sol-gel mixture. This can be seen in Figure 6.12 where water loss from the first coat is quite high at the beginning of the drying process. In this case, a coat comprises the slurry and ceramic particulate that forms the layer thickness. Thus, the slurry and the ceramic that forms the shell have a high water content within the porous network. This is not the case for brick or concrete. Therefore most of the sol-gel ceramic type compositions have a very steep drying curve at the beginning (Briscoe *et al.*, 1998). As explained in the previous section, brick drying involves two stages that correspond to constant and falling rate periods. The same drying stages are inherited for the ceramic shell coat that has also been described in previous work (Hyde, October 1995) and (Pierre, 1990). Therefore, in this section, validation of simulation will be based on trends rather than precise values. This is due principally to the difficulty in obtaining precise data and characteristics to describe the drying behaviour for the coating materials in a form comparable to that set out in Chapter 3 and that is appropriate for incorporation into simulation.

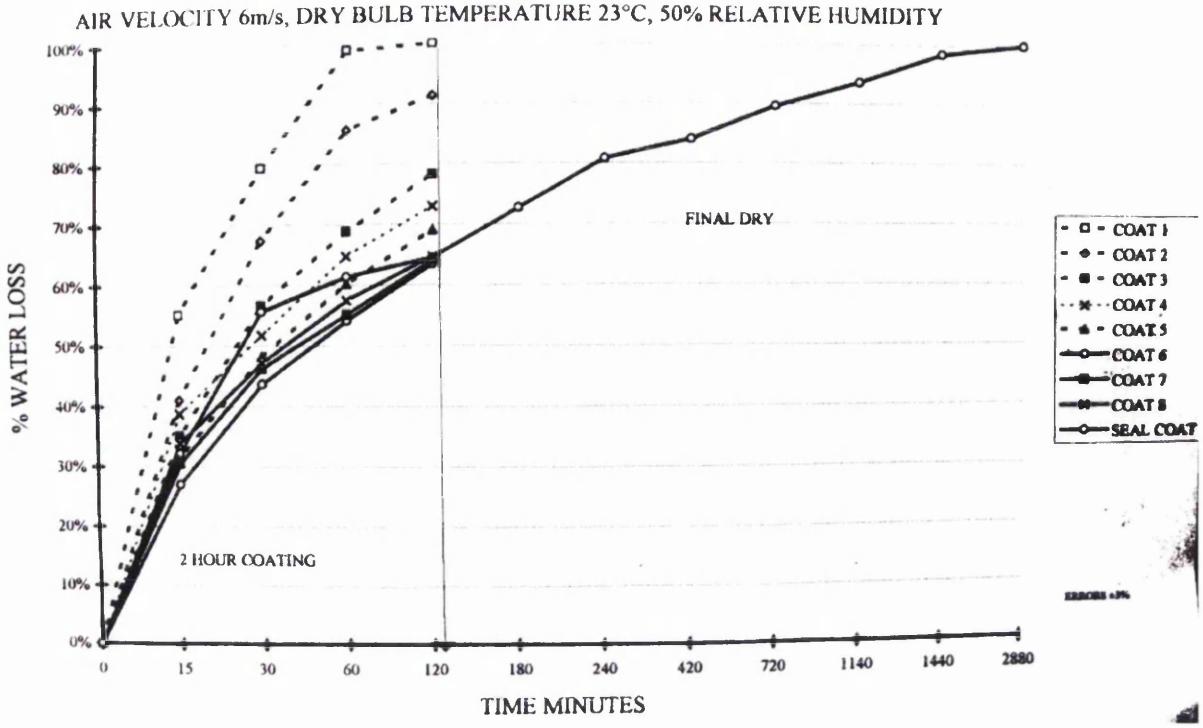

Figure 6.12: Percentage of moisture loss at different time (Leyland and Jones, 11-14 September 1995).

In this work, numerical experiments have been conducted on simple linear geometries under closely defined boundary conditions that represent the drying atmosphere commonly implemented in a shell drying facility. Both single layer and multilayer shells are simulated and presented within this section. Comparison between the experimental data on shell build up (denoted as coats in Figure 6.12) and the simulated results are given. Most comparisons are based on the moisture loss measurement as presented in the works by Leyland and Jones. This has been done to facilitate validation of the scheme. Also because shell drying occurs slowly under near isothermal conditions there will be little contribution from temperature and hence gas pressure effects. The material properties that have been assumed are given in Table 1 (in Chapter 3) and the liquid and gas permeability, vapour diffusivity, ceramic porous conductivity and other related data have been presented and discussed in Chapter 3. Based on the information from industry, most shell drying is achieved by controlling relative humidity with air velocity and a nearly constant temperature. Therefore, the simulation has been conducted with regard to the above conditions for both single layer and multilayer shells.

6.4.1 Single layer case study

This section focuses on the drying of a single layer of the ceramic shell mould. The simulation was carried out on a simple linear section as described in Figure 6.13 below. The body was assumed to have high initial water content and can be considered to be nearly fully saturated. The boundary condition for drying is applied at the side that contains nodes 3, 26 and 2. The remaining sides are assumed insulated and to be impermeable. This reflects the zero gradient that is appropriate for a section through a long straight shell section and the condition that applies at the wax surface corresponding to nodes 1, 52 and 4. All other parameters such as temperature (at 23°C), gas pressure (1 bar) are assumed constant throughout the body. The heat and mass transfer coefficient values which are 2 W/m^2K and 0.001 ms^{-1} along with the ambient relative humidity of 50% and temperature at 23°C are used as the best approximation in describing the slow and controlled drying process. The domain is mapped using a uniform finite element mesh comprising 53 nodes and 10 quadratic serendipity elements applied to a layer thickness of 1 mm. A variable time step, based on initial, minimum and maximum time step size of 1sec, 0.001sec and 2 hours respectively, was employed for the simulation. The above mentioned spatial and temporal discretisations, similar to those in the previous section are considered appropriate for this case study.

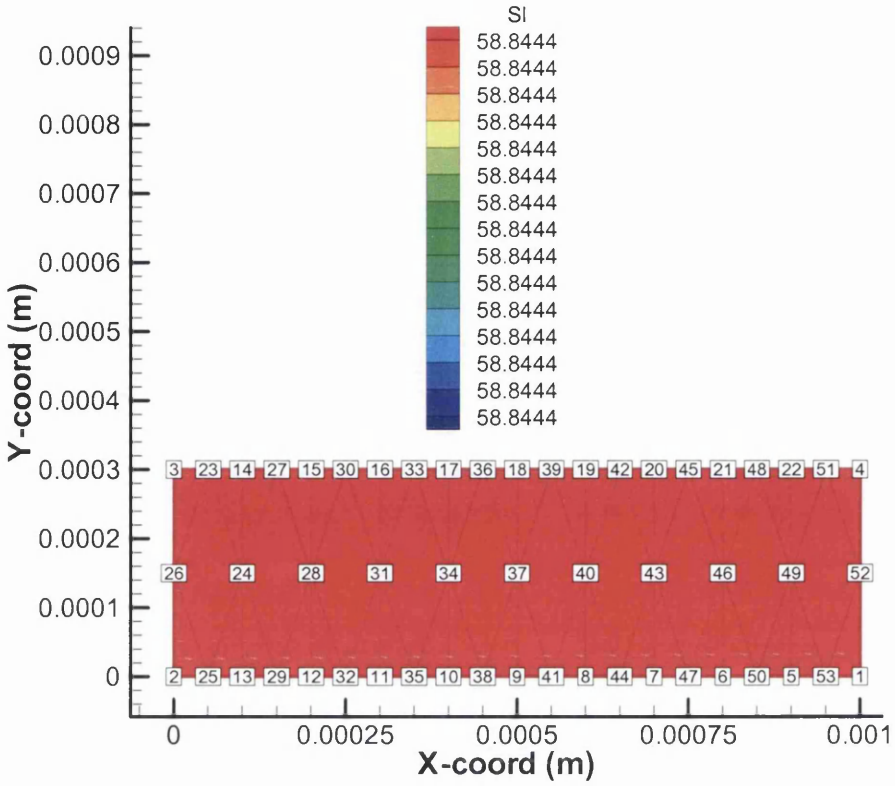

Figure 6.13: Schematic of the single layer problem.

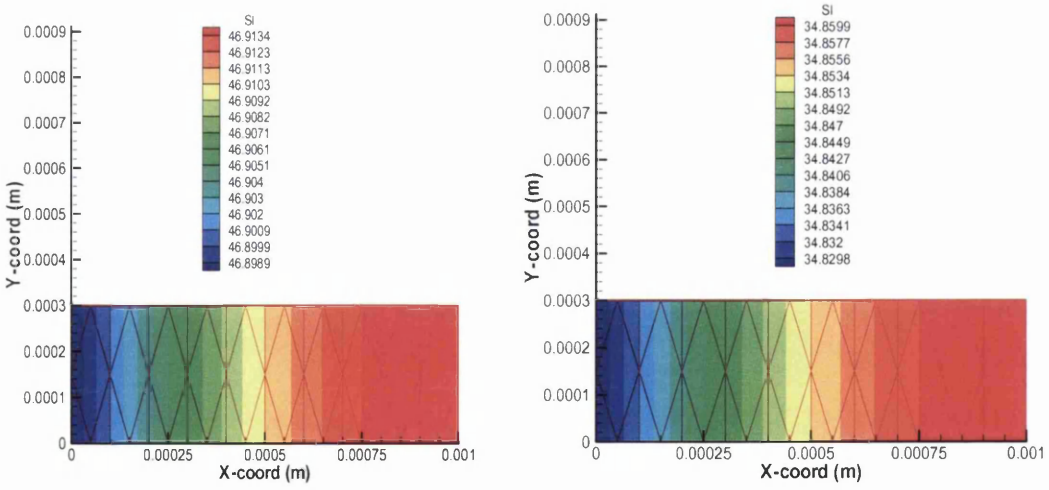

(a) (b)

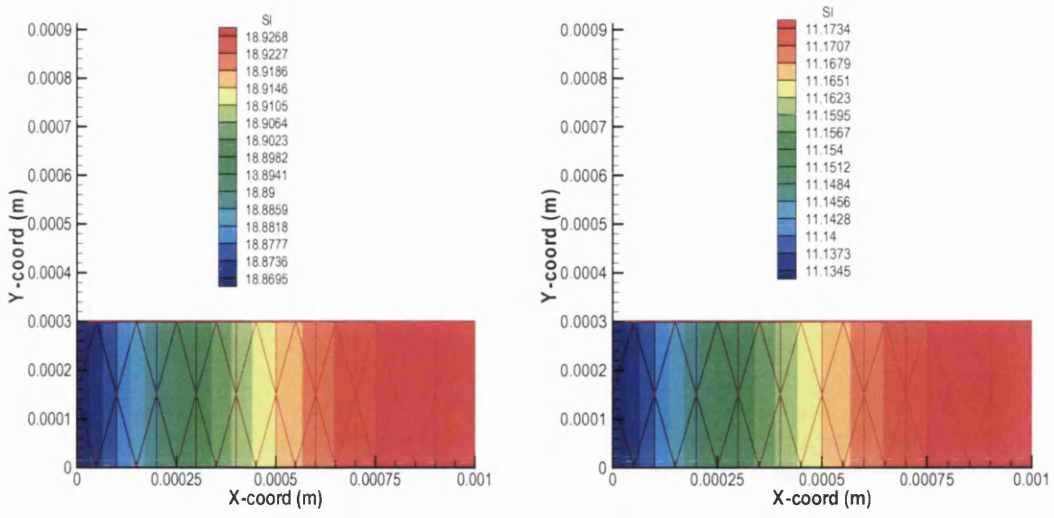

(c) (d)

Figure 6.14: Saturation at 15 minutes (a), 30 minutes (b), 1 hour (c) and 2 hours (d) of the drying times.

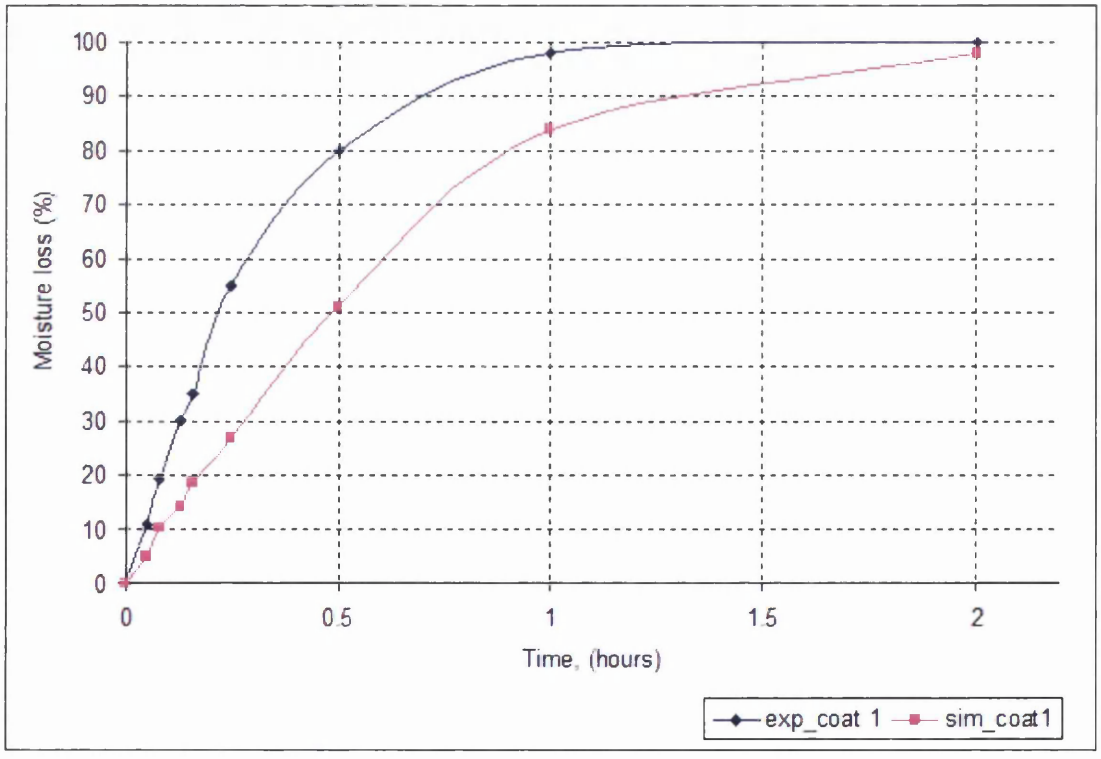

Figure 6.15: Percentage of moisture loss at different time for the single layer case study.

The results for saturation and moisture loss are presented in Figures 6.14 and 6.15. In the latter, moisture loss represents the progression of water loss that has been derived from an average of the moisture content within the sample. The moisture loss may be obtained from the saturation data predicted by the simulation. This is given by the expression below;

$$\text{Percentage moisture loss} = \left(\frac{59\ \% - y\ \%}{59} \right) x 100\ \% \qquad (6.6)$$

where the value of 59 % indicates saturated percentage of the new dipped layer and y % is saturation level that remains in the body after it has gone through the drying process.

This trend reflects the gravimetric measure that captures a global water loss, rather than a local value as depicted in the contours in Figure 6.14. The results show that the saturation starts to reduce as drying proceeds. At the beginning of drying a high percentage of moisture loss is presented in both of the curves in Figure 6.15. This illustrates the trend from the constant rate drying period and indicates the high free water content that is present in the single layer. The simulated curve showed a big deviation from the experiment over the early stages of drying. This has been attributed to the ceramic shell properties that have been used in the proposed model, such as the saturation curve that has been demonstrated to be appropriate for the brick material (no equivalent curve has been found for the ceramic shell material). Data from the experiments also show that within 20 minutes, drying nearly achieves the critical saturation (0.3) that corresponds to a 70% moisture loss. The simulated curve achieves the critical saturation after about 45 minutes. As drying continues beyond this critical value, the difference between experiment and simulation falls progressively to a very small value near to the irreducible level after 2 hours. Both plots show the same pattern of moisture reduction and so it is assumed that the proposed model can be used to simulate drying of ceramic shell layers and therefore it will be used to explore a multilayer system.

6.4.2 Multilayer study

As described in Chapter 1, the multilayer ceramic shell build up process involves the dipping and the drying process for every layer that makes up the ceramic shell body. Consequently, there is an impact on the drying behaviour due to the slurry soak back throughout the previously dried layer(s) during each coating cycle (Jones, 1995). This is clearly described and shown in Figure 6.12 above, where for every layer there is a slightly different percentage water loss. This directly influences the drying time as the thickness of the shell increases during the layering process. In the work by Leyland and Jones (11-14 September 1995) three variations of intercoat time were explored (30 minutes, 1 hour and 2 hours) from which it was found that 2 hours intercoat drying time gave the shortest total drying time for the whole shell system. This is the result depicted in Figure 6.12 and this will be used to explore the multilayer drying simulation capability. Therefore in this set of numerical experiments, a two hour coating cycle time was chosen. Experimentally, the weight loss data took into account the water contained in the slurry calculated from the total solids content, slurry soak back into the previous coats during dipping and water that is not removed from the inter coating layers (Leyland and Jones, 11-14 September 1995).

In this work there are several options that may be explored in modelling drying of the multilayer shell. This is due to the fact that the layered domain is not as simple as a single layer model (where the domain may be assumed to be homogenous). In a precise simulation, the process of shell build up as explained in Chapter 1 should be emulated. This comprises dipping and soak back, addition of a zircon layer by sprinkling powder over the wet surface to build a layer of about 1mm thickness, wetting of this sprinkled powder and then drying of the layer that is added as well as re-drying of previously dried layer(s). If simulation is to capture layer addition, a dynamic meshing strategy to capture the addition of the sprinkled layer will be required. There are also further physical difficulties such as the need for a wetting model to capture the redistribution of water from the slurry into this freshly added layer. Because of these difficulties two simpler approaches were explored in an attempt to establish their ability to capture the drying of the multilayer system.

The **First approach** describes the multilayer stage by simulating a single layer, and then adding a second wet layer with a different percentage water content that reflects a homogenisation of the added slurry and zircon powder that makes up that layer. The drying period is then simulated and the final results are averaged over the shell thickness that has been built up. A third layer is then added to the averaged data for the first two and the drying simulation carried out. This process is then repeated for as many layers as required. The **Second approach** describes the multilayer by assigning a moisture gradient through the layers, as derived from experimental observation. Unlike the first approach, this requires some knowledge of the moisture gradient and therefore it is not a strictly 'ab initio' simulation approach.

Besides the factors that have been mentioned in the above paragraphs, numerical problems will arise at the sharp discontinuity introduced by the low to high saturation as a fresh layer is added. This can be accommodated by having a finer mesh. In this work, one example multilayer case study will be simulated using two different meshes to explore mesh sensitivity issues related to the sharp discontinuity that exists at the interfaces between existing and new layers. The results are presented in Section 6.4.2.3 shows a mesh with 20 elements which is double that for the case study 6.4.2.1. For the finer mesh the interface area that has been defined is quite narrow compared with Figure 6.16 (or Figure 6.32(b)). The simulated results for every node in the two meshes do not show a big difference (less than 1 %) which is acceptable for most numerical solutions. Therefore throughout the next case studies, all the domains are mapped using the coarse mesh.

6.4.2.1 Case study for the First Approach

This section can be considered as an analysis of drying of a ceramic shell mould effectively comprising two layers. The procedure for the simulation has been described in the above section. In defining the initial condition, coupled with a relatively coarse mesh, a gradient is prescribed between the two layers. As well as avoiding the introduction of a discontinuity at the interface, this also reflects the soak back mechanism that occurs during the dipping process.

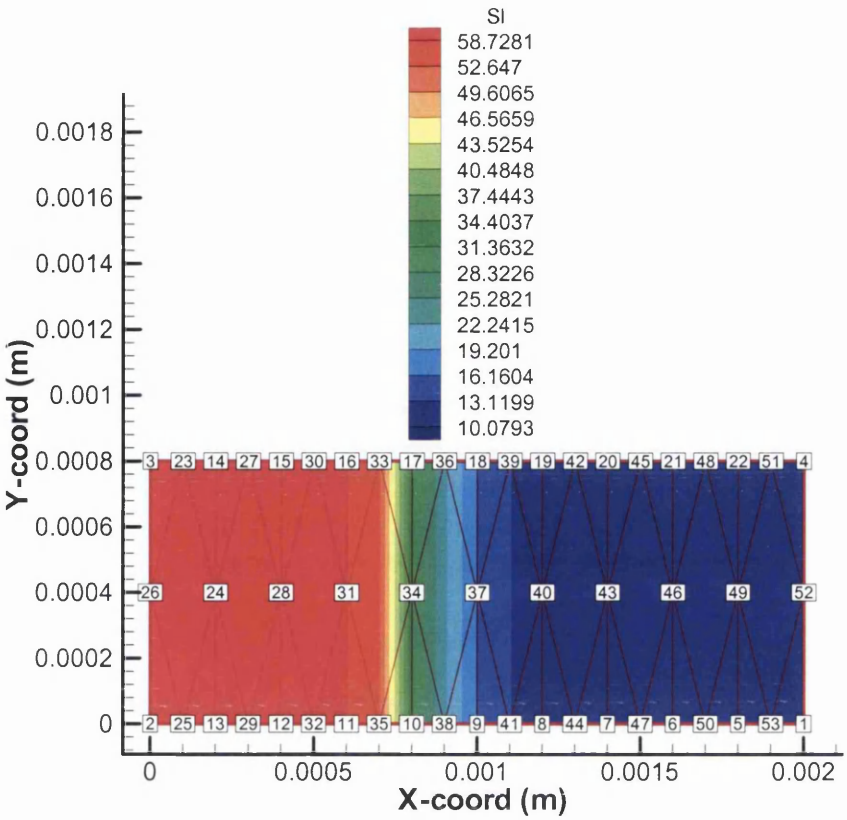

Figure 6.16: Schematic of two layers of the shell showing the initial condition and including the selected nodes 1, 9 and 2.

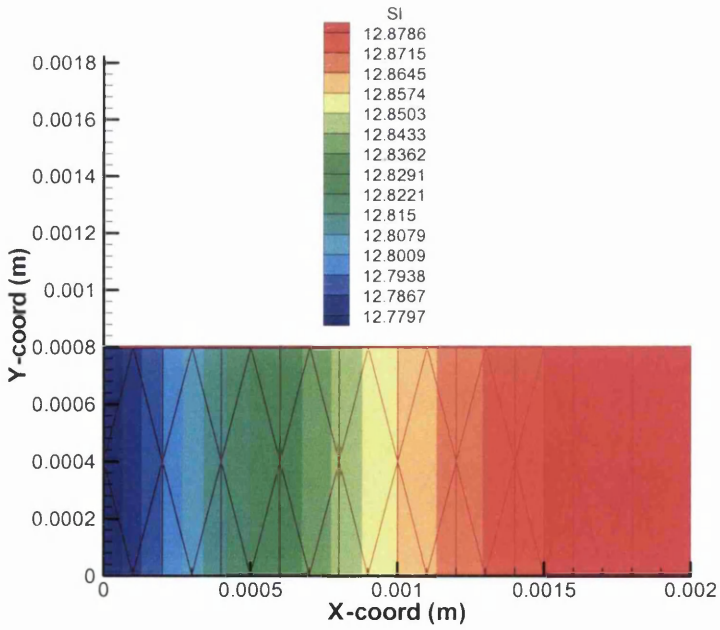

Figure 6.17: Saturation contour at 2 hours drying time.

The simulation was carried out on the simple linear section as shown in Figure 6.16 above. The same domain mesh which comprises 51 nodes and 12 quadratic serendipity elements but with different thickness to represent the build up of the shell was used in all of the analyses, the results from which will be set out in the figures below. The variable time step, based on initial, minimum and maximum time step size of 1sec, 0.001sec and 2 hr for every layer. The exception is the last layer; layer 9 for which the maximum time step of 48 hours has been implemented. All the figures that will be described below and in Appendix 3 show the simulated results with their selected nodes that are appropriate to describe the transience of moisture gradient throughout the multilayer system especially at the beginning of the drying process and in the later stage.

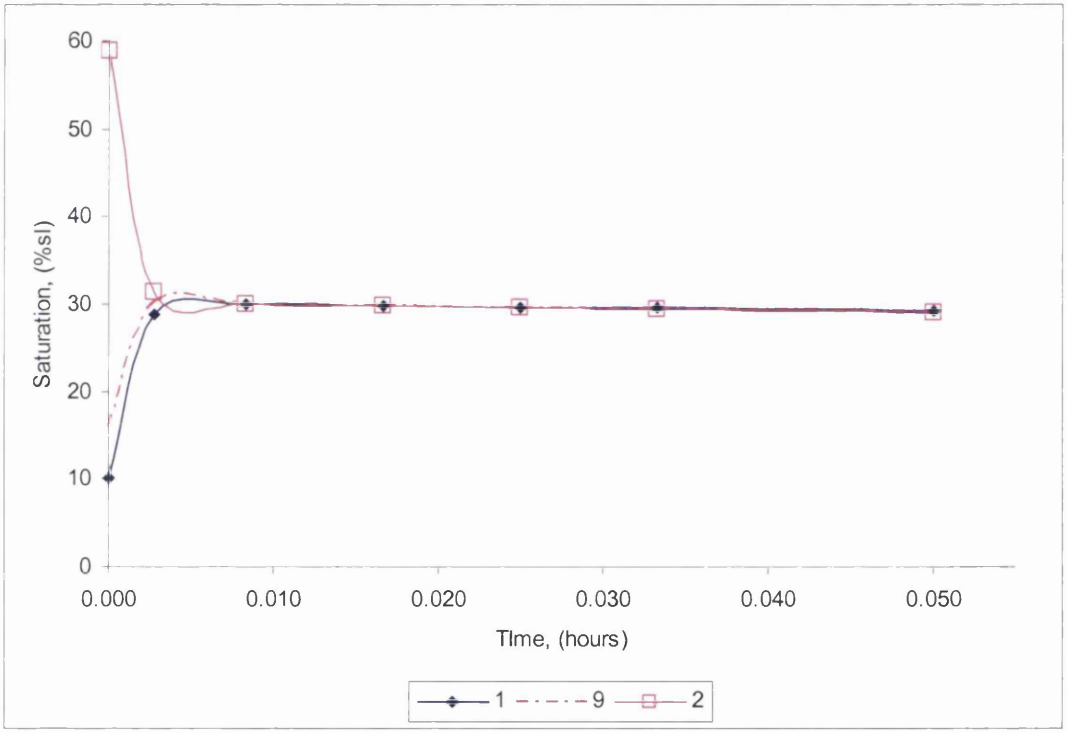

Figure 6.18: Saturation level of coat 2 at the selected nodes over a 3 minutes drying duration.

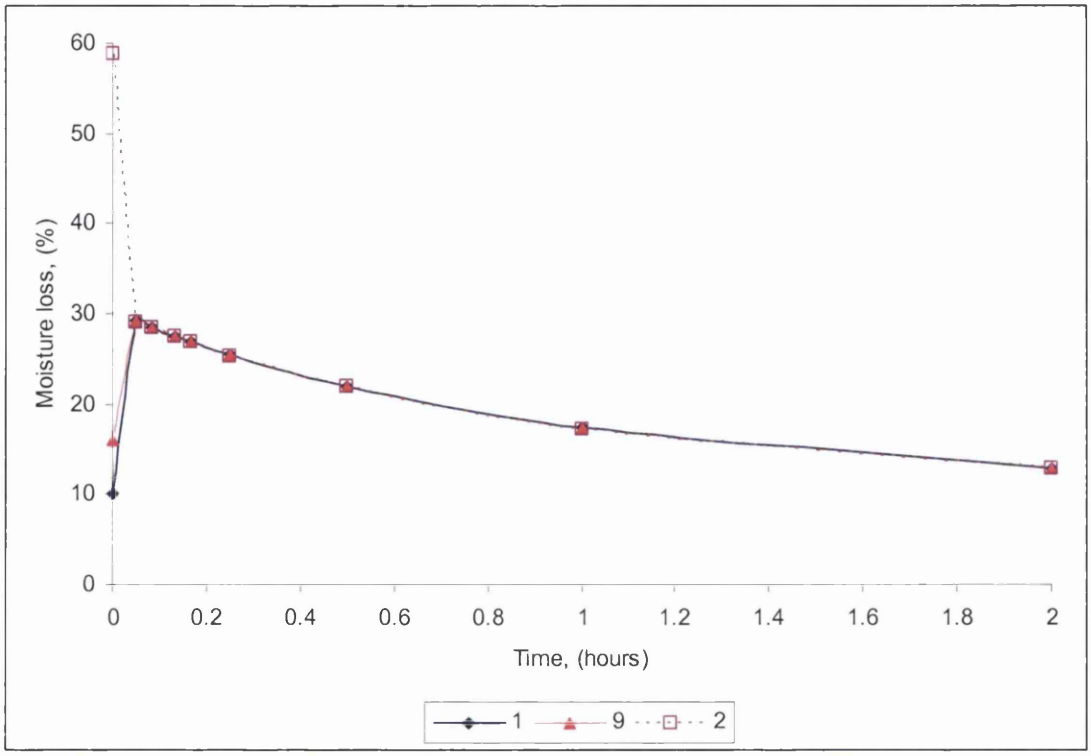

Figure 6.19: Saturation level of coat 2 at the selected nodes over a 2 hour drying duration.

Figures 6.16 to 6.19 show the initial condition and simulated results for the first two layers system in modelling of the drying ceramic shell build up process. At the beginning of the drying in Figure 6.17 there is a balancing or transition that shows movement of the moisture content from the wet layer to the inner dried layer within 1 minute. This penetration of moisture to the inner layer is also strongly influenced by the properties that initially exist within the previously dried inner layer(s). This still indicates that the process occurred in the presence of free water. As the initial transient is finished, then the moisture gradient starts to decrease and the moisture distribution across the domain levels out. The complete contour evolution of the moisture transition are given in Appendix 3.

To continue this simulation the excess moisture from the previous layer is assigned as the initial condition for the next dried layer after that. Therefore, modelling this simulation case study does not need an initial experiment for each layer derived from experiment. Figure 6.20 shows the initial condition for a three layer system where the excess moisture in the dried layer is equal to a saturation level of 12 % (which is the

excess moisture that is present in the combined first and second layers after two hours drying time).

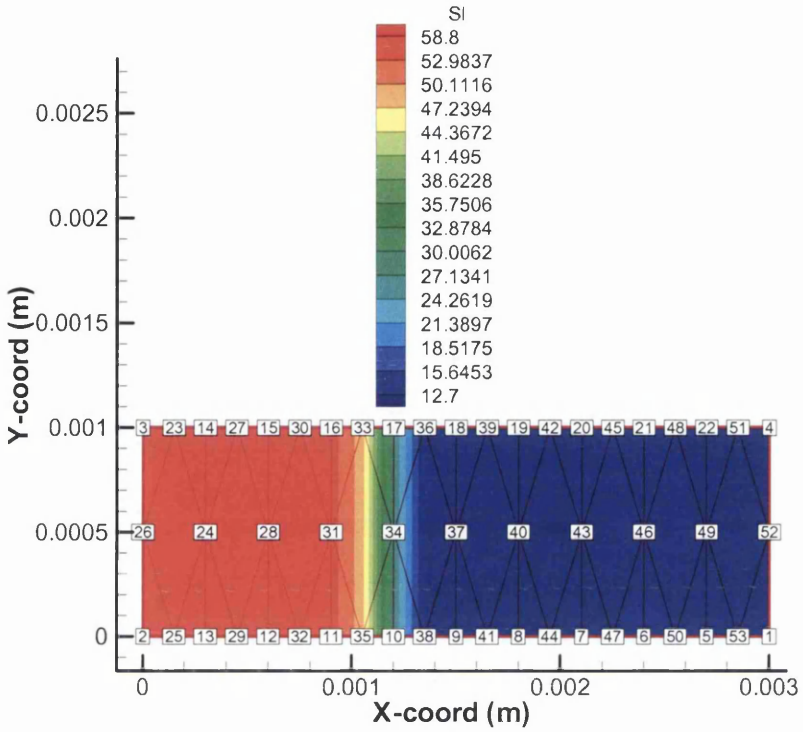

Figure 6.20: Schematic of three layers of the shell coat.

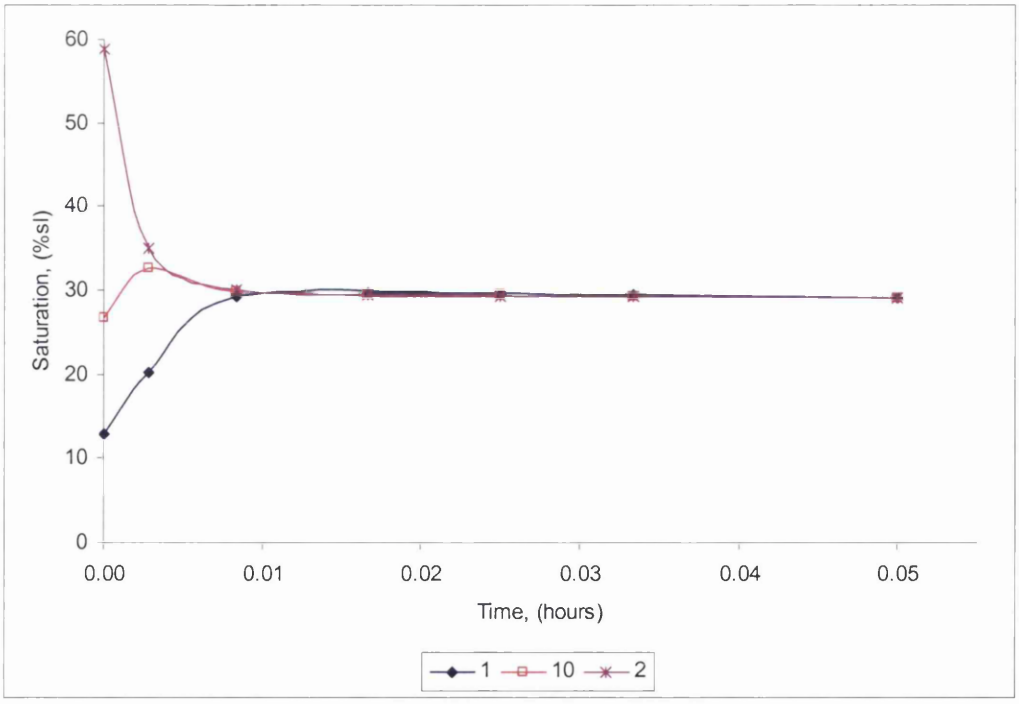

Figure 6.21: Saturation level of coat 3 at the selected nodes over a 3 minutes drying duration.

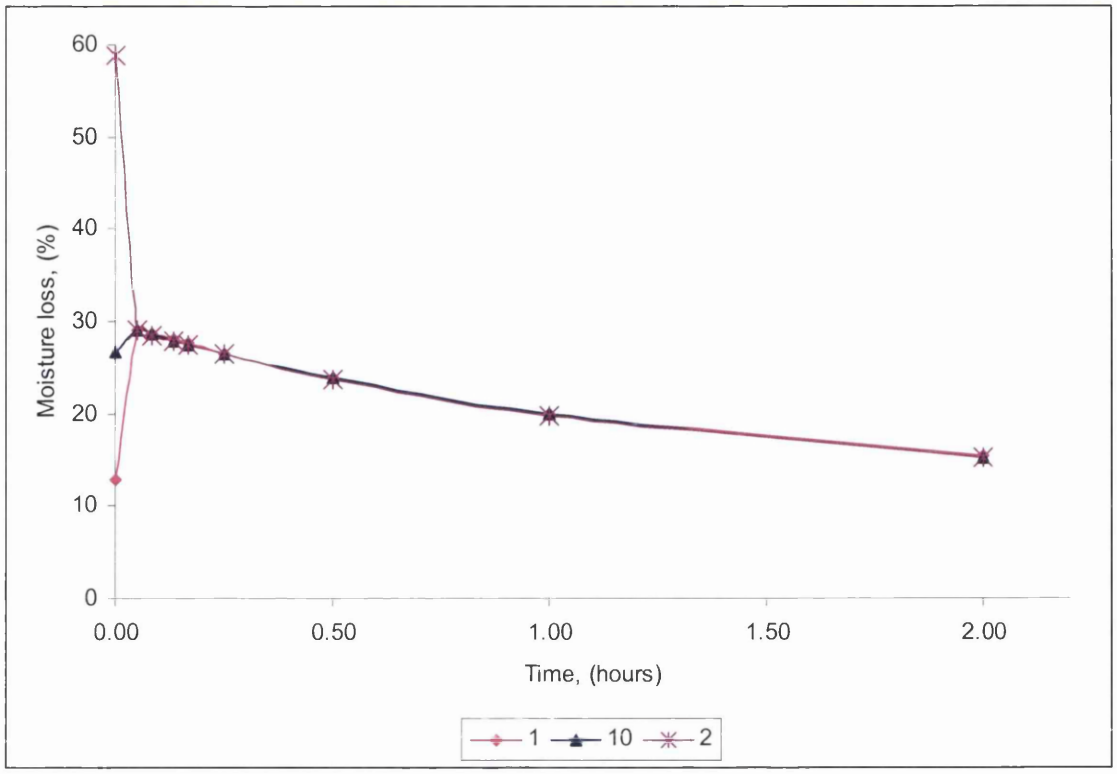

Figure 6.22: Saturation level of coat 3 at the selected nodes over a 2 hours drying duration.

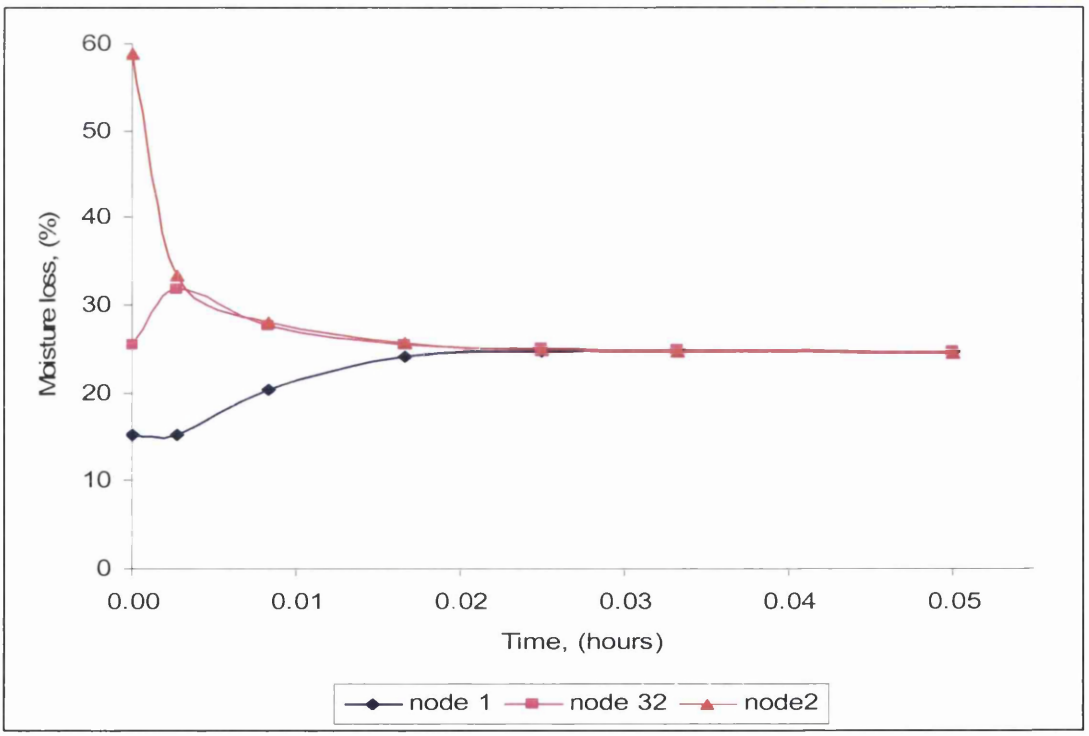

Figure 6.23: Saturation level of coat 4 at the selected nodes over a 3 minutes drying duration.

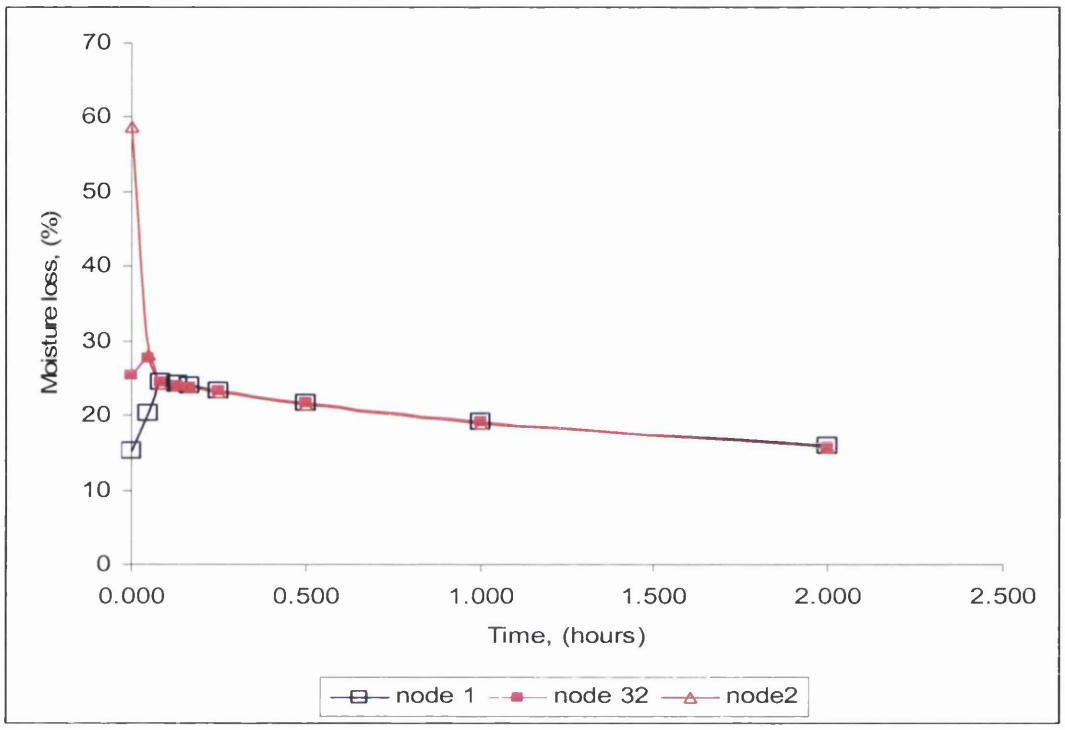

Figure 6.24: Saturation level of coat 4 at the selected nodes over a 2 hours drying duration.

The same condition is exhibited in the case of the three and four layer systems as described in the previous two layers system, where again results show the transition in moisture constant takes place over the early stages. These are shown in Figure 6.21 and Figure 6.23. In general there is only a slightly difference in the moisture change as each layer is added. As can be seen from Figure 6.18, 6.21 and Figure 6.23, the water penetration (which reflects also the water soak back mechanism) take a longer time as layers are added and the thickness of dried layer increase. This shows the effect of thickness build up as layers are added and the effect of previous layers that have an increasing excess moisture content due to the soak back mechanism.

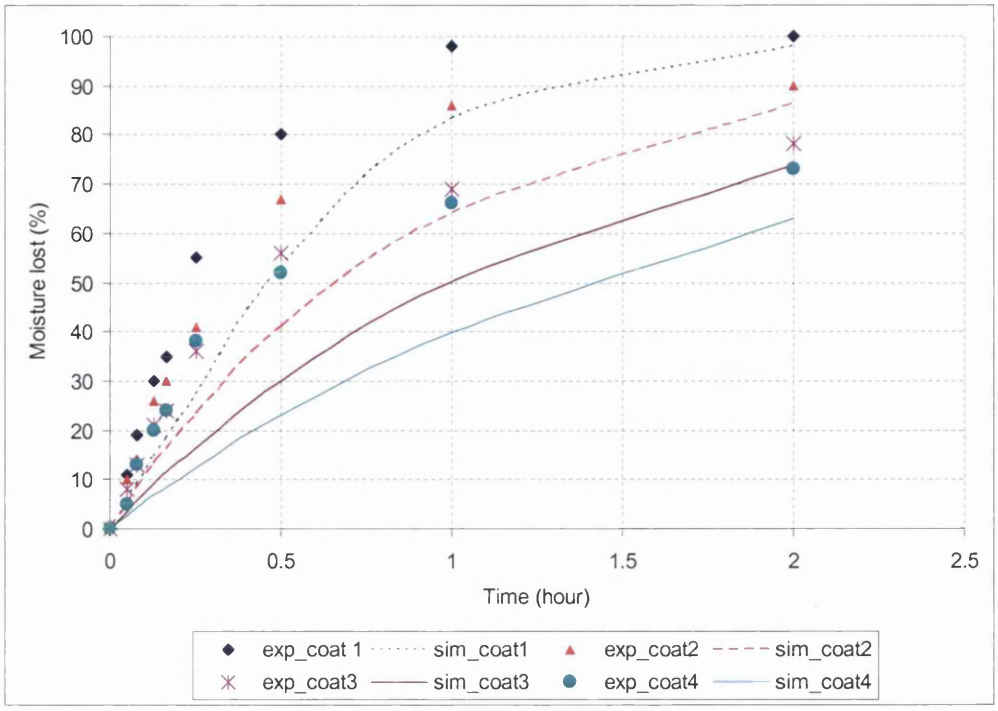

Figure 6.25: Comparison between the simulated result of layer 1, layer 2, layer 3 and layer 4, and the experiment data within 2 hours drying time.

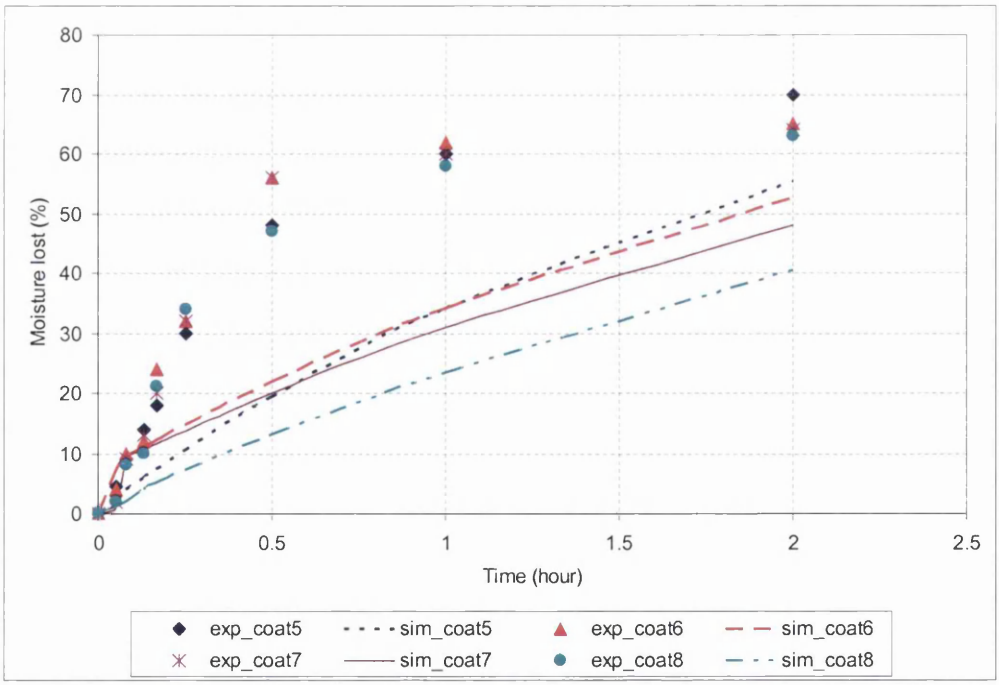

Figure 6.26: Comparison between the simulated result of layer 5, layer 6, layer 7 and layer 8, and the experiment data within 2 hours drying time.

A comparison of all the simulated results for layer 1, layer 2, layer 3 and layer 4 are

presented in Figure 6.25, and for the next four layers are given in Figure 6.26 and lastly the result for layer 9 is given in Figure 6.27. Figure 6.25 shows quite a good trend agreement between the simulated water losses distribution and the real experiment. The difference may be attributed to a number of reasons, that include material model definition and boundary conditions. All of the experimental responses are more rapid than the simulation that implies that either the mass transfer coefficient at the exterior surface is too low or that the material model parameters that control transport (permeability and saturation curve) are not appropriate, even though the latter must be matched. Further work is required to establish material model data that is appropriate for investment casting shell materials.

Figure 6.26 illustrates the condition of drying for layers 5 to 8. Again data from the experiments show that the remaining water in the shell layers from layers 5 to 8 does not achieve the critical saturation, which indicates that the matrix is still wet. This agrees with the related published experimental works (Leyland and Jones, 11-14 September 1995) where the water removed in each coat and the soak back into the previous coat becomes relatively constant after coat 4 and achieves about 60 to 50% saturation. This indicates that the previous layers have a build up in moisture content and that the intercoat duration is not sufficient. The same patterns of simulated moisture losses are presented in Figure 6.26 and which is similar in pattern to the experiment data. In general the moisture loss follows the same trend as the experimental data, showing the highest water loss in the first layer and increasing drying duration as further coats are added to the shell.

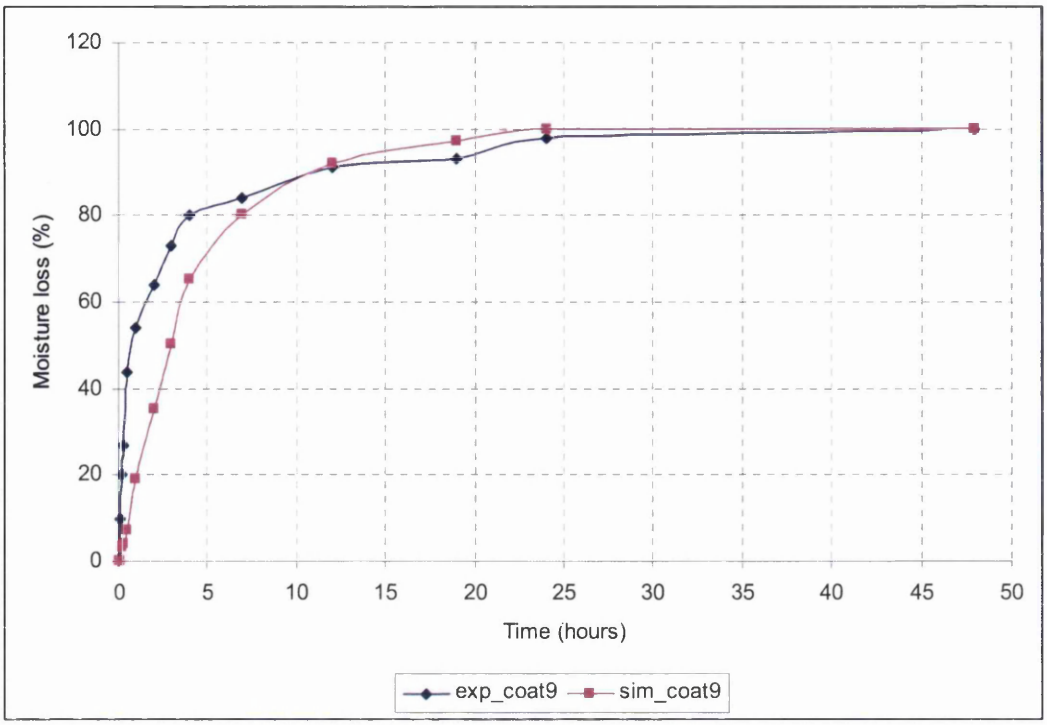

Figure 6.27: Comparison between the simulated results of layer 9 for two difference calculations within 2 days drying time of the first approach.

Simulation of the layer 9 (the seal coat) for the longer period of drying in Figure 6.27 show that the results are quite close as been used to represent the result in Figure 6.25 and Figure 6.26. Finally after 25 hours the simulated plot shows 100 % of water removal. In general the moisture loss follows the same trend as the experimental data, showing the lower reduction in the latter stage and finally approaching to the 100% moisture loss, as measured in the lab based work after 2 days drying period.

6.4.2.2 Case study of the Second Approach

This section can be considered as an analysis of the drying of the complete multilayer shell (which consists of 9 layers) that has a prescribed initial moisture gradient across the thickness. This moisture gradient captures the full sequence of dipping and drying and the prescribed gradient has been derived from the related reference (Leyland and

Jones, 11-14 September 1995) as given in the Figure 6.12 above. The simulation is implemented on the simple linear section as described in the Figure 6.28 below. In this problem no gradient is prescribed at each layer interface due to the fact that the difference in saturation between each layer is small. Also the coarse mesh within this multilayer structure is enough to solve via the proposed scheme. The same boundary condition and the drying environment as presented in Section 6.4.1 has been used to have the same drying effect for the layered system (as implemented in the experimental work). The domain was mapped using a uniform finite element mesh comprising 53 nodes and 9 quadratic serendipity elements, with an overall thickness of 9 mm, representing the multilayer shell body. A variable time step, based on initial, minimum and maximum time step size of 1sec, 0.001sec and 48 hours respectively, was employed for the simulation. The above mentioned spatial and temporal discretisations were applied after a thorough investigation to obtain a converged solution. Comparison of the simulated average value of water loss within the multilayer domain was made with the experimental data. This comparison was made by referring to the drying results for the fully layered system.

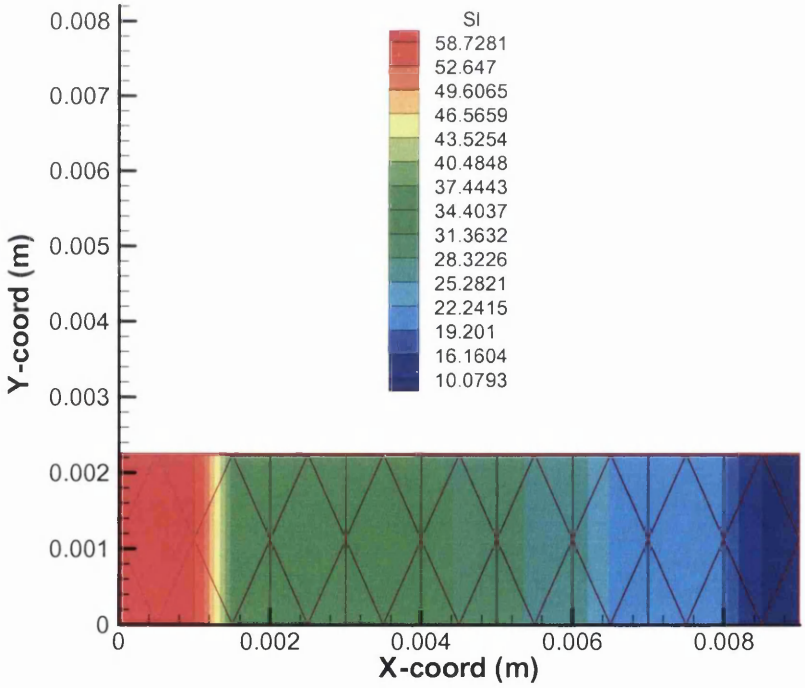

Figure 6.28: Schematic of multilayer shell with 9 layers – initial moisture variation.

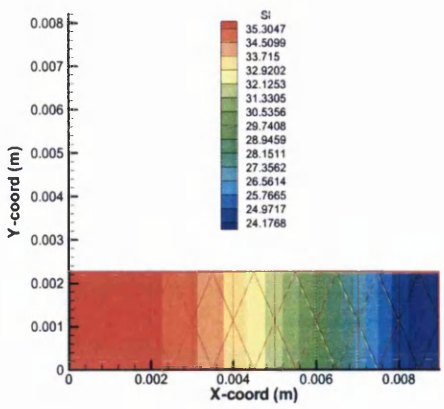
SI
35.3047
34.5099
33.715
32.9202
32.1253
31.3305
30.5356
29.7408
28.9459
28.1511
27.3562
26.5614
25.7665
24.9717
24.1768
Y-coord (m)
X-coord (m)
0.008
0.007
0.006
0.005
0.004
0.003
0.002
0.001
0
0.002
0.004
0.006
0.008

(a)

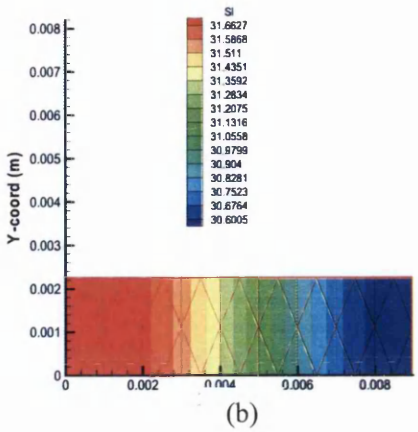
SI
31.6627
31.5868
31.511
31.4351
31.3592
31.2834
31.2075
31.1316
31.0558
30.9799
30.904
30.8281
30.7523
30.6764
30.6005
Y-coord (m)
0.008
0.007
0.006
0.005
0.004
0.003
0.002
0.001
0
0.002
0.004
0.006
0.008

(b)

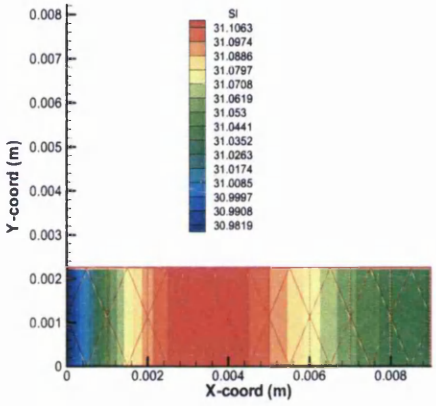
SI
31.1063
31.0974
31.0886
31.0797
31.0708
31.0619
31.053
31.0441
31.0352
31.0263
31.0174
31.0085
30.9997
30.9908
30.9819
Y-coord (m)
X-coord (m)
0.008
0.007
0.006
0.005
0.004
0.003
0.002
0.001
0
0.002
0.004
0.006
0.008

(c)

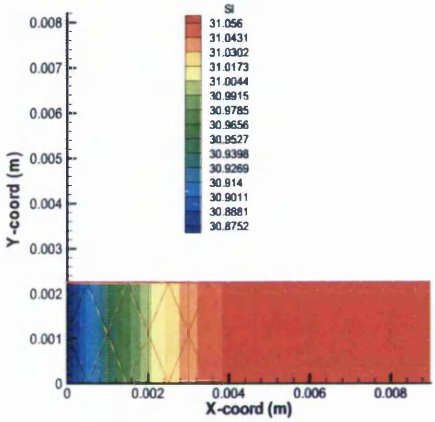
SI
31.056
31.0431
31.0302
31.0173
31.0044
30.9915
30.9785
30.9656
30.9527
30.9398
30.9269
30.914
30.9011
30.8881
30.8752
Y-coord (m)
X-coord (m)
0.008
0.007
0.006
0.005
0.004
0.003
0.002
0.001
0
0.002
0.004
0.006
0.008

(d)

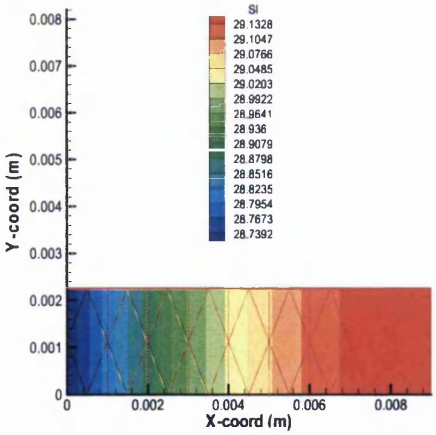
SI
29.1328
29.1047
29.0766
29.0485
29.0203
28.9922
28.9641
28.936
28.9079
28.8798
28.8516
28.8235
28.7954
28.7673
28.7392
Y-coord (m)
X-coord (m)
0.008
0.007
0.006
0.005
0.004
0.003
0.002
0.001
0
0.002
0.004
0.006
0.008

(e)

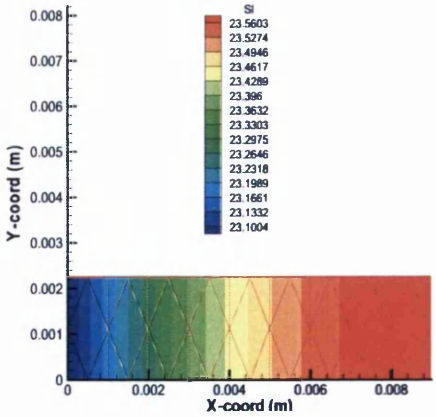
SI
23.5603
23.5274
23.4946
23.4617
23.4289
23.396
23.3632
23.3303
23.2975
23.2646
23.2318
23.1989
23.1661
23.1332
23.1004
Y-coord (m)
X-coord (m)
0.008
0.007
0.006
0.005
0.004
0.003
0.002
0.001
0
0.002
0.004
0.006
0.008

(f)

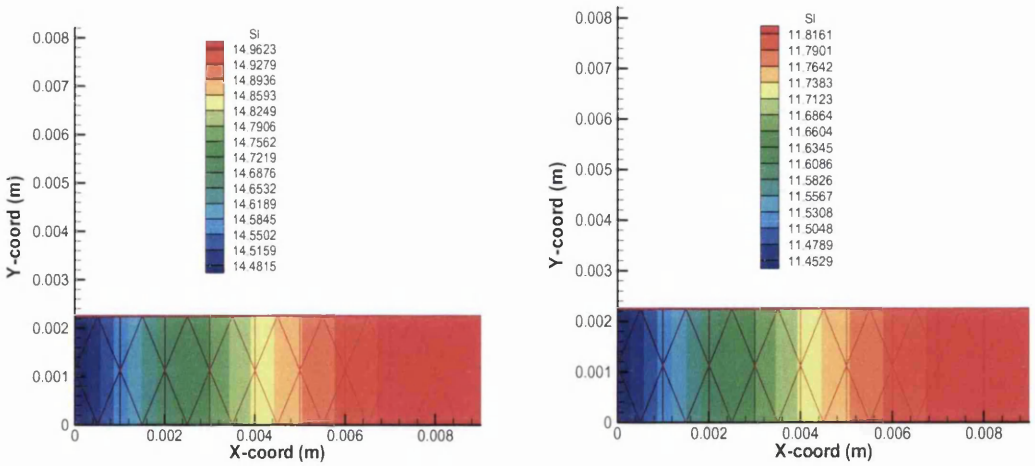

(g)

(h)

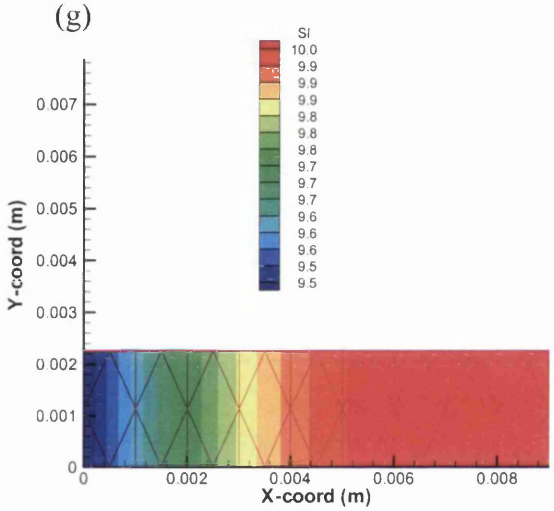

(i)

Figure 6.29: Saturation at 1 minutes (a), 3 minutes (b), 4.5 minutes(c), 5 minutes (d), 30 minutes (e), 2 hours (f), 7 hours (g), 12 hours (h) and 19 hours (i) of the multilayer shell.

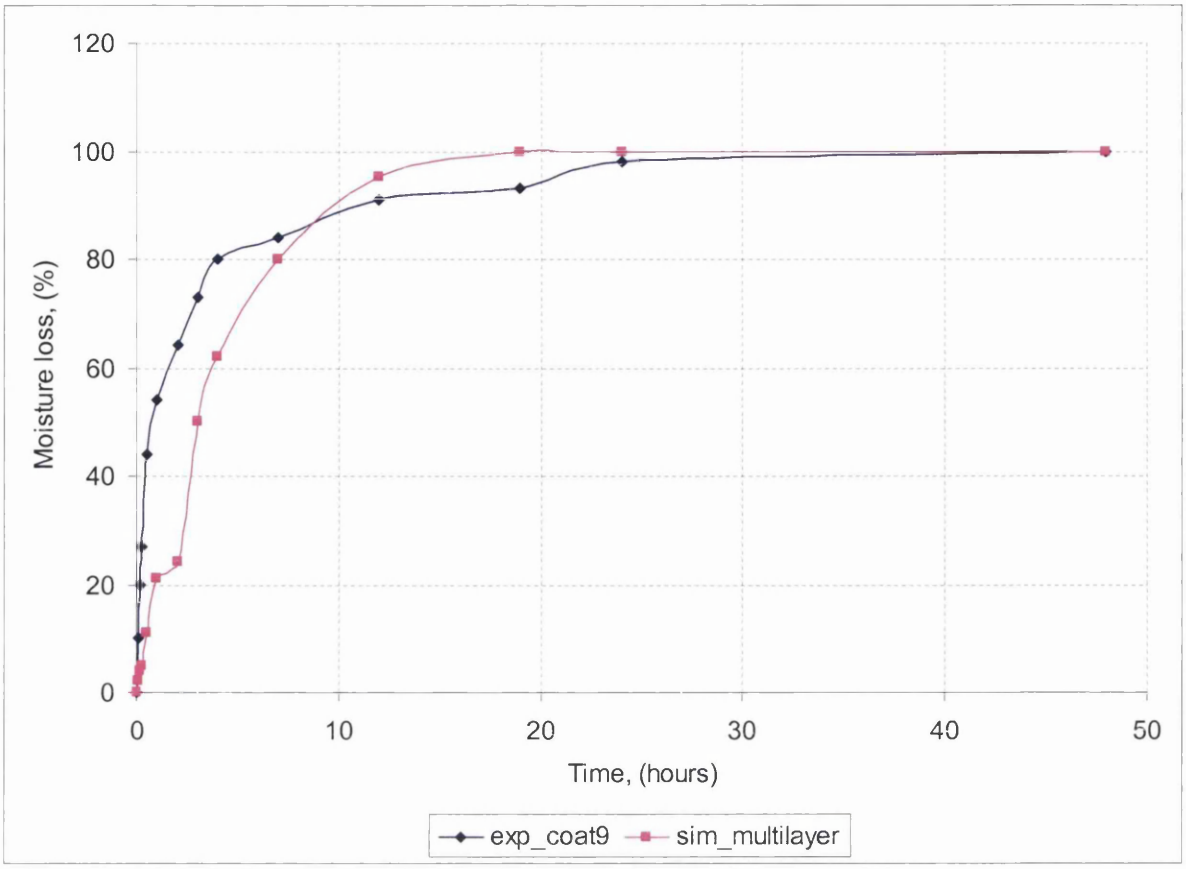

Figure 6.30: Comparison between the predicted and experimental values of the moisture loss for the fully layered system in the second approach.

Simulation of the drying of the fully layered system shows more deviation from the experimental data as compared to the previous case study (see Figure 6.29). The most clear difference can be seen at the beginning of the drying time, where moisture loss for the whole body is slower than in the first approach This is not shown in the experimental data. Comparison between the case studies under Approach 1 (from Figure 6.27) and Approach 2 (Figure 6.30) with the experiment result , show a slight difference, where most of the simulated results under Approach 1 agrees with the same pattern with the experimental data. So, therefore it can be concluded that the Approach 1 shows the best solution in simulating the drying of shell. In fact it is the method that may be used 'ab initio' to simulate the drying process.

6.4.2.3 Mesh Sensitivity study

This section is presented in order to determine the accuracy of the prediction in every case study which is mapped by a coarse mesh. Therefore, some comparison with different meshes in a straight layer geometry and corner shape with two different distinct layers were investigated and these are presented in following sections. All figures are presented based on the same scale of contour colour in order to enable a direct comparison to highlight mesh sensitivity.

6.4.2.3.1 Two layer linear section

In this case study, a two layer system mapped with a coarse mesh (10 elements) and a finer mesh (20 elements) was examined. Both domains have the same level of saturation with two different distinct layers. In describing the two distinct layers in the domain, the interface area that captures the steep gradient between the two layers needs to be defined in both domains.

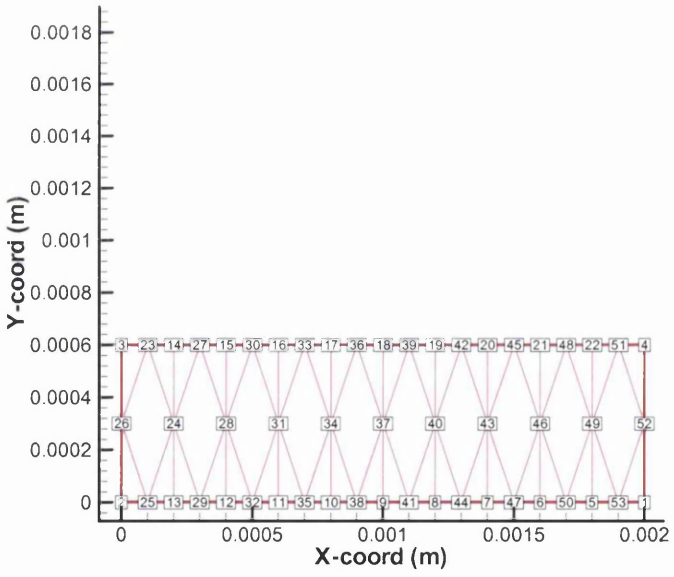

Figure 6.31: Schematic for node numbering across the domain

The same drying condition and the same time step, based on initial, minimum and

maximum time step respectively were chosen as in the Section 6.4.2.2 was employed for both simulations in both case studies. Both domains are exposed to the convective boundary condition at one side while the other side is insulated and impermeable. The results from the simulation are shown below in the form of saturation contours.

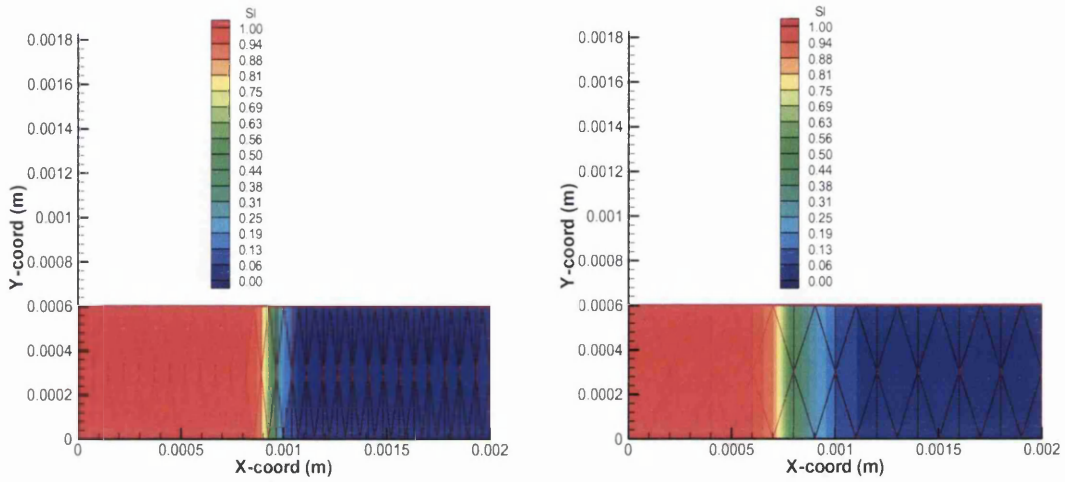

(a)

Scale : 1.00 = 58.87
0.00 = 10.07

(b)

Scale : 1.00 = 58.87
0.00 = 10.07

Figure 6.32: Initial condition for saturation level in the coarse and fine mesh for a two layer shell system

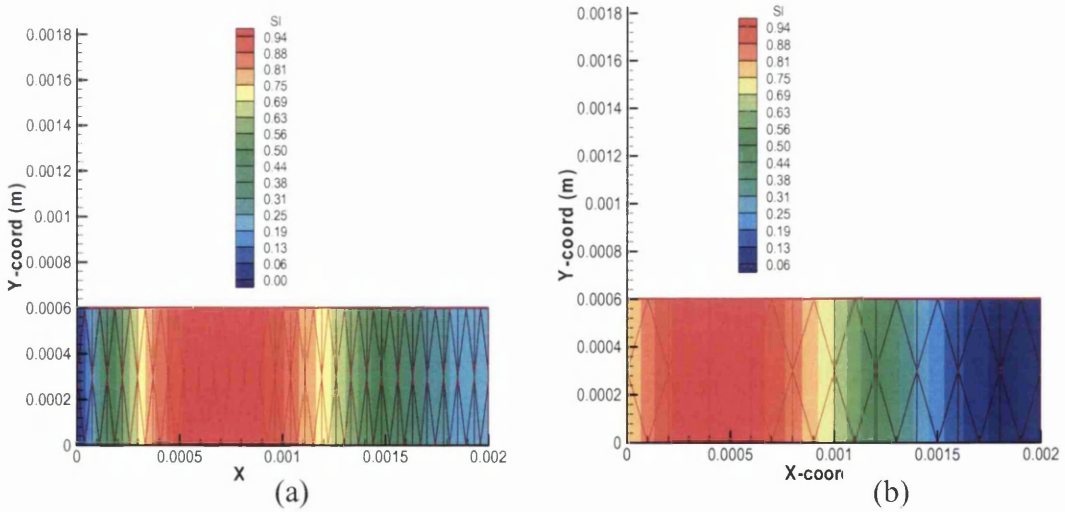

(a)

Scale : 0.94 = 32.963
0.00 = 32.940

(b)

Scale : 0.94 = 30.180
0.00 = 10.070

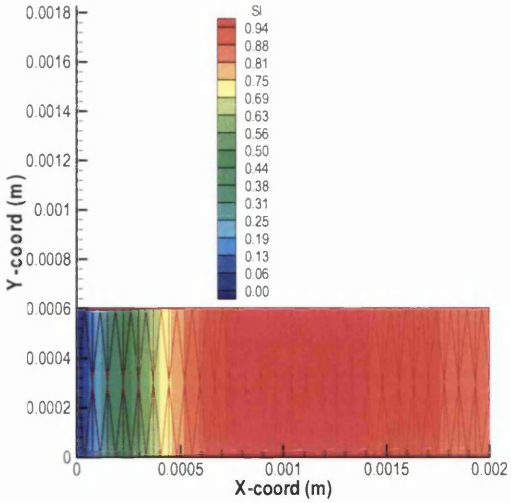

(c)

Scale : 0.94 = 32.953
0.00 = 32.922

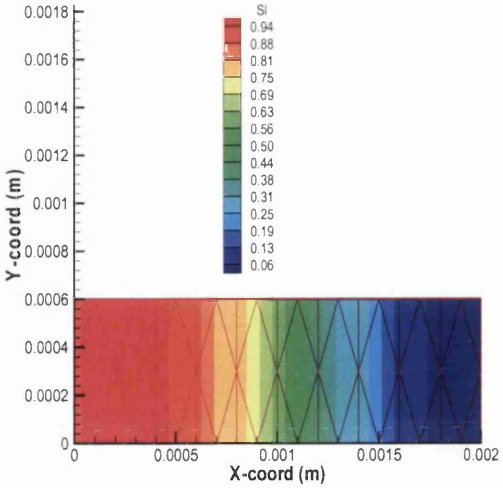

(d)

Scale : 0.94 = 30.144
0.00 = 30.030

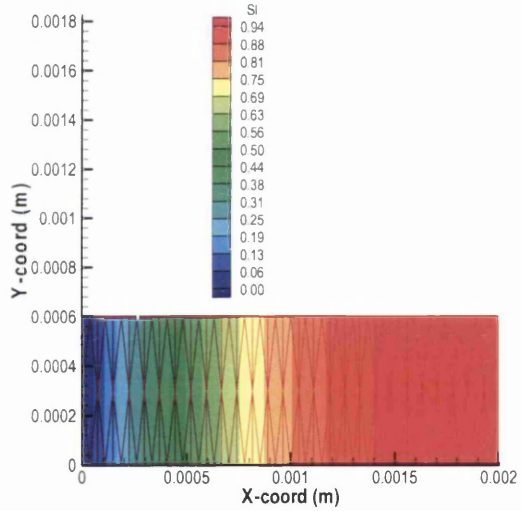

(e)

Scale : 0.94 = 32.944
0.00 = 32.887

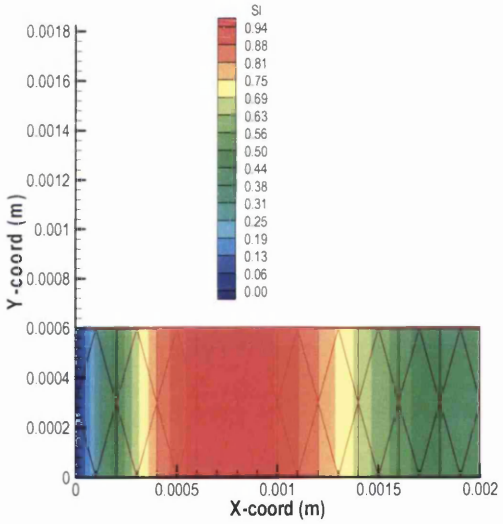

(f)

Scale : 0.94 = 30.085
0.00 = 30.056

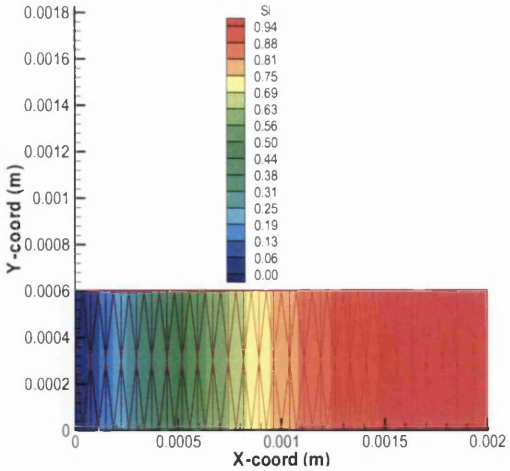

(g)

Scale : 0.94 = 32.934
0.00 = 32.871

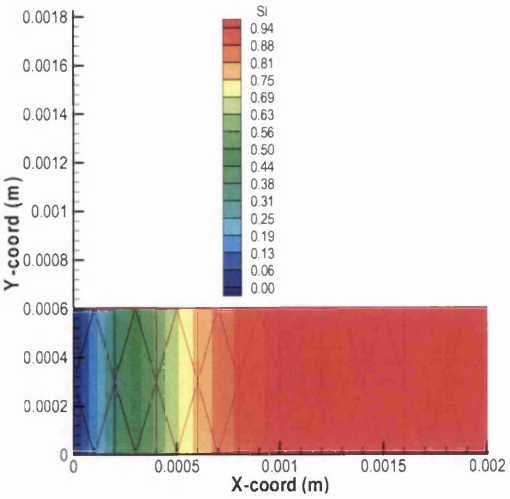

(h)

Scale : 0.94 = 30.072
0.00 = 30.025

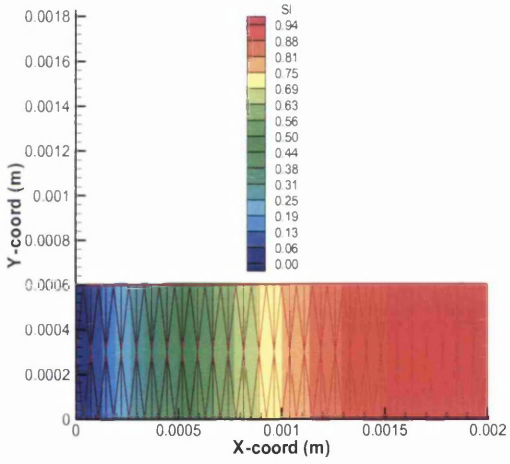

(i)

Scale : 0.94 = 18.271
0.00 = 18.156

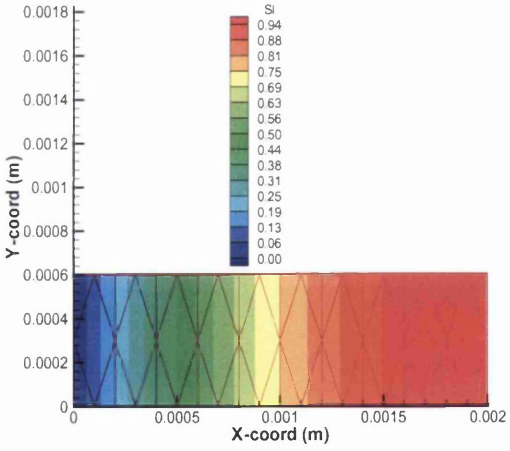

(j)

Scale : 0.94 = 17.350
0.00 = 17.235

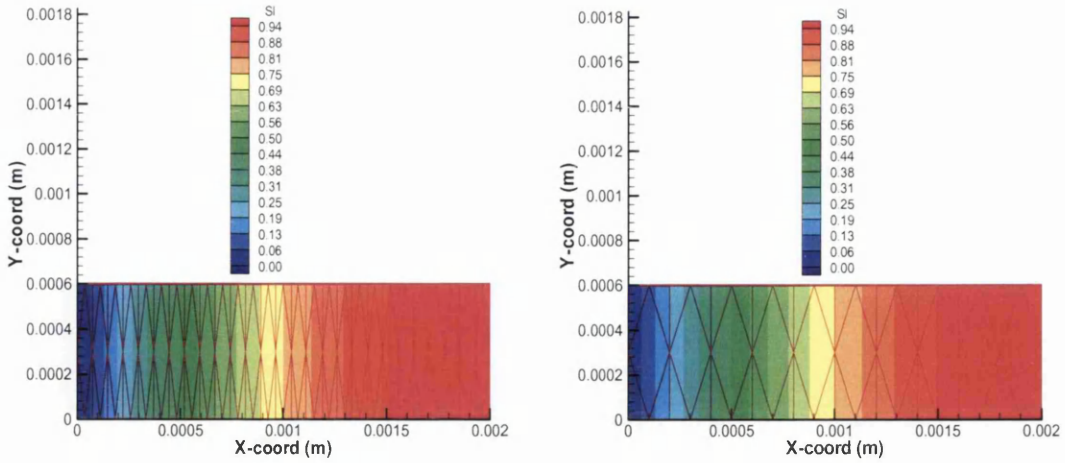

(k)

Scale : 0.94 = 13.248
0.00 = 13.146

(l)

Scale : 0.94 = 12.878
0.00 = 12.779

Figure 6.33: Comparison of saturation level at 17 seconds((a),(b)), 19 seconds((c),(d)), 21 seconds((e),(f)), 23 seconds((g),(h)), 1 hour((i),(j)) and 2 hour((k),(l)) for both meshes.

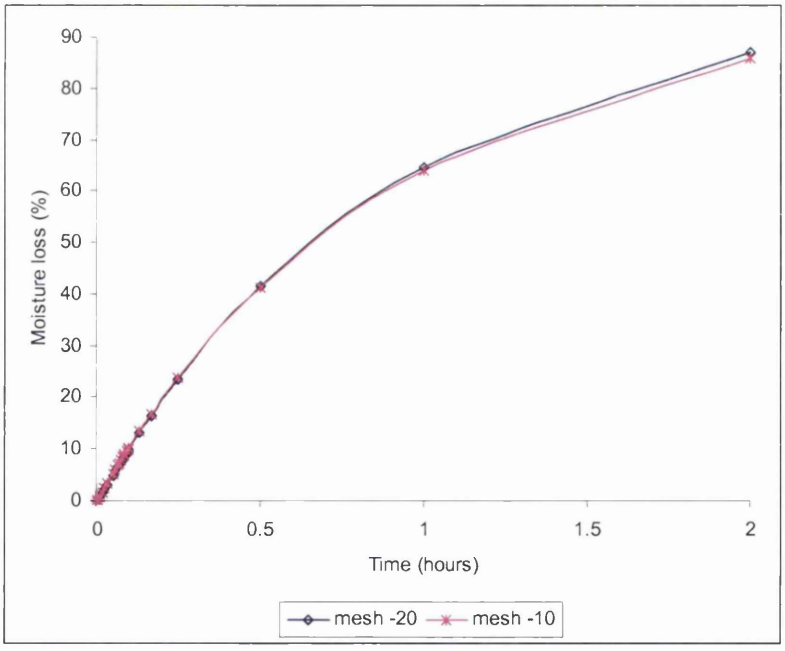

Figure 6.34: Comparison of moisture loss between mesh 20 and mesh 10 at node 2 over a 2 hour drying time.

6.4.2.3.2 Single layer corner section.

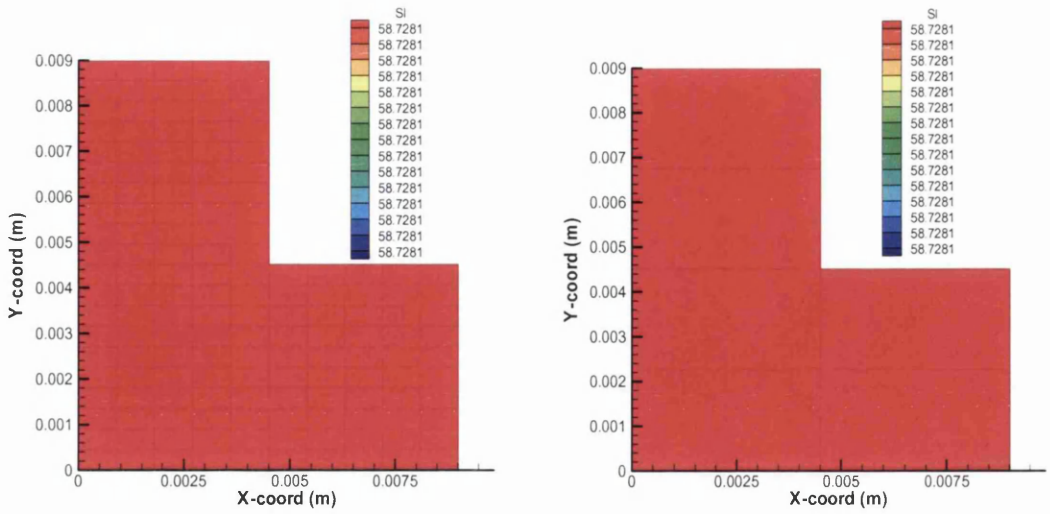

(a) (b)

Figure 6.35: Initial condition for saturation level in the coarse and fine mesh for the corner section.

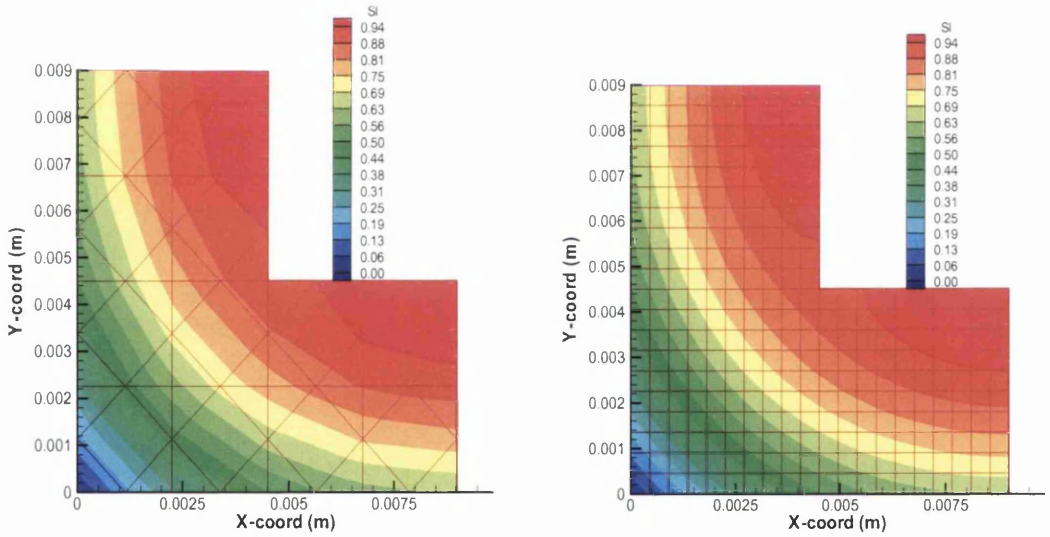

(c) (d)

Scale : 0.94 = 54.734
0.00 = 54.604

Scale : 0.94 = 54.735
0.00 = 54.605

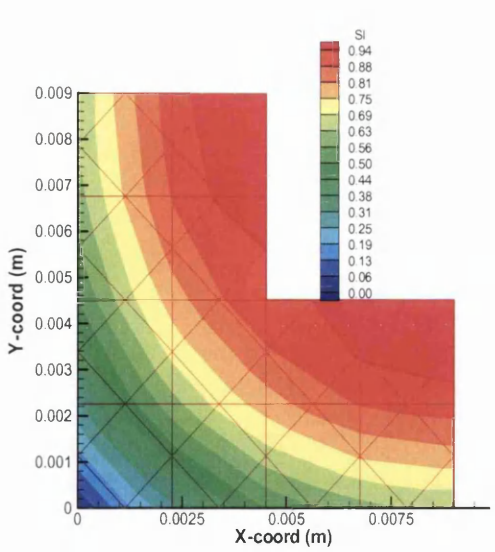

(e)

Scale : 0.94 = 50.770
0.00 = 50.615

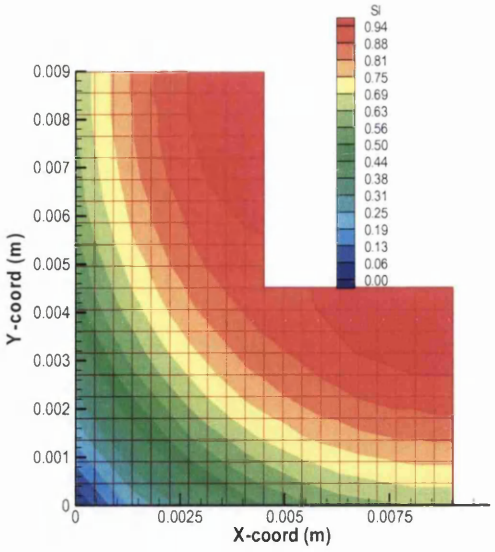

(f)

Scale : 0.94 = 50.757
0.00 = 50.601

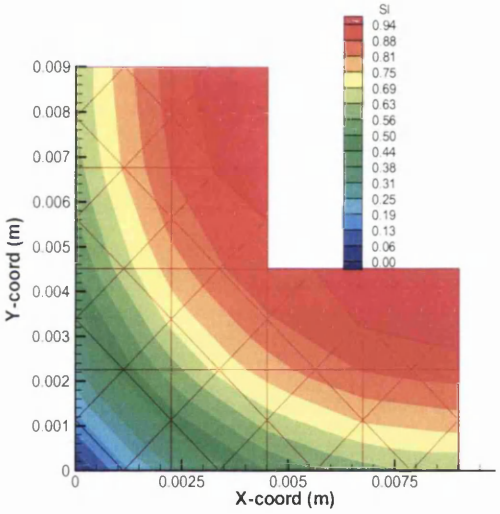

(g)

Scale : 0.94 = 28.914
0.00 = 28.365

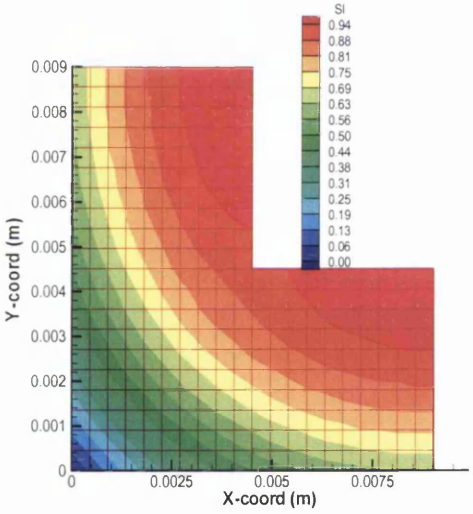

(h)

Scale : 0.94 = 28.977
0.00 = 28.429

Figure 6.36: Comparison of the coarse mesh (12 elements) and finer mesh (75 elements) over 2 hours drying times.

In these case studies (linear section and corner section), both meshes (fine and coarse) show very little difference in saturation level, being less than 2% over the two hour drying period. However there is a big different in computing time. Using the same computing platform, the coarse mesh (10 elements) needed less than 30 minutes, but

the finer mesh required more than 5 hours computing time which is 10 times longer than the coarse mesh. Therefore, the coarse mesh was considered to be adequate to run the the single layer and multilayer case studies in Section 6.4.1 and in Section 6.4.2.

6.5 Drying Case Study of the shell with Corner Geometry

Based on the above validation, the simulation was extended to include moisture and heat transport from two sides effectively capturing a corner which is a generic shape in a ceramic shell body. This was done in order to demonstrate the robustness of the code and also to illustrate the hygrothermal response especially in the corner zone of a single and multi layer shell. The same material properties that have been used in Section 6.4 were used in this work. In this section, the same condition for shell drying as presented in the previous Section 6.4 was used.

6.5.1 Corner shell with single layer

The simulation was completed for a single layer ceramic shell with thickness of 1 mm. A uniform size of mesh comprising 53 nodes and 12 quadratic serendipity elements was used to represent the sample. The mesh configuration of the sample is shown in Figure 6.31. A variable time step, based on initial, minimum and maximum time step size of 1 second, 0.001 second and 2 hours respectively, was employed for the simulation. The convective boundary is shown in the Figure 6.37 and other parts of boundary are assumed insulated. Initially the shell layer has saturation equal to 59% and pore water pressure -7.5×10^6 (Pa) constant throughout the body. Results of the simulation for the level of saturation and pore water pressure with different times are shown in Figure 6.38.

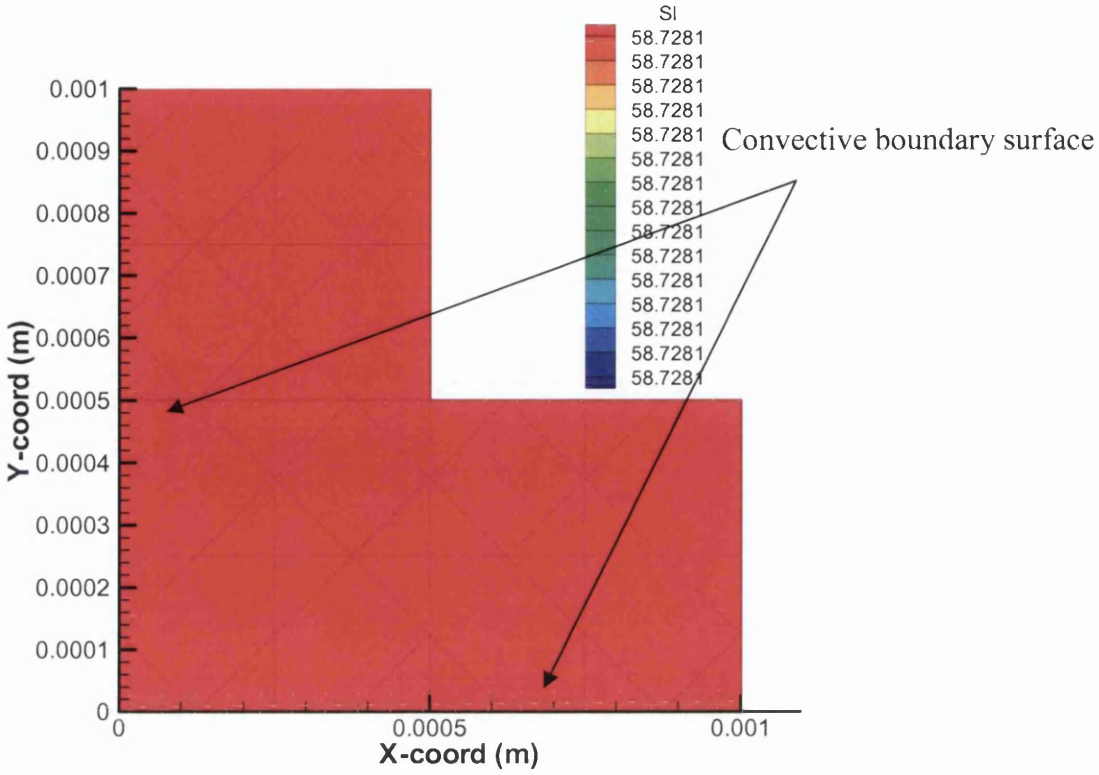

Figure 6.37: The domain mesh and boundry conditions for single layer with corner shape.

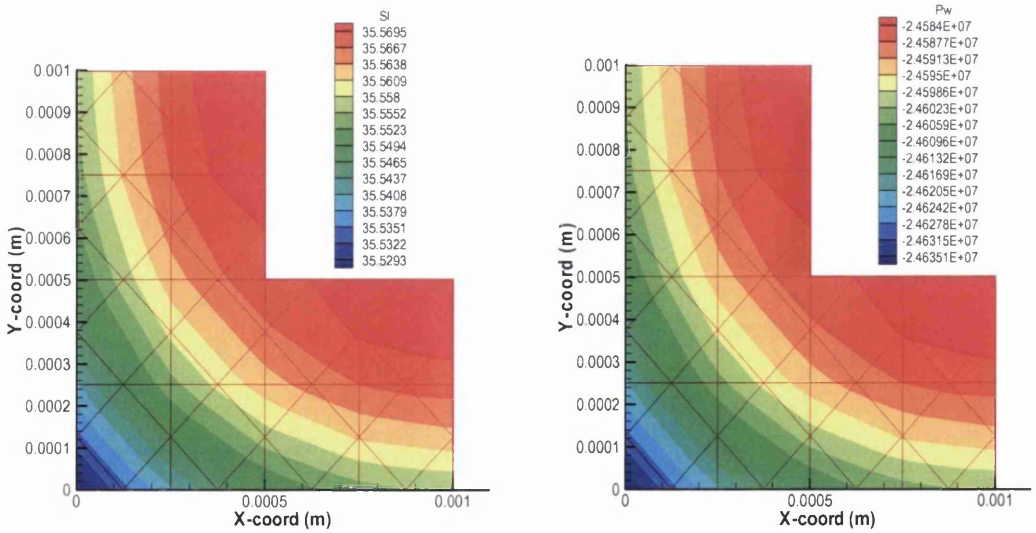

(a) (b)

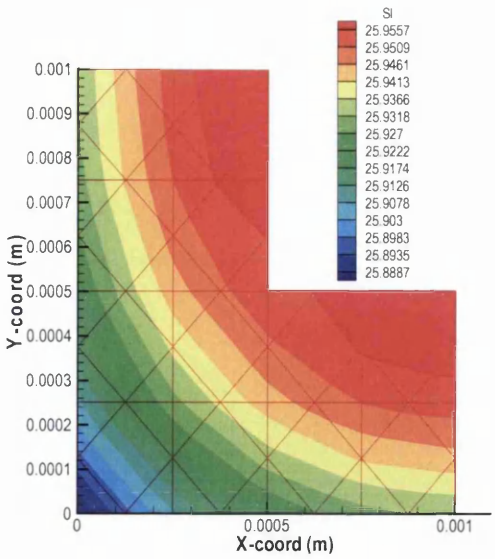
Sl
25.9557
25.9509
25.9461
25.9413
25.9366
25.9318
25.927
25.9222
25.9174
25.9126
25.9078
25.903
25.8983
25.8935
25.8887
Y-coord (m)
X-coord (m)
0
0.0001
0.0002
0.0003
0.0004
0.0005
0.0006
0.0007
0.0008
0.0009
0.001
0.0005

(c)

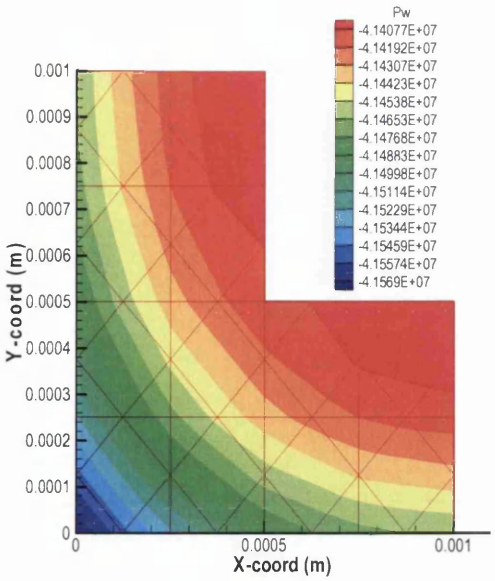
Pw
-4.14077E+07
-4.14192E+07
-4.14307E+07
-4.14423E+07
-4.14538E+07
-4.14653E+07
-4.14768E+07
-4.14883E+07
-4.14998E+07
-4.15114E+07
-4.15229E+07
-4.15344E+07
-4.15459E+07
-4.15574E+07
-4.1569E+07
Y-coord (m)
X-coord (m)
0
0.0001
0.0002
0.0003
0.0004
0.0005
0.0006
0.0007
0.0008
0.0009
0.001
0.0005

(d)

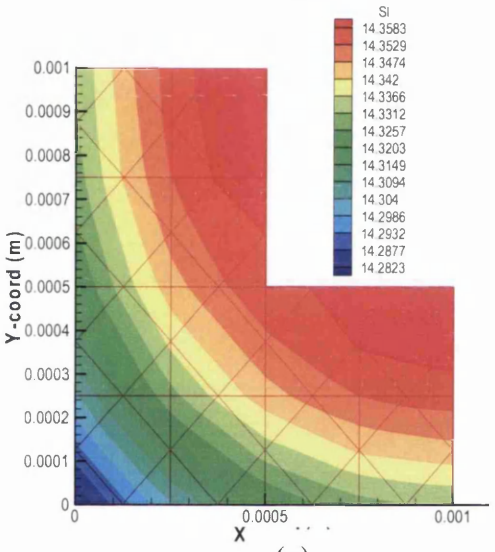
Sl
14.3583
14.3529
14.3474
14.342
14.3366
14.3312
14.3257
14.3203
14.3149
14.3094
14.304
14.2986
14.2932
14.2877
14.2823
Y-coord (m)
X
0
0.0001
0.0002
0.0003
0.0004
0.0005
0.0006
0.0007
0.0008
0.0009
0.001
0.0005

(e)

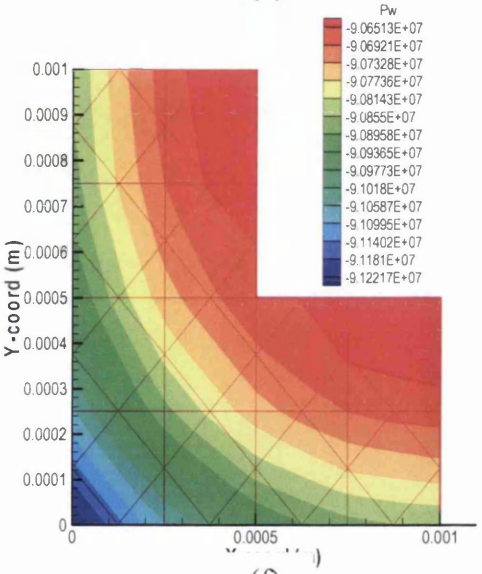
Pw
-9.06513E+07
-9.06921E+07
-9.07328E+07
-9.07736E+07
-9.08143E+07
-9.0855E+07
-9.08958E+07
-9.09365E+07
-9.09773E+07
-9.1018E+07
-9.10587E+07
-9.10995E+07
-9.11402E+07
-9.1181E+07
-9.12217E+07
Y-coord (m)
0
0.0001
0.0002
0.0003
0.0004
0.0005
0.0006
0.0007
0.0008
0.0009
0.001
0.0005

(f)

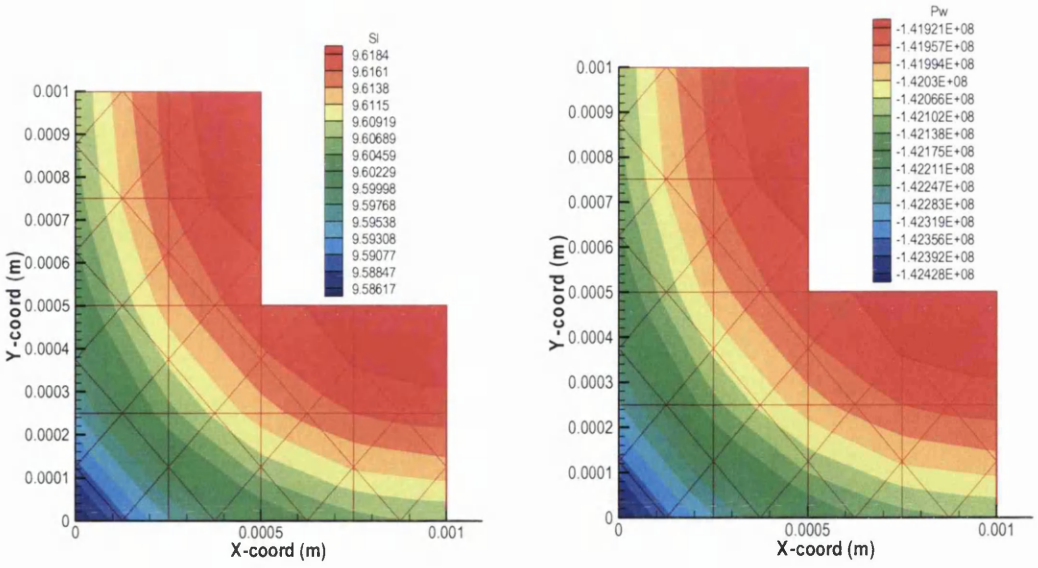

(g) (h)

Figure 6.38: Saturation and pore water pressure at 15 minutes (a), 30 minutes (b), 1 hour (c) and 2 hours (d) of drying times for the single layer case study (corner shape).

At the time increments, the saturation value shows only a small variation across the body due to the geometry of the ceramic shell layer (1 mm thick) and its ability to promote moisture transport. Over the drying times, as expected the greatest changes are observed in the corner zone where the saturation reaches its minimum value due to the convection from two adjacent sides. In the early stage of drying (constant rate period) or above the critical value (0.3), saturation drops drastically within 30 minutes. This condition indicates the capillarity effect and free water movement that leads to the moisture loss. As drying proceeds and exceeds the critical value after 30 minutes, moisture loss slowly starts to reduce and the same result is exhibited in the pore water pressure. This is clearly shown by comparing the value of saturation in Figure 6.38, where it took nearly 1 hour to have a reduction of 5% in saturation as compared to the beginning of drying time, where its shows a 34% loss in saturation in less than 30 minutes.

6.5.2 Corner Shell with multilayer

The multilayer system was simulated for just two layers. This case study follows the previous approach set out in Section 6.4 under **Approach 1**. A uniform size of mesh comprising 341 nodes and 75 quadratic serendipity elements was used to represent the sample with 5 mm length and 2.5 mm thickness. In presenting the layering system that is clearly shown by the two distinct layers, a finer mesh needs to be used to capture the interface layer that has a very steep difference in moisture content. The interface gradient needs to be define to avoid numerical difficulties in the simulation. The mesh configuration is shown in Figure 6.39. A variable time step, based on initial, minimum and maximum time step size of 1 second, 0.001 second and 2 hours respectively, was employed for the both simulations. The same convective boundary as implemented in the previous case study (is shown in the Figure 6.37) is also implemented in this problems, and their initial saturation that describes the two layer system is given in Figure 6.39. The same drying condition as implemented in the previous Section 6.4 is used in this problem. Simulated results of the working variables with different times are shown in Figures below.

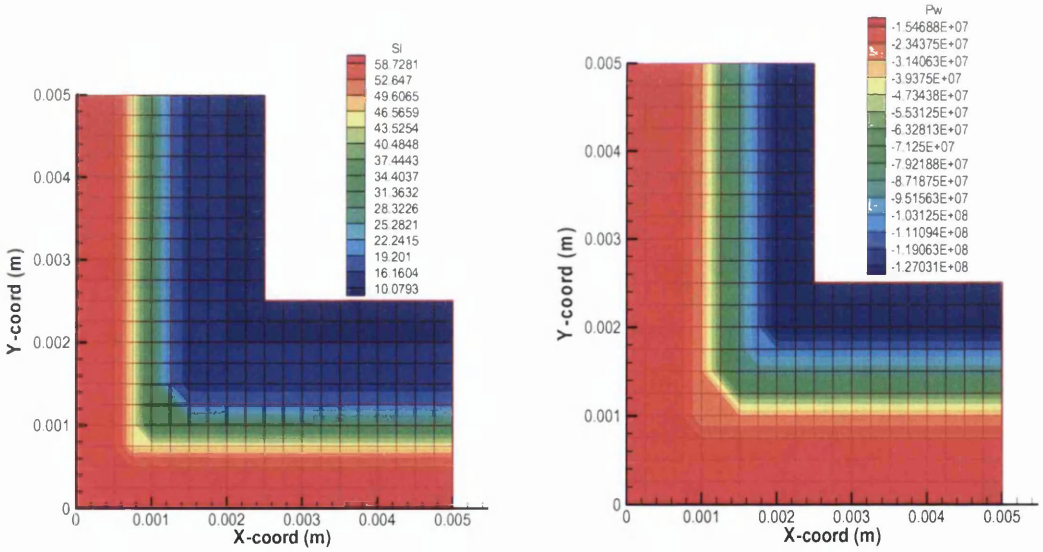

(a) (b)

Figure 6.39: Initial condition of the saturation and pore water pressure for two layer systems with corner shape.

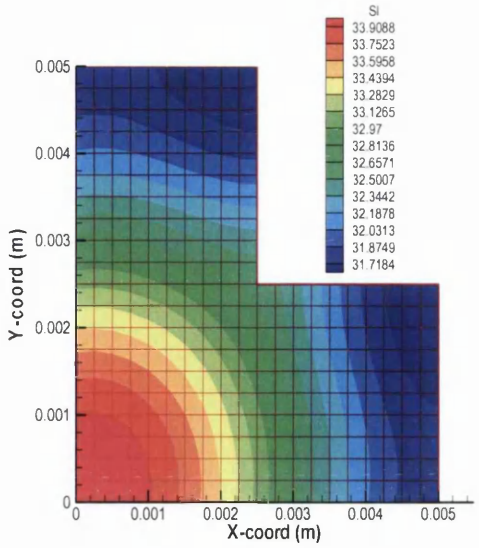
Sl
33.9088
33.7523
33.5958
33.4394
33.2829
33.1265
32.97
32.8136
32.6571
32.5007
32.3442
32.1878
32.0313
31.8749
31.7184
Y-coord (m)
X-coord (m)
0
0.001
0.002
0.003
0.004
0.005

(a)

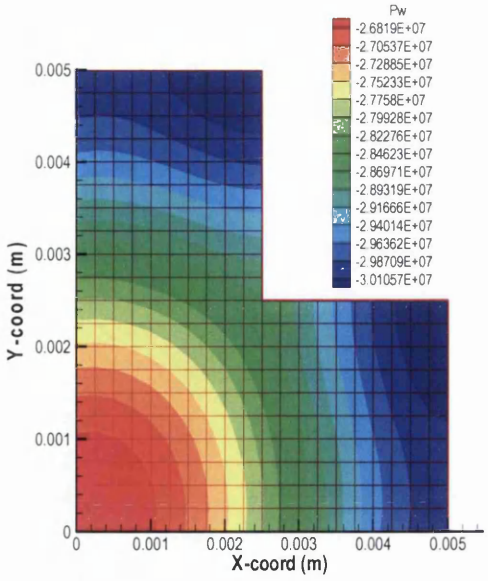
Pw
-2.6819E+07
-2.70537E+07
-2.72885E+07
-2.75233E+07
-2.7758E+07
-2.79928E+07
-2.82276E+07
-2.84623E+07
-2.86971E+07
-2.89319E+07
-2.91666E+07
-2.94014E+07
-2.96362E+07
-2.98709E+07
-3.01057E+07
Y-coord (m)
X-coord (m)
0
0.001
0.002
0.003
0.004
0.005

(b)

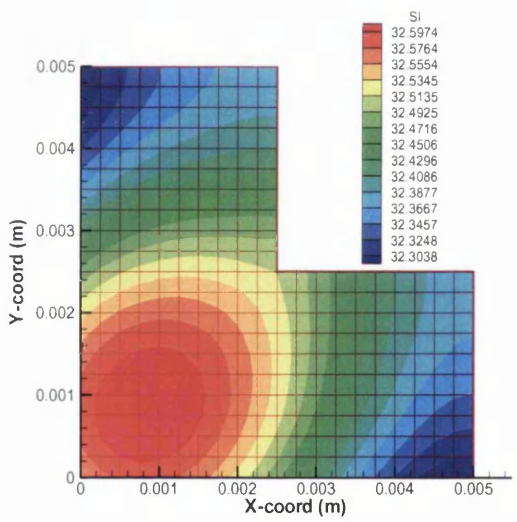
Sl
32.5974
32.5764
32.5554
32.5345
32.5135
32.4925
32.4716
32.4506
32.4296
32.4086
32.3877
32.3667
32.3457
32.3248
32.3038
Y-coord (m)
X-coord (m)
0
0.001
0.002
0.003
0.004
0.005

(c)

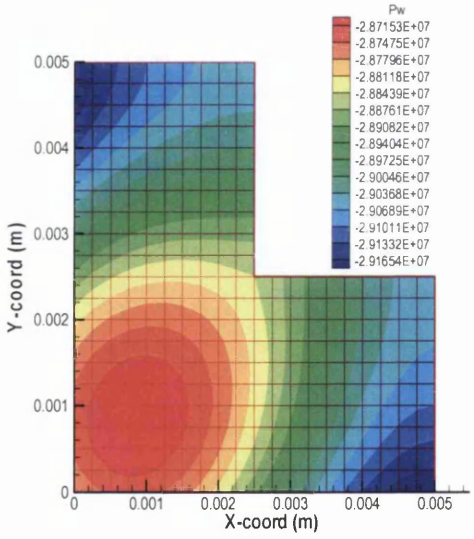
Pw
-2.87153E+07
-2.87475E+07
-2.87796E+07
-2.88118E+07
-2.88439E+07
-2.88761E+07
-2.89082E+07
-2.89404E+07
-2.89725E+07
-2.90046E+07
-2.90368E+07
-2.90689E+07
-2.91011E+07
-2.91332E+07
-2.91654E+07
Y-coord (m)
X-coord (m)
0
0.001
0.002
0.003
0.004
0.005

(d)

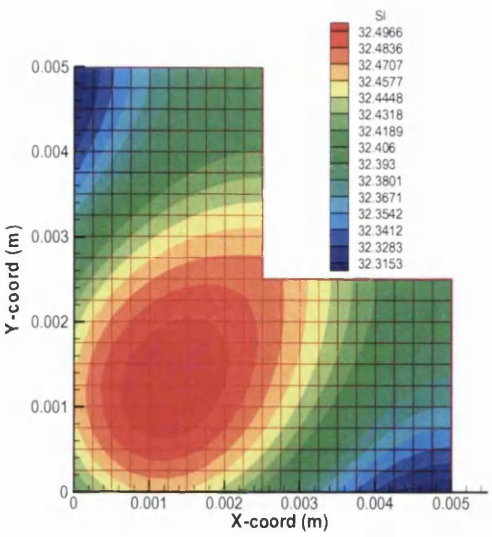
Sl
32.4966
32.4836
32.4707
32.4577
32.4448
32.4318
32.4189
32.406
32.393
32.3801
32.3671
32.3542
32.3412
32.3283
32.3153
Y-coord (m)
X-coord (m)

(e)

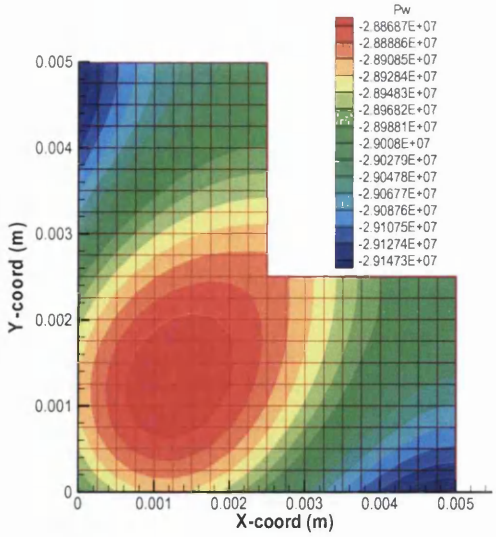
Pw
-2.88687E+07
-2.88886E+07
-2.89085E+07
-2.89284E+07
-2.89483E+07
-2.89682E+07
-2.89881E+07
-2.9008E+07
-2.90279E+07
-2.90478E+07
-2.90677E+07
-2.90876E+07
-2.91075E+07
-2.91274E+07
-2.91473E+07
Y-coord (m)
X-coord (m)

(f)

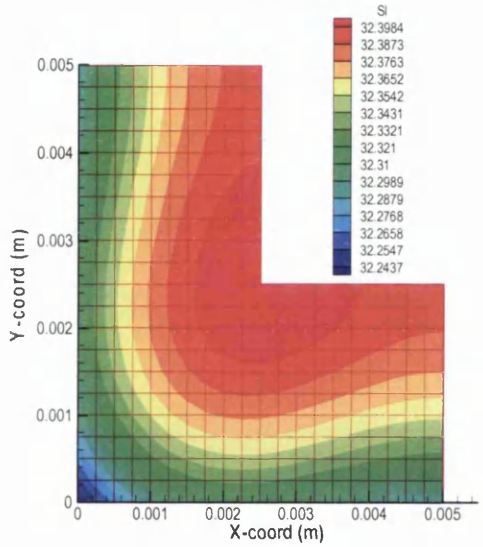
Sl
32.3984
32.3873
32.3763
32.3652
32.3542
32.3431
32.3321
32.321
32.31
32.2989
32.2879
32.2768
32.2658
32.2547
32.2437
Y-coord (m)
X-coord (m)

(g)

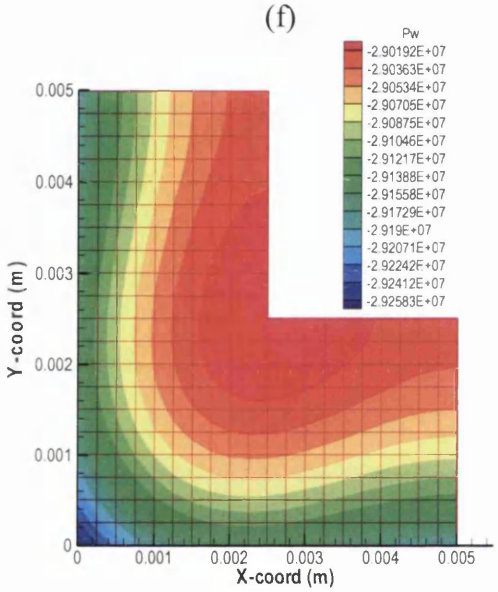
Pw
-2.90192E+07
-2.90363E+07
-2.90534E+07
-2.90705E+07
-2.90875E+07
-2.91046E+07
-2.91217E+07
-2.91388E+07
-2.91558E+07
-2.91729E+07
-2.919E+07
-2.92071E+07
-2.92242E+07
-2.92412E+07
-2.92583E+07
Y-coord (m)
X-coord (m)

(h)

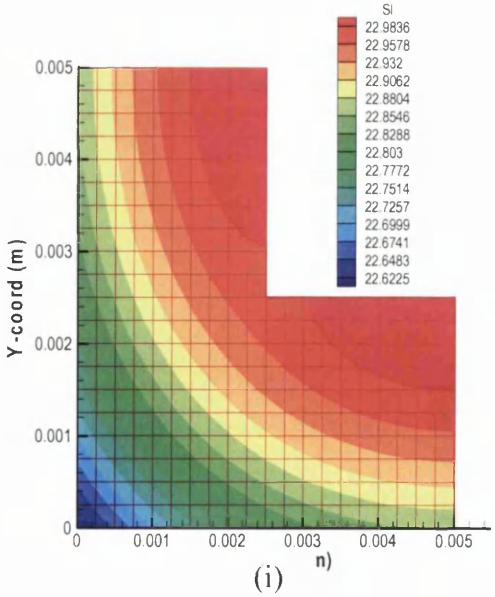
Sl
22.9836
22.9578
22.932
22.9062
22.8804
22.8546
22.8288
22.803
22.7772
22.7514
22.7257
22.6999
22.6741
22.6483
22.6225
Y-coord (m)
n)

(i)

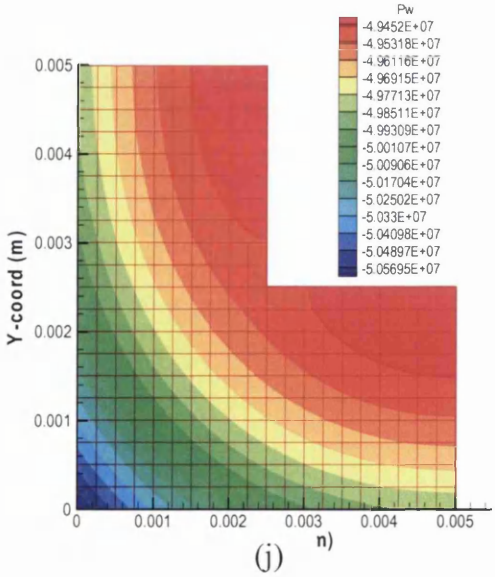
Pw
-4.9452E+07
-4.95318E+07
-4.96116E+07
-4.96915E+07
-4.97713E+07
-4.98511E+07
-4.99309E+07
-5.00107E+07
-5.00906E+07
-5.01704E+07
-5.02502E+07
-5.033E+07
-5.04098E+07
-5.04897E+07
-5.05695E+07
Y-coord (m)
n)

(j)

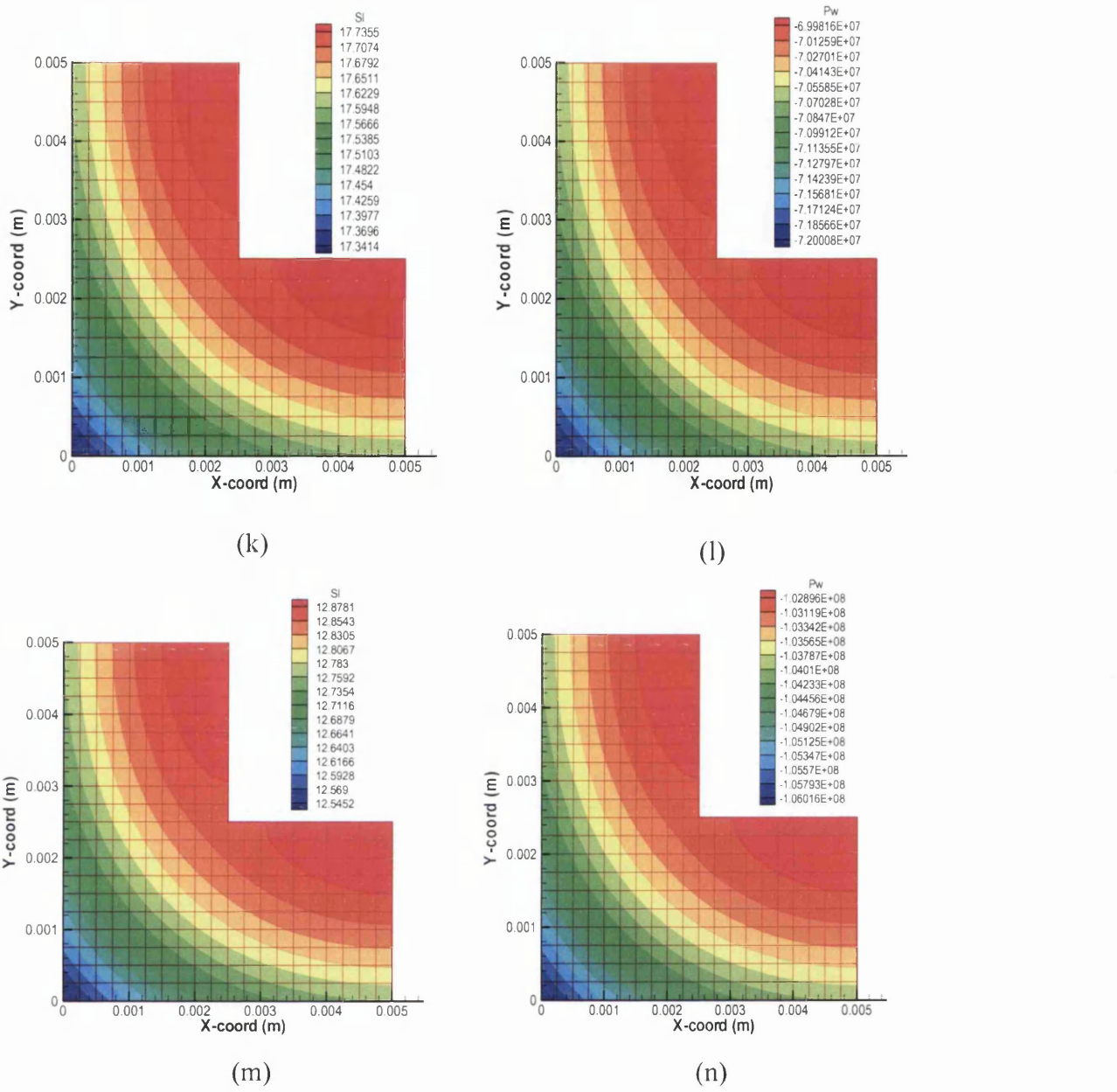

Figure 6.40: Saturation and pore water pressure at 25 seconds; (a) and (b), 45 seconds; (c) and (d), 50 seconds; (e) and (f), 1 minute; (g) and (h), 30 minutes; (i) and (j), 1 hours; (k) and (l), 2 hours; (m) and (n).

At the beginning of drying of the multilayer system there is a considerable shift in the moisture condition, as has already been discussed and illustrated in the linear plain sections. The saturation level in Figure 6.40 shows a big moisture loss at the beginning of drying. Less than 30 minutes is needed to dry the body to the critical value at 22 % saturation level (which is equal to 70-75% moisture loss). The two layers systems show a nearly fully dried condition within 2 hours. The average value

of saturation (12 %) indicates the value of 90% moisture loss at two hours drying time. In general, the results show the expected trends, but they need to be compared with experimental data when these become available.

6.6 Closure

In this chapter, the accuracy of the solutions obtained by the numerical approximation used in the proposed model was investigated. The problems chosen for the validation and analysis were one-dimensional linear heat flow accommodating various initial conditions and boundary conditions. Dirichlet boundary condition and flux boundary condition in which related to a convection mechanism were solved numerically using the proposed model. The computed numerical results were compared with analytical heat transfer solutions (Carslaw and Jaeger, 1959) and showed a good agreement.

The verification of a fully coupled model in one dimensional scale, which considers moisture, heat transfer and gas transport (air and vapour) for brick drying, was carried out using data from a previous numerical work presented by Stanish *et al* (1986). This analysis considered the simulation of temperature, moisture and other material transport evolution during the drying process. Simulation results of the measured variables at different times and across the drying body section showed a good matching with results reported by Stanish *et al* (1986) and in others related work.

Extension of the model validation into a two dimensional scale was done for the drying of a ceramic layer (single layer and multilayer) on the simple linear section and the corner shape geometry. These simulations and investigations were done with considering the nearly isothermal ambient condition that are pertinent to shell drying conditions. It was observed that the simulation results of the measured variables showed a right pattern temporally and spatially between interrelated measured variables in the proposed model in every case study. A good correlation also was noticed between the simulated results and experimental data for the case of simulation of multilayer system that follows directly the experimental work. The same procedure

for a multilayer system as implemented for to the simple linear section also proved to be applicable to the corner shape problem.

Therefore, it can be concluded that the proposed fully coupled moisture, air and heat transfer model is able to describe the heat and mass transport that varies temporally and spatially during the shell drying process. The verifications and validations of the proposed model have also been published in two conference proceedings (Harun, *et al.*, April 2007; Harun, *et al.*, 2006).

REFERENCES

Baroghel-Bouny, V., Mainguy, M., Lassabatere, T., and Coussy, O., 1999, Chracaterization and Identification of Equilibrium and Transfer Moisture Properties for Ordinary and High-performance Cementitious Materials: Cement and Concrete Research, v. 29, p. 1225-1238.

Ben Nasrallah, S., and Perre, P., 1988, Detailed Study of A Model of Heat and Mass Transfer During Convective Drying of Porous Media: International Journal Heat Mass Transfer, v. 31, p. 957-967.

Briscoe, B.J., Biundo, G.L., and Ozken, N., 1998, Drying Kinetics of Water-Based Ceramic Suspensions for Tape Casting: Ceramics International, v. 24, p. 347-357.

Carlaw, H.S., and Jaeger, J.C., 1959, Conduction of Heat in Solids, p. 59-73.

de Vries, D.A, 1958., Simultaneous Transfer of Heat and Moisture in Porous Media: Trans. Am Geophysc Union, v. **39**, p. 909-916.

Gawin, D., and Schrefler, B.A., 1996, Thermo-Hydro-Mechanical Analysis of Partially Saturated Porous Materials: Engineering Computations, v. 13, p. 113-143.

Hyde, R., October 1995, The Rupture of Ceramic Moulds for Investment Casting: PhD theses, University of Birmingham, Birmingham.

Ilic, M., and Turner, I.W., 1989, Convective Drying of a Consolidated Slab of Wet Porous Material: International Journal Heat Mass Transfer, v. 32, p. 2351-2362.

Jones, S., 1995, The Use of Conductivity as A Means of Assessing The Extent of Wet Back in An Investment Mould, England, Material and Metallurgy Dept.,The University of Birmingham.

Kallel, F., Galanis, N., Perrin, B., and Javales, R., 1993, Effects of Moisture on Temperature During Drying of Consolidated Porous Materials: Transaction of ASME, v. 32, p. 1301-1311.

Leyland, S., and Jones, S., 11-14 September 1995, The Effect of Varying The Intercoat Drying Time Upon The Rate of Moisture Removal From Investment Casting Shell Mould: 22nd BICTA Conference.

Palananthakumar, B., 2004, A Finite Element Analysis of The Migration and Generation of Landfill Gas through Unsaturated Soil: PhD theses, Herriot-watt University.

Pierre, A. C., 1990, The Drying of Gels - A Model: Journal of The Canadian Ceramic Society, v. 59.

Spolek, G.A., and Plumb, O.A., 1981, Capillary Pressure in Softwood: Wood Science and Technology, v. 15, p. 189-199.

Stanish, M.A, Schajer G.S, and Kayihan, F., 1986, A Mathematical Model of Drying for Hygroscopic Porous Media: AIChE, v. 32, p. 1301-1311.

Tesoro, F.O, Choong, E.T., Kimbler O.K., 1974, Relative Permeability and The Porous Pore Structure of Wood: Wood and Fiber Science, v. 6, p. 226-236.

Harun, Z., Gethin, D.T., Lewis, R.W., and Ferguson, W.J., April 2007, Drying of A Multilayer Ceramic Shell Body: The Fifteenth UK Conference of The Association of Computational Mechanics in Engineering.

Harun, Z., Gethin, D.T., Lewis, R.W., and Ferguson, W.J., 2006, Combined Heat and Mass Transfer for Drying Ceramic Shell: The International Symposium on Multiphysics.

Zhang, Z., 1999, Mechanism and Mathematical Model of Heat and Mass Transfer During Convective Drying of Porous Materials: Heat Transfer_Asian Research, v. 28, p. 337-351.

CHAPTER 7

SUMMARY, CONCLUSION AND RECOMMENDATION FOR FUTURE WORK

7.1 Summary and conclusion of the research

The proposed theoretical model to describe the drying of a porous medium has been successfully implemented with respect to the hygrothermal drying of a brick and the isothermal drying of shell that comprises either a single layer or multilayer domain that includes the addition of wet layers to replicate shell build up. The completeness of the proposed model has been dependent on the successful integration of the governing equations based on Whitaker's model (Whitaker, 1977) into a numerical solution that uses the finite element spatial discretisation and a fully implicit backward time stepping scheme. Some earlier works have been taken to verify the proposed model against analytical solutions, benchmark experiments and data derived from laboratory studies on drying within the shell build up process.

This fully coupled model that is proposed in this work describes the moisture transfer as both liquid and vapour and includes the evaporation and condensation term. The condensation term also is considered in the gas and vapour transport equations. The transport equation of gas flow contributes to the movement of vapour flow under the control of the convective ambient condition. Heat transfer mechanisms of conduction, liquid, vapour and air convection and latent heat have been accommodated. In the proposed model some consideration of the relationship between the heat and mass transfer coefficient and the surface water content at the bounding surface of the domain are also included in the convection mechanism. In general this proposed model that is based on the solid, liquid and gas phases represents a most rigorous

approach to simulate the drying of a ceramic porous system.

The following conclusions may be drawn from the work presented in this thesis:

The validation of the thermal component of the proposed model within a one dimensional framework shows an excellent agreement for prescribed and gradient boundary conditions when compared with an analytical solution. The accuracy of the proposed time stepping scheme has been investigated in the both case studies and has showed a good agreement when compared to the analysis solutions and previous works.

Comparison of this proposed coupled model with its solution scheme against the brick drying benchmark by Stanish *et. al* (1986) for the first time has demonstrated that the model and solution scheme are compatible with the brick drying benchmark. By developing the heat transfer formulation to include latent heat contribution, the current proposed model showed a good improvement over previous work published in (Stanish *et al.*, 1986). In general this complete fully coupled model shows a good agreement with most previous drying models where the working variables such as temperature, moisture content, gas pressure, etc. show at least identical trends in both space and time variation.

The capability of the fully coupled model was further extended to investment casting shell drying by including single and multilayer domains. The simulation was benchmarked against the single layer shell data in the experimental work by Leyland (11-14 September 1995), again giving a good agreement with the experimental data recorded for moisture loss.

Following on from the above validation, investigation was extended to the multilayer case study with two different sub-case studies to explore the correctness of the simulation work. The second case study was a comparison for a multilayer that has the initial saturation gradient defined from the experimental work and so the emphasis was on predicting the final drying transient of the fully assembled shell. This showed a small deviation from the experimental results. The first case study focused on replicating the dipping and drying sequence of shell build up. Investigation of the

latter showed that the simulated result in every layer showed the right pattern of reduction in moisture loss when compared with the experiment and gave a superior agreement with experiment when drying of the final assembled shell was undertaken. Therefore, the **First approach** has been demonstrated to be applicable to simulate the drying process during the build up of an investment casting shell. In fact the **First approach** can be defined as an "ab initio" method for simulating the drying of an investment casting shell as it is built up by successive layering.

The investigation was further extended to the two dimensional corner shape domain that is exposed to two convective boundaries that are pertinent to shell drying. A single and two layer shell system was explored. Both systems show a consistent relationship between the moisture content and pore water pressure where both showed the fastest changes at the tip of the corner zone because this is the area where heat and moisture loss is comes from two sides.

Regarding the above corner shape it can be concluded that the fully coupled model with selected numerical scheme is robust and may be extended to more complex shape geometries.

In designing the simulation process for the multilayer domain, both linear and corner sections show a short transient during which balancing of the moisture level between the dried and the wet layer takes place. This is followed by a drying schedule that follows the well recognised constant and falling rate periods.

Through investigation of many case studies (either drying of brick or shell bodies) that have been examined under Chapter 6, the simulated result not only showed a good agreement when tested against experimental data but also a good agreement with trends that have been published in works that describe developments and implementation of numerical simulation within the wider field of drying that has been discussed in Chapter 2. In fact this investigation has demonstrated that a simulation tool that has been developed principally for geotechnical application may be adapted appropriately for ceramic shell drying.

7.2 Recommendation

The model developed to simulate drying of the ceramic shell layer and ceramic brick incorporating fully coupled heat and mass transfer has shown to be capable of giving good results in all case studies presented in Chapter 6. However, extension of this work is still possible. Suggestions regarding the further development are proposed below:

The moisture transport either via capillarity, diffusion and gas migration process is highly influenced by material properties or transport properties such as the water retention curve, relative permeability of each phases, diffusivity coefficient etc. The approach in this thesis has the advantage that relevant material data can be determined through experimentation. Therefore, is highly recommended that characterisation that is aligned with the material model defined in this is work is undertaken to establish a coherent data set that will improve the accuracy in analysing the drying of the shell mould.

Although considerable progress has been made in the verification of this fully coupled drying model, further validation of the whole system for the multilayer problem needs to be done to explore and establish a better material model.

The model has been implemented in two dimensions, extension to full-scale simulation in three dimensions is straight forward and will be a requirement for complex shell systems. Extension to three dimensions will also require careful consideration of computing requirements, especially for complex geometries that are typical of investment cast parts.

The anisotropy of the ceramic body (ceramic shell or brick) was not considered in the model. Natural porous media exhibit the characteristic anisotropy in properties such as hydraulic conductivity, gas permeability and mechanical dispersion. To achieve this, the anisotropy of ceramic properties should be included.

To obtain accurate values in the convective transport mechanism, the conduction and diffusion through the stagnant layer of air at the immediate boundary surface may need to be considered. This involves the introduction of a correction factor in the correlation of heat and mass transfer coefficient.

This work has used existing empirical heat and mass transfer coefficient that govern drying of most porous media. Further improvement may be gained by modelling the surrounding fluid flow. Therefore some work needs to be done in order to couple the existing drying model with the external flow domain.

The current model is capable of simulating the drying process. However, the porous ceramic body is also subjected to shrinkage and cracking, which is the main factor that contributes to the loss of casting production. Therefore, the inclusion of a deformation model to capture the hygrothermal stress due to moisture gradient is also recommended.

This drying study presents only the drying due to free water removal. A fully integrated model could include bound water diffusion mechanisms, especially when considering high temperature drying that will occur as part of the dewaxing and firing sequence for the shell. The critical part dealing with the bound water coefficient is to find their diffusivity coefficients which are highly depended on material properties, which can only be determined experimentally.

REFERENCES

Leyland, S., and Jones, S., 11-14 September 1995, The Effect of Varying The Intercoat Drying Time Upon The Rate of Moisture Removal Form Investment Casting Shell Mould: 22nd BICTA Conference.

Stanish, M.A, Schajer, G.S, and Ferhan, K., 1986, A Mathematical Model of Drying for Hygroscopic Porous Media: AIChE, v. 32, p. 1301-1311.

Whitaker, S., 1977, Simultaneous Heat, Mass and Momentum Transfer in Porous Media; A Theory of Drying: Advances in Heat Transfer, v. 13, p. 119-203.

APPENDIX A1

MATERIAL CONSTANT

A1.1. The Properties of Liquid Water

Liquid water density, ρ_l=1000 kg/m^3

Molecular weight, M_w =18.02 g/ mol

The specific heat capacity, C_{pl}= 4180 J/ kg K

The thermal conductivity of liquid water, λ_l = 0.6 W/ m K

A1.2. The Properties of gas (vapour and air)

The value universal gas constant; R = 8.314 J/ K mol

A1.3 The Properties of Vapour

The molecular weight, M_{gv} = 18.02 g/ mol

The vapour gas constant, R_v = 461.5 J/ K kg

The specific heat capacity of water vapour, C_{pv} =1870 J/ kg K

The latent heat of vaporisation, L = 2.4x10^6 J/ kg

A1.4 The Properties of air

The dynamic viscosity of air, μ_a = 0.02965

The thermal conductivity of vapour, λ_a = 0.028 W/ m K

A1.5. Water retention curve parameters

n = 0.5146

m = 0.4853

α = 37.5438 MPa

A1.6. The relationship between the heat and mass transfer coefficient and the surface water content

$\eta_h = 0.8$

$\eta_T = 0.1$

APPENDIX A2

MATERIAL PROPERTY SENSITIVITY

This section is presented in order to determine response sensitivity with respect to selected material properties. Some comparison of the output variable evolution with the benchmark case study is presented in here. Two parameters that define the material properties have been chosen for the investigation. These are the intrinsic permeability value and the porosity value. This is due to the fact that theoretically these variables have a significant influence on the saturation and transport through the porous network during the drying process. All the results comparisons are based on the fully coupled model investigation for the one dimensional convective drying of the brick in Section 6.3. In conducting this sensitivity study, material parameters were disturbed by only a small amount, because to achieve a converged solution it is necessary to have a compatible data set for the material parameters, the solution does not converge under any arbitrary assignment of material properties.

A2.1 Intrinsic permeability value, K_{intc} changed by a factor of 10.

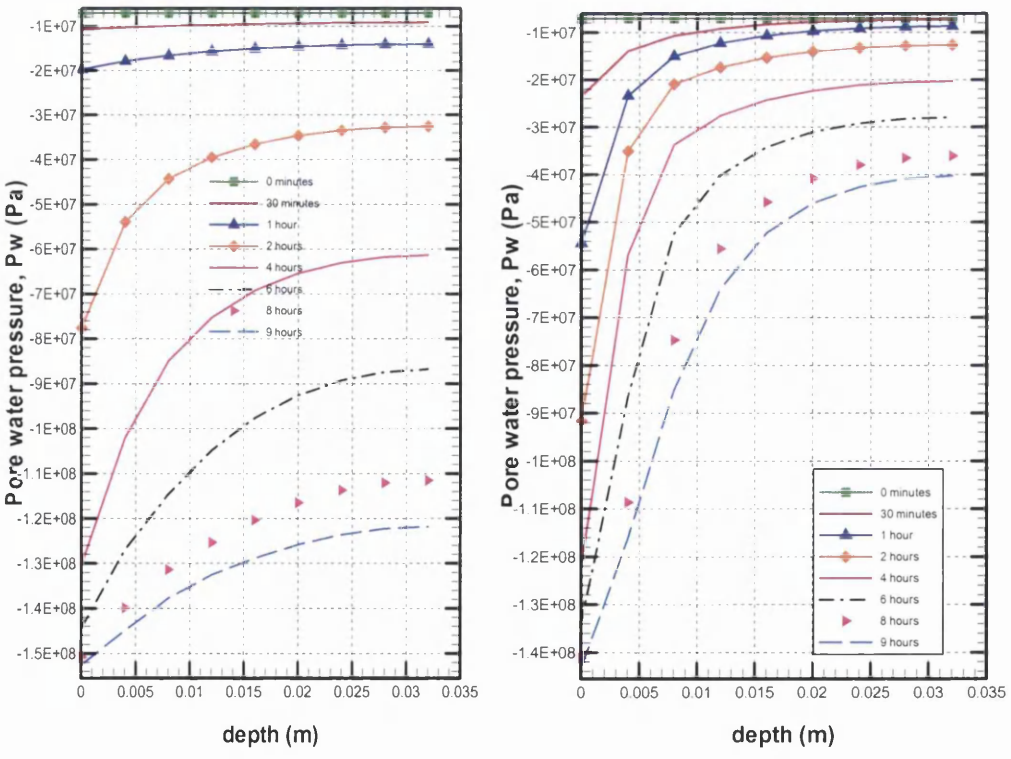

(a) (b)

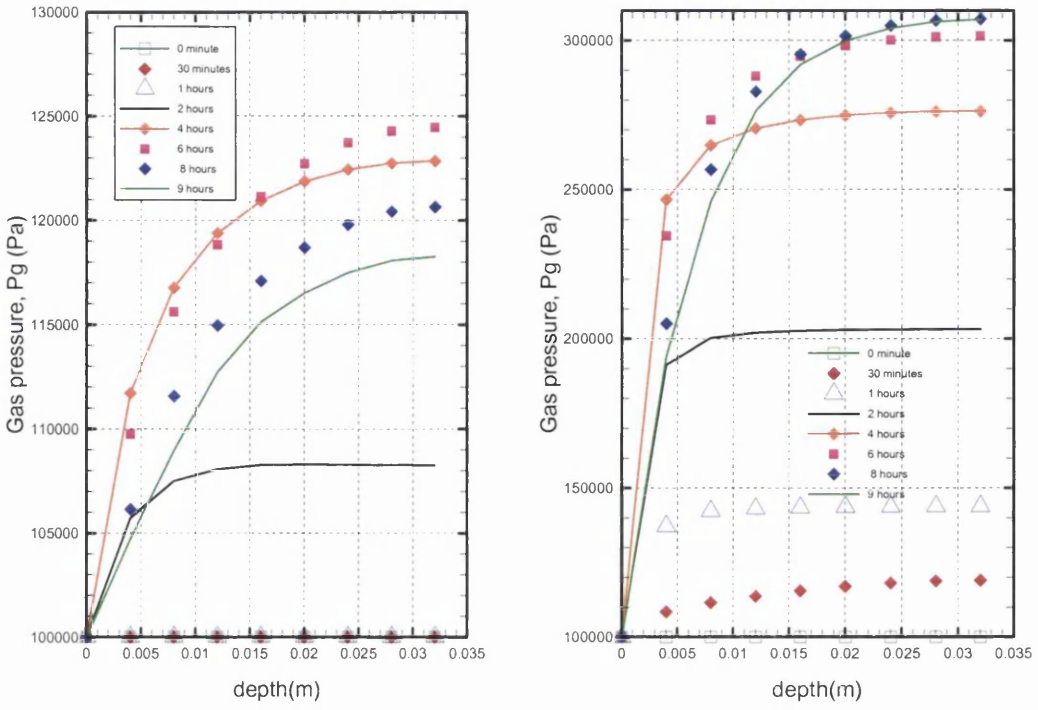

Figure A2.1 : The pore water pressure with different time at intrinsic permeability value, K_{intc} = 1.0 x 10^{-16} (a) and K_{intc} = 1.0 x 10^{-17} (b). The gas pressure variation with different time at K_{intc} = 1.0 x 10^{-16} (c) and K_{intc} = 1.0 x 10^{-17} (d).

In this case study, a slightly lower intrinsic permeability value compared to the standard value (in Table 3.1) was selected for the investigation. The result of the pore water pressure shows that all evolution of pore water pressure is very steep along to the convective boundary with the lower permeability value. This is linked directly to the ease of liquid movement in the pore section as it described by the permeability level and hygroscopicity of the body. Therefore from the plots, it can be concluded that this lower permeability value will result in a higher pore water pressure and gas pressure created within the network as water is removed.

A2.2 Porosity value, ϕ=0.1 to 0.45.

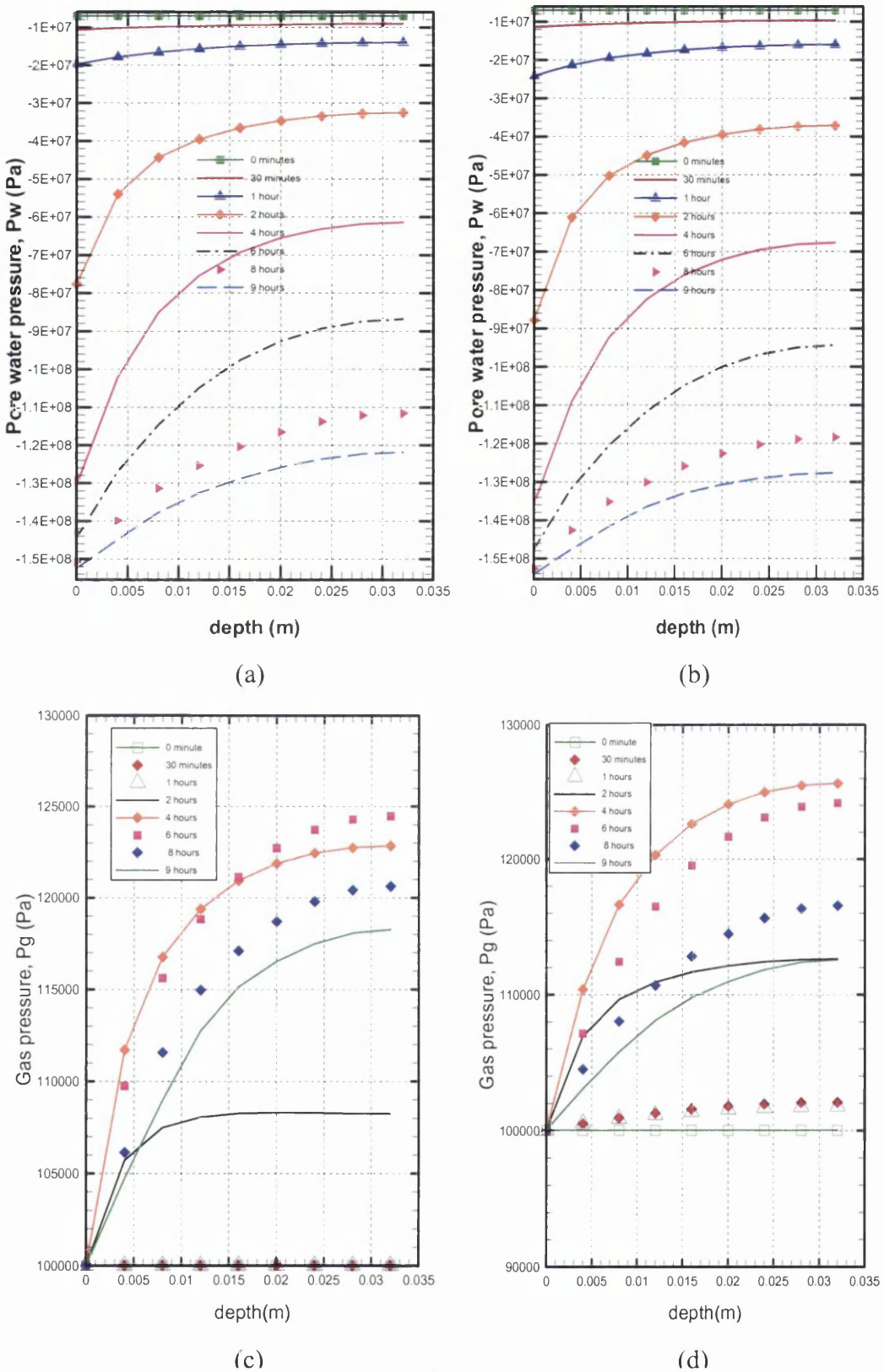

Figure A2.2: The pore water pressure with different time at porosity value, ϕ = 0.12 (a) and ϕ = 0.1 (b). The gas pressure variation with different time at porosity value, ϕ = 0.12 (c) and ϕ = 0.1 (d).

Based on the above selected porosity, the simulated results for the gas and pore water pressures are presented in Figure A2.2. The pore water pressure evolution (in Figure A2.2(b)) and gas pressure evolution (in Figure A2.2(d)) showed a slightly higher value than the previous computed values as presented in Figure A2.2(a) and in Figure A2.2(c). Therefore at this lower porosity value, the pore and gas pressures will increase as the movement of the fluid is more restricted within the network. The next sets of comparisons illustrate sensitivity with respect to higher porosity values that are expected to approximate those of a ceramic shell material.

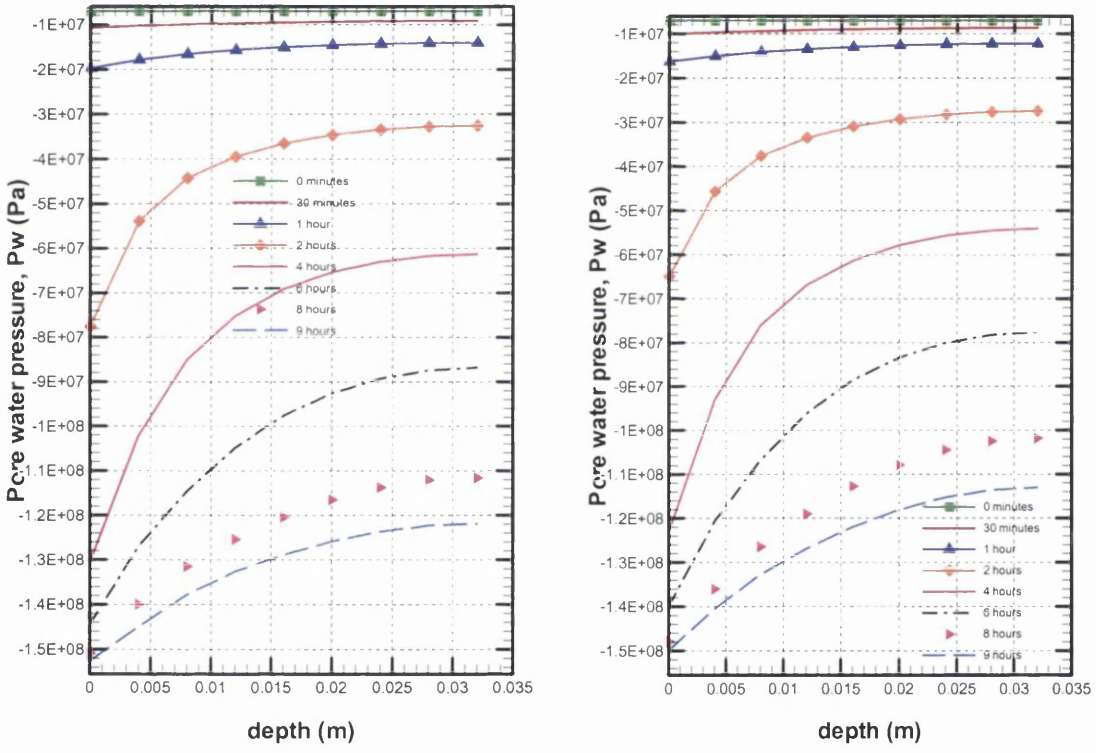

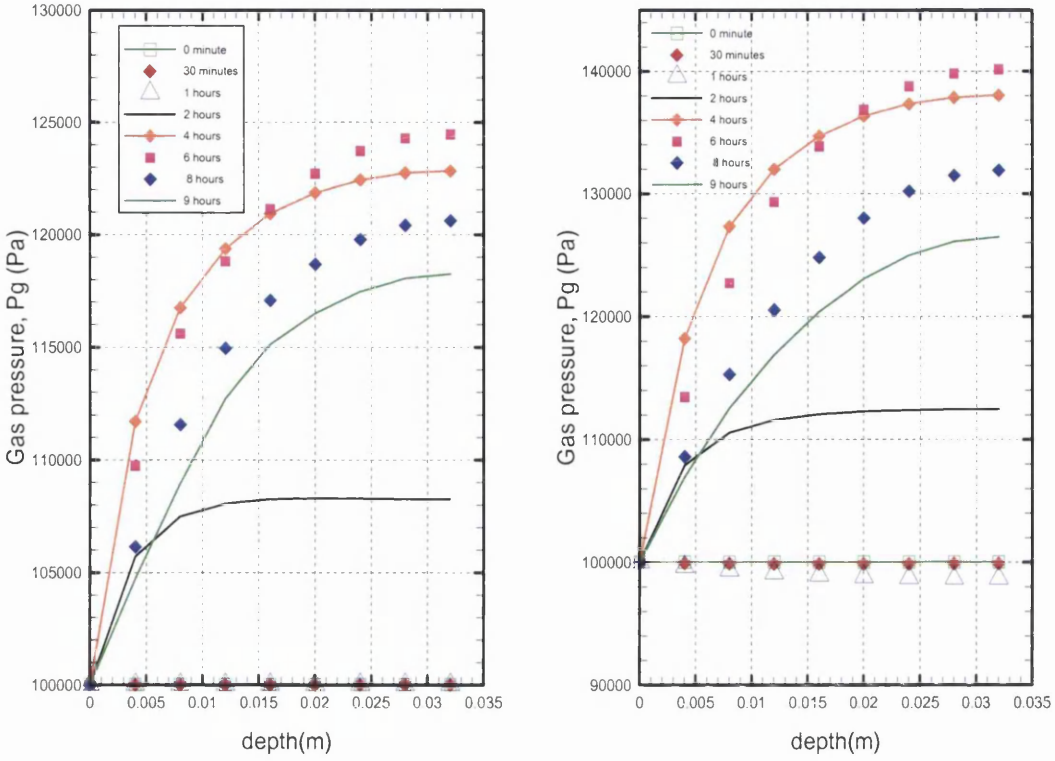

(c) (d)

Figure A2.3 : The pore water pressure with different time at porosity value, $\phi = 0.12$ (a) and $\phi = 0.15$ (b). The gas pressure variation with different time at porosity value, $\phi = 0.12$ (c) and $\phi = 0.15$ (d).

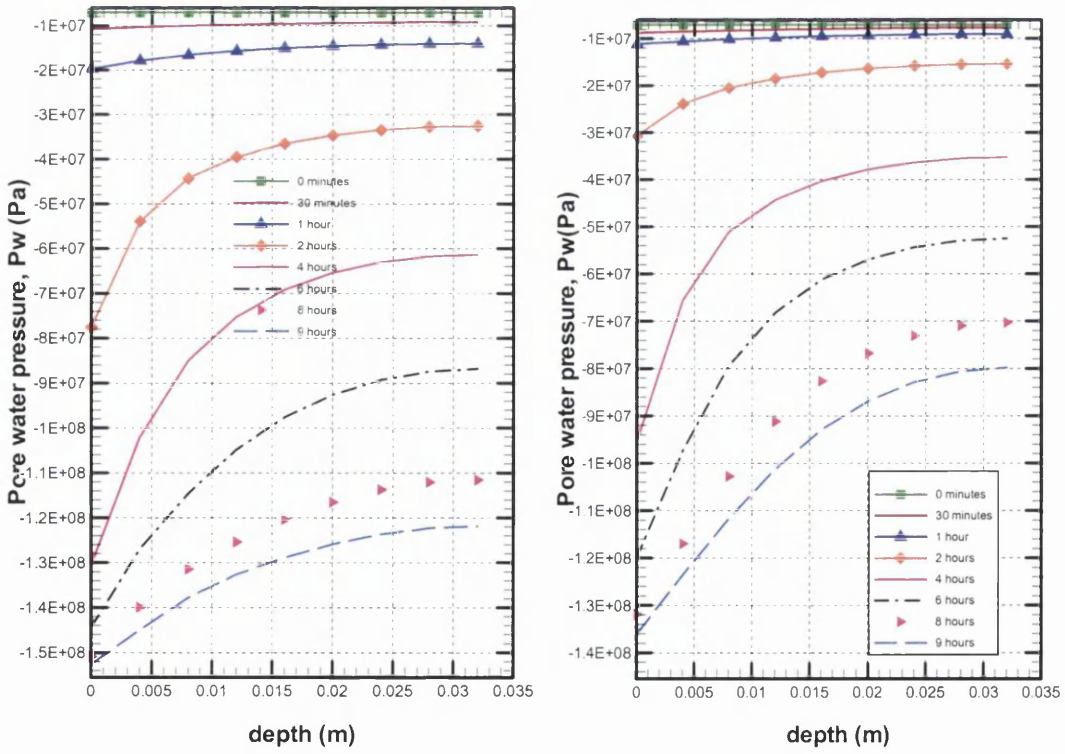

(a) (b)

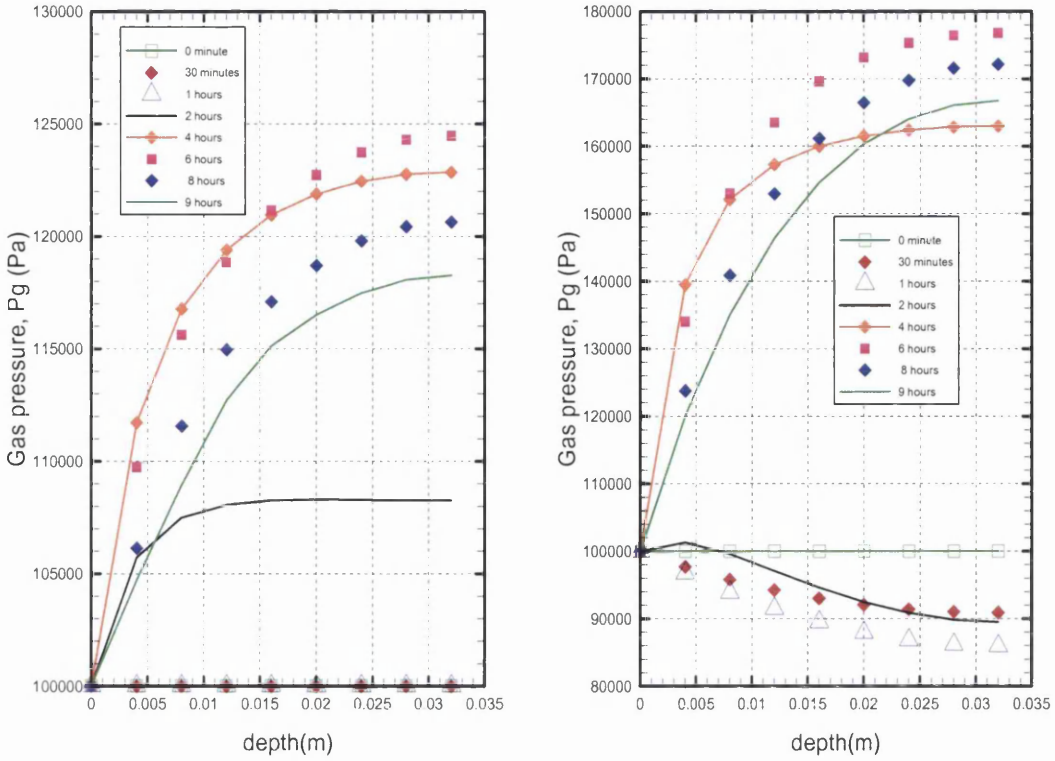

(c) (d)

Figure A2.4 : The pore water pressure with different time at porosity value, $\phi = 0.12$ (a) and $\phi = 0.3$ (b). The gas pressure variation with different time at porosity value, $\phi = 0.12$ (c) and $\phi = 0.3$ (d).

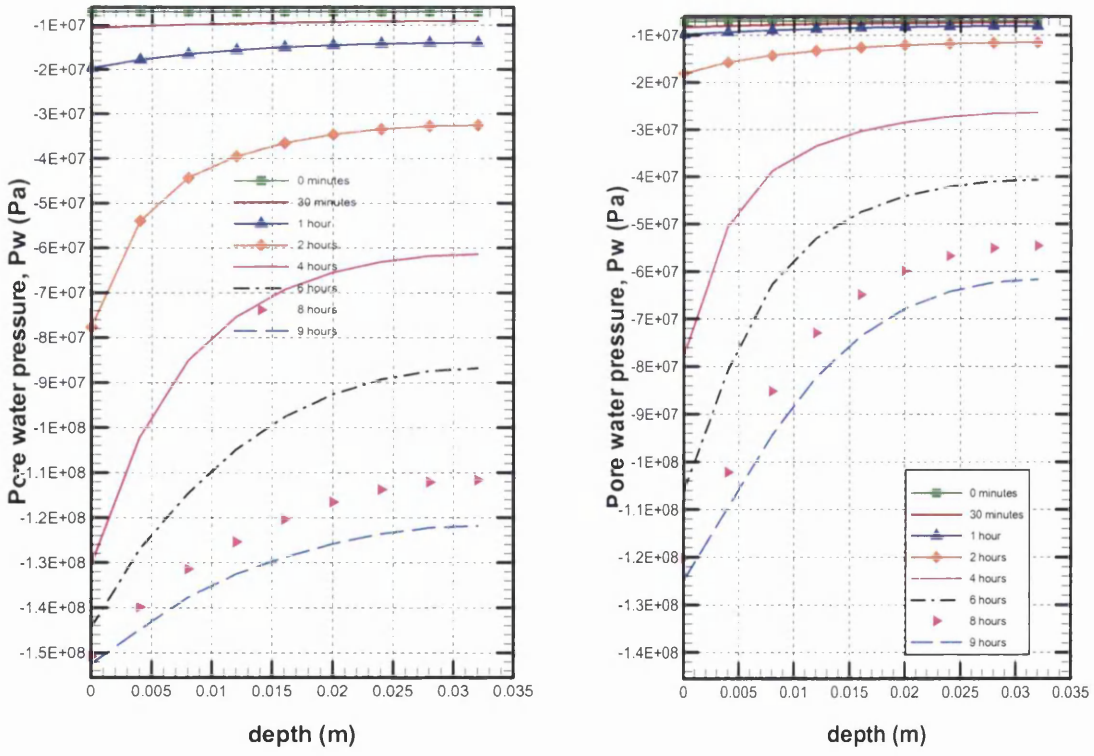

(a) (b)

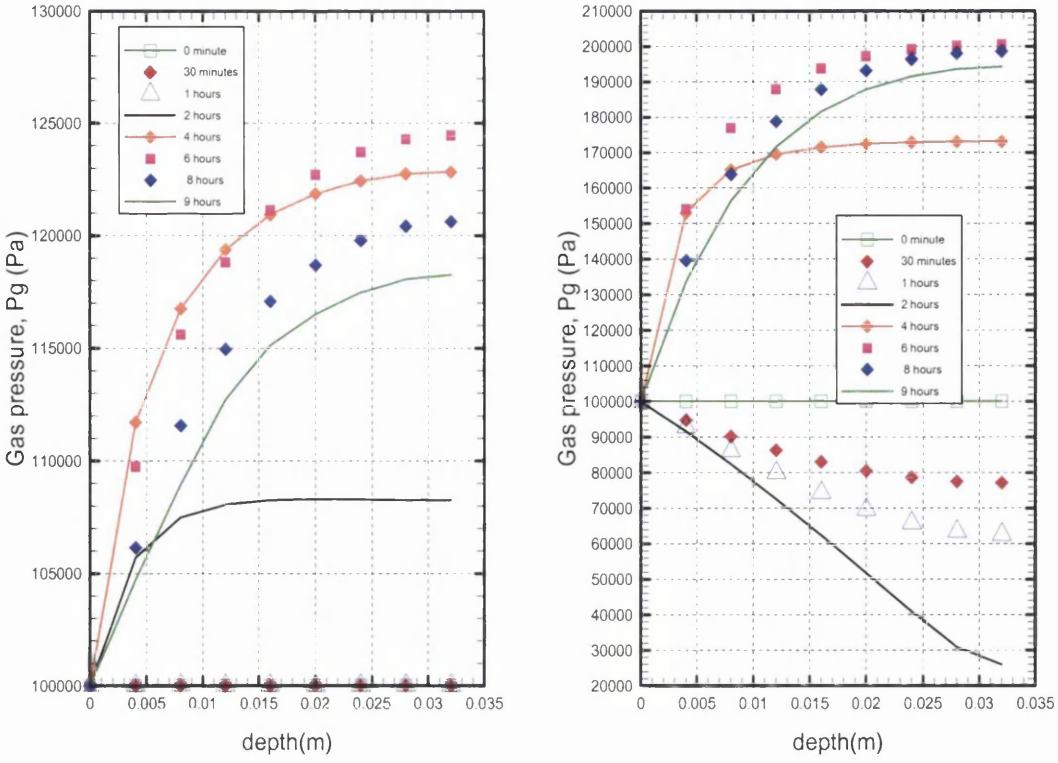

(c) (d)

Figure A2.5 : The pore water pressure with different time at porosity value, $\phi = 0.12$ (a) and $\phi = 0.45$ (b). The gas pressure variation with different time at porosity value, $\phi = 0.12$ (c) and $\phi = 0.45$ (d).

With regard to the above case study (as presented in Figure A2.2), several investigations have been carried out to explore a range of porosity values. By increasing the porosity values the results show that the pore water pressure evolution is reduced when compared with the validation datasets.

Based on the above case studies and comparisons that have been done, the material properties do have an impact on pore water and gas transport highlighting the need for accurate determination of these material parameters.

APPENDIX A3

Figures for the case study for a two layer linear section.

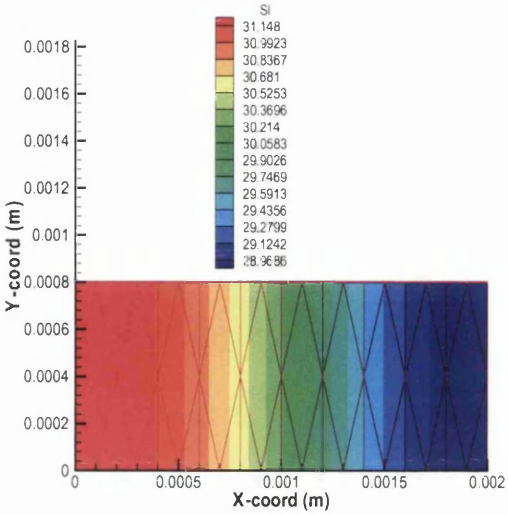

(a)

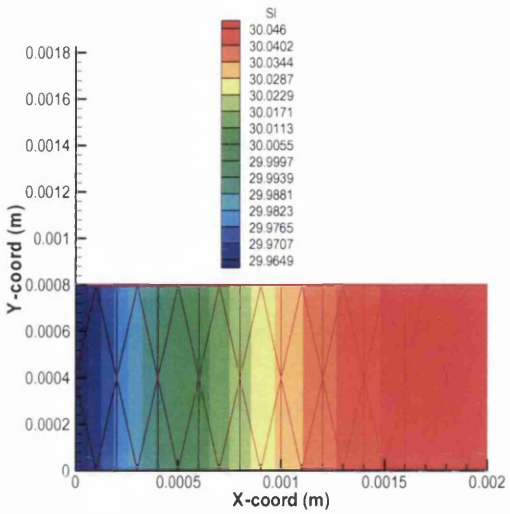

(b)

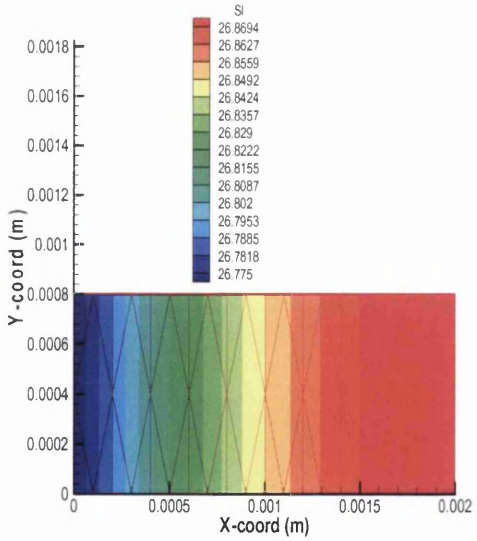

(c)

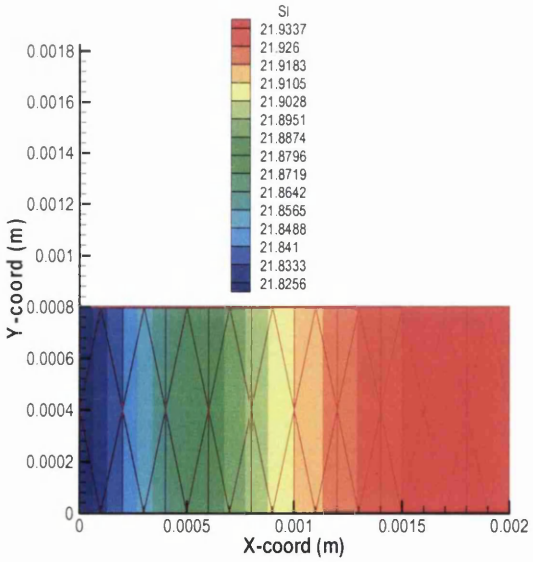

(d)

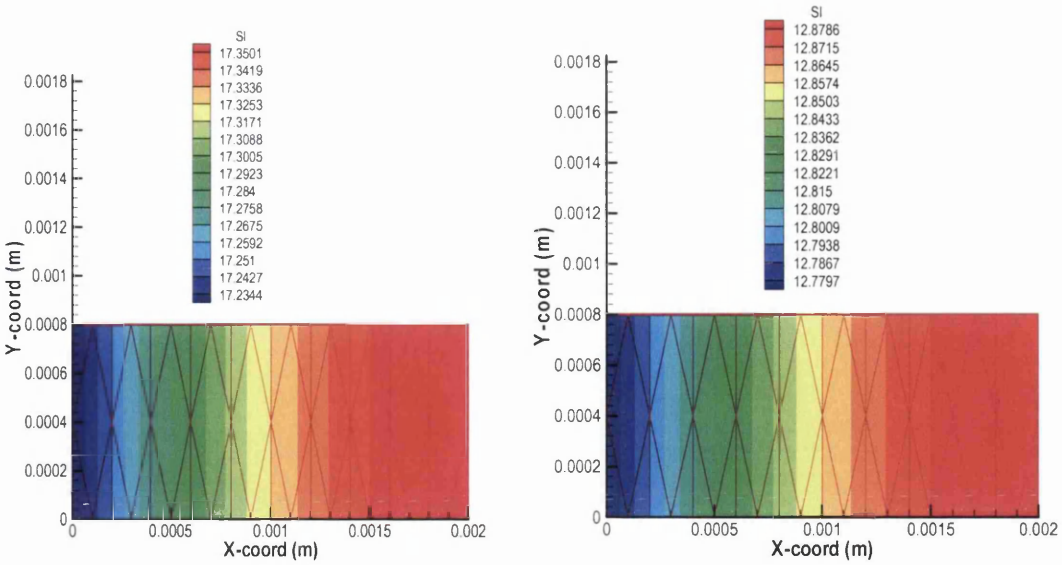

(e) (f)

Figure A3.1: Saturation at 10 seconds (a), 30 seconds (b), 10 minutes (c), 30 minutes (d), 1 hour (e) and 2 hours (f) for two layers system with linear section

APPENDIX A4

List of Publications;

- Harun, Z., Gethin, D.T., Lewis, R.W., and Ferguson, W.J., Drying of A Multilayer Ceramic Shell Body: Proceedings of the Fifteenth UK Conference of The Association of Computational Mechanics in Engineering, Glasgow, UK, 2^{nd}-3^{rd} April, 2007.
- Harun, Z., Gethin, D.T., Lewis, R.W., and Ferguson, W.J., Combined Heat and Mass Transfer for Drying Ceramic Shell: The International Symposium on Multiphysics, Maribor, Slovenia, 14^{th}-15^{th} December, 2006.